



Cyprus  
University of  
Technology



杭州电子科技大学  
HANGZHOU DIANZI UNIVERSITY

**Master's thesis**

**Texture Analysis in Prostate Ultrasound Images  
Based on Different Pre-processing Schemes**

**Haohan Yu**

**Limassol, June 2025**



**MSc in Electronics Science  
and Technology**



CYPRUS UNIVERSITY OF TECHNOLOGY

Faculty of Engineering and Technology

Department of Electrical Engineering, Computer Engineering, and Informatics

Master's thesis

**Texture Analysis in Prostate Ultrasound Images  
Based on Different Pre-processing Schemes**

Haohan Yu

Supervisor

Christos P. Loizou

Limassol, June 2025

## **Approval Form**

Master's thesis

# **Texture Analysis in Prostate Ultrasound Images**

## **Based on Different Pre-processing Schemes**

Presented by

Haohan Yu

**Supervisor:** Christos P. Loizou

**Member of the committee:** Committee member 1

**Member of the committee:** Committee member 2

Cyprus University of Technology  
Limassol, June 2025

## **Copyrights**

Copyright © 2025 Haohan Yu

All rights reserved.

The approval of the dissertation by the Department of Electrical Engineering, Computer Engineering, and Informatics does not necessarily imply the approval by the Department of the views of the writer.

## **Acknowledgements**

I would like to express my sincere gratitude to my supervisors, Prof. Christos P. Loizou and Prof. Xiwei Huang, for their invaluable guidance, continuous support, and insightful advice throughout this study. Their expertise and encouragement were essential to the completion of this work.

I would also like to thank the Department of Electrical Engineering, Computer Engineering and Informatics at Cyprus University of Technology, and the Innovation Center for Electronic Design Automation Technology at Hangzhou Dianzi University, for providing the research environment and resources necessary for this study.

Special thanks to my colleagues and friends for their assistance and constructive discussions during the research process.

Finally, I am grateful to the German Oncology Center, Nicosia, Cyprus, for providing access to the medical imaging data used in this study.

# ABSTRACT

Prostate cancer (PCa) remains a significant global health concern, with transrectal ultrasound (TRUS) commonly used for its detection due to its accessibility and cost-effectiveness. However, TRUS imaging is limited by speckle noise and low contrast, which compromise diagnostic accuracy. This study investigates the effect of preprocessing techniques—normalization, despeckling, and their combination—on TRUS image quality and texture feature stability to enhance computer-aided diagnosis (CAD) of PCa. A total of 1,316 texture features, including first-order statistics, shape descriptors, and higher-order matrices (GLCM, GLDM, GLRLM, GLSZM, NGTDM), were extracted from automatically segmented prostate regions. Image quality was evaluated using four quantitative metrics, demonstrating that the combination of normalization and Non-Local Means Filtering (NLMF) significantly improved contrast and feature consistency. Among the extracted features, 318 showed high stability (Spearman correlation coefficient  $\rho \approx 0.9\text{--}1.0$ ) across preprocessing schemes. Using these stable features, a Support Vector Machine (SVM) classifier achieved an area under the curve (AUC) values of approximately 0.92, indicating strong diagnostic performance. In conclusion, appropriate preprocessing—particularly normalization combined with NLMF—enhances TRUS image quality and preserves diagnostically relevant texture features, supporting more accurate and reliable CAD systems for prostate cancer detection.

**Keywords:** Prostate Ultrasound, Prostate Cancer, Pre-processing, Texture Analysis, Transrectal Ultrasound

# TABLE OF CONTENTS

<b>ABSTRACT</b>	<b>v</b>
<b>TABLE OF CONTENTS</b>	<b>vi</b>
<b>LIST OF TABLES</b>	<b>viii</b>
<b>LIST OF FIGURES</b>	<b>ix</b>
<b>LIST OF ABBREVIATIONS</b>	<b>xii</b>
<b>1 Introduction</b>	<b>1</b>
1.1 Aims and Objectives . . . . .	6
1.2 Research Questions . . . . .	7
1.3 Contribution . . . . .	7
1.4 Structure of the Thesis . . . . .	8
1.5 Summary . . . . .	8
<b>2 Literature Review</b>	<b>10</b>
<b>3 Research Methodology</b>	<b>15</b>
3.1 Acquisition of Ultrasound Images . . . . .	15
3.2 Types of Image Noise . . . . .	16
3.2.1 Speckle Noise . . . . .	17
3.2.2 Salt and Pepper (Impulse) Noise . . . . .	18
3.2.3 Gaussian Noise . . . . .	18
3.3 Filtering Methods . . . . .	19
3.3.1 Intensity Normalization . . . . .	19
3.3.2 Average Filtering . . . . .	20
3.3.3 Bilateral Filtering . . . . .	21
3.3.4 Median Filtering . . . . .	21
3.3.5 Wiener Filtering . . . . .	22
3.3.6 Non-Local Means Filtering . . . . .	23
3.4 Segmentation Algorithm . . . . .	24
3.5 Texture Features . . . . .	25
3.6 Quality Evaluation and Statistical Analysis . . . . .	27
3.7 Classification Modeling . . . . .	28

<b>4 Results</b>	<b>30</b>
<b>5 Conclusion and Discussion</b>	<b>48</b>
5.1 Implications for CAD Systems . . . . .	51
5.2 Limitations . . . . .	53
5.3 Future Work . . . . .	55
5.4 Conclusion . . . . .	56
<b>BIBLIOGRAPHY</b>	<b>57</b>
<b>APPENDICES</b>	<b>67</b>
<b>I List of Selected Stable Texture Features</b>	<b>68</b>

# LIST OF TABLES

4.1	The median ( $\pm$ IQR) values of texture features extracted from segmented PCa ultrasound images (Nr = 382), including O, N, and images further processed with various filtering methods (AF, BF, MF, WF, and NLMF) based on both the original and normalized images. The extracted features include OGCC, LFI, W1GSS, W5FE, W8GDS, and GGCI . . . . .	32
4.2	Texture features were extracted as median ( $\pm$ IQR) values from cancerous regions segmented from PCa ultrasound images (Nr = 382), including original images (O), normalized images (N), and images further processed with various filtering methods (AF, BF, MF, WF, and NLMF) based on both the original and normalized images. The extracted features included OGCC, LFI, W1GSS, W5FE, W8GDS, and GGCI . . . . .	33
4.3	Texture features were extracted as median ( $\pm$ IQR) values from normal regions segmented from PCa ultrasound images (Nr = 382), including original images (O), normalized images (N), and images further processed with various filtering methods (AF, BF, MF, WF, and NLMF) based on both the original and normalized images. The extracted features include OGCC, LFI, W1GSS, W5FE, W8GDS, and GGCI . . . . .	34
4.4	Quality EM median( $\pm$ IQR) values for all the segmented ultrasound prostate images (Nr = 382) extracted between the O and all various filtering methods (AF, BF, MF, WF, NLMF). . . . .	35
4.5	Shapiro–Wilk test p-values for each texture feature across different preprocessing methods. All p-values are reported in scientific notation. A p-value less than 0.05 indicates that the null hypothesis of normality is rejected, suggesting the corresponding feature does not follow a normal distribution under that preprocessing condition. . . . .	35
4.6	Statistical analysis using the Mann–Whitney rank-sum test ( $p < 0.05$ ) was conducted for the p-values of texture features extracted between all different preprocessing schemes O, N, D(NNLMF), and ND. The Spearman correlation coefficients ( $\rho$ , p-value) are also presented. Features with statistical significance are highlighted in bold. . . . .	36
4.7	Classification performance (Accuracy and AUC) under different preprocessing schemes . . . . .	46
I.1	Selected stable texture features . . . . .	68

# LIST OF FIGURES

3.1	Flow diagram of the integrated system as proposed in this study for the PCa ultrasound texture analysis. (1) Data Acquisition (TRUS) Images, (2) Data Selection & Segmentation, (3) Image Preprocessing, transformation, (4) Image Quality Assessment & Selection and evaluation metrics, (5) Image transformations, (6) Features extraction, (7) Significance analysis (8) Statistical analysis, (9) Identify stable vs unstable features for the different preprocessing schemes. Np: Number of patients, Nr: Number of images, O: Original images, N: Normalization, AF: Average Filtering, BF: Bilateral Filtering, MF: Median Filtering, WF: Wiener Filtering, NLMF: Non-Local Means Filtering, EM: Evaluation metrics, PSNR: Peak Signal-to-Noise Ratio, SSIM: Structural Similarity Index Measure, RMSE: Root Mean Square Error, CNR: Contrast-to-Noise Ratio, GLCM: Gray-Level Co-occurrence Matrix, GLDM: Gray-Level Dependence Matrix, GLRLM: Gray-Level Run Length Matrix, D: Des-peckle, ND: normalization and despeckle. . . . .	16
4.1	PCa ultrasound images were automatically segmented, to extract texture features based on different preprocessing schemes, including the following: a) O, b) AF, c) BF, d) MF, e) WF, f) NLMF. The texture features are described using OGCC (GLCM-Correlation) and W8GDS (Wavelet-LLL-GLDM-Small-Dependence High Gray Level Emphasis). . . . .	30
4.2	PCa ultrasound images were automatically segmented, to extract texture features based on different preprocessing schemes, including the following: a) N, b) NAF, c) NBF, d) NMF, e) NWF, f) NNLMF. . . . .	31
4.3	Segmentation of cancerous regions in PCa ultrasound images was performed to extract texture features from the original and normalized images. . . . .	31
4.4	Segmentation of cancerous regions in PCa ultrasound images was performed to extract texture features from the original and normalized images. . . . .	32
4.5	Boxplots of six different texture features extracted from the entire (whole) region of PCa ultrasound images under different preprocessing conditions: original (O), normalized (N), filtered (D), and normalized + filtered (ND). The extracted features include: a) OGCC, b) LFI, c) W1GSS, d) W5FE, e) W8GDS, and f) GGC. These visualizations highlight the distribution and variability of texture features across different preprocessing pipelines for whole-region analysis. . . . .	37
4.6	Boxplots of six different texture features extracted from the cancerous tissue region of PCa ultrasound images under different preprocessing conditions (O, N, D, ND). . . . .	38
4.7	Boxplots of six different texture features extracted from the normal tissue region of PCa ultrasound images under different preprocessing conditions (O, N, D, ND). . . . .	39

4.8	Regression plots between the O vs ND of six different texture features extracted from the whole region of PCa ultrasound images. The extracted features include: a) OGCC, b) LFI, c) W1GSS, d) W5FE, e) W8GDS, and f) GGCI.	40
4.9	Regression plots between the O vs ND of six different texture features extracted from the cancerous tissue region of PCa ultrasound images for: a) OGCC, b) LFI, c) W1GSS, d) W5FE, e) W8GDS, and f) GGCI.	41
4.10	Regression plots between the O vs ND of six different texture features extracted from the normal tissue region of PCa ultrasound images for: a) OGCC, b) LFI, c) W1GSS, d) W5FE, e) W8GDS, and f) GGCI.	42
4.11	Bland-Altman plots between the O vs ND of six different texture features extracted from the whole region of PCa ultrasound images. The extracted features include: a) OGCC, b) LFI, c) W1GSS, d) W5FE, e) W8GDS, and f) GGCI.	43
4.12	Bland-Altman plots between the O vs ND of six different texture features extracted from the cancerous tissue region of PCa ultrasound images for: a) OGCC, b) LFI, c) W1GSS, d) W5FE, e) W8GDS, and f) GGCI.	44
4.13	Bland-Altman plots between the O vs ND of six different texture features extracted from the normal tissue region of PCa ultrasound images for: a) OGCC, b) LFI, c) W1GSS, d) W5FE, e) W8GDS, and f) GGCI.	45
4.14	ROC curves for SVM-based classification of cancerous versus normal tissue regions in prostate ultrasound images, under different preprocessing and feature selection strategies. (a) ROC curve based on all features extracted from O images (b) ROC curve based on all features extracted from NNLMF-processed images (c) ROC curve based on 318 stable features selected from O images (d) ROC curve based on 318 stable features selected from NNLMF-processed images.	46



# LIST OF ABBREVIATIONS

- AF: Average Filtering.
- AUC: Area Under the Receiver Operating Characteristic (ROC) curve.
- BF: Bilateral Filtering.
- bpMRI: Biparametric Magnetic Resonance Imaging.
- CAD: Computer-Aided Diagnosis (system).
- CNR: Contrast-to-Noise Ratio.
- DRE: Digital Rectal Examination.
- ECE: Extracapsular Extension.
- GGCI: Gradient\_GLCM\_Inverse Variance.
- GLCM: Gray-Level Co-occurrence Matrix.
- GLDM: Gray-Level Dependence Matrix.
- GLRLM: Gray-Level Run Length Matrix.
- GLSZM: Gray-Level Size Zone Matrix.
- GMRF: Gaussian Markov Random Field.
- HMM: Hidden Markov Model.Emphasis.
- k-NN: k-Nearest Neighbors.
- LBP: Local Binary Pattern.
- LFI: Logarithm First-order Interquartile Range.
- MSE: Mean Squared Error.
- MF: Median Filtering.
- MRI: Magnetic Resonance Imaging.
- mpMRI: Multiparametric Magnetic Resonance Imaging.
- NLMF: Non-Local Means Filtering.
- NGTDM: Neighboring Gray Tone Difference Matrix.
- NMF: Normalized Median Filtering.
- NNLMF: Normalized Non-Local Means Filtering.
- NWF: Normalized Wiener Filtering.
- OGCC: GLCM-Correlation.
- PCa: Prostate Cancer.
- PSA: Prostate-Specific Antigen.
- PSNR: Peak Signal-to-Noise Ratio.
- pMRI: Pseudo-Magnetic Resonance Imaging.
- RF: Radio Frequency (signal).
- ROI: Region of Interest.
- ROC: Receiver Operating Characteristic.
- RMSE: Root Mean Square Error.
- SGLDL: Square-Gray Level Dependence Low Gray-Level Emphasis.
- SRGLCD: Square Root-Gray Level Co-occurrence Matrix Difference Variance.
- SSIM: Structural Similarity Index Measure.
- SVM: Support Vector Machine.
- TRUS: Transrectal Ultrasound.
- UTI: Urinary Tract Infection.
- WF: Wiener Filtering.

# 1 Introduction

Prostate cancer (PCa) is one of the most common malignant tumors in men worldwide and one of the major public health issues affecting men's health worldwide. According to data released by the International Agency for Research on Cancer (IARC) at GLOBOCAN 2022 [1], PCa ranks fourth in incidence among all cancer types in the world, accounting for approximately 7.3% new cancer types in men in many high-income countries, and its risk is expected to increase further with the aging of the population and changes in lifestyle. However, thanks to the continuous progress in cancer screening methods and medical imaging diagnostic technologies (such as MRI, TRUS, etc.) in recent years, the mortality rate of PCa has decreased in the past few decades. According to 2022 data, the global age-standardized mortality rate of PCa is approximately 4.1%, which is a decrease from the 7.3% reported earlier in 2018 [1,2]. However, the decline in mortality depends largely on the accessibility and diagnosis level of medical resources between countries, and low-income and middle-income countries still face a higher risk of death. PCa remains one of the leading causes of cancer-related death in men. Therefore, in the current medical environment, early identification of PCa, accurate risk stratification assessment and development of individualized treatment plans can effectively improve patient survival, reduce the risk of overtreatment and improve quality of life.

At present, the clinical diagnosis of PCa mainly relies on a variety of complementary examination methods to achieve a comprehensive assessment of the tumor. These methods include digital rectal examination, prostate-specific antigen detection, transrectal ultrasound, magnetic resonance imaging(MRI), and ultimately prostate tissue biopsy for diagnosis [3]. Each examination method plays a specific role in the clinical pathway of PCa, covering multiple links from initial screening to lesion localization, risk stratification, treatment decision-making and prognosis judgment. In actual diagnosis and treatment, these methods are usually used in combination to improve the overall diagnostic accuracy and scientific nature of decision-making.

Digital rectal examination (DRE) is one of the oldest and easiest physical examination methods for PCa screening. It is usually used as a preliminary evaluation method in routine health examinations or urology clinics [4,5]. The doctor wears a gloved index finger and inserts it into the patient's rectum to palpate and evaluate the size, texture, symmetry, boundary clarity of the prostate, and the presence of abnormal manifestations such as suspicious nodules, lumps or tenderness. This method does not rely on any expensive equipment or complex technology. It has the advantages of short operation time, strong economy, and low burden on patients. It is particularly suitable for primary screening or regular follow-up of high-risk populations in primary health institutions with relatively limited medical resources.

However, the diagnostic efficacy of DRE in clinical practice is limited in many aspects. First, the examination is extremely dependent on the operator's hand sensitivity and clinical experience. Doctors are highly subjective in palpation judgment and lack objective quantitative standards, resulting in low consistency in diagnostic results between different doctors. Secondly, since the prostate is located deep in the pelvic cavity and has a complex shape, DRE can only touch the posterior part of the prostate. If the lesion is located at the distal end of the prostate or is small in size and has no obvious texture changes, it is very easy to be ignored. In addition, for obese patients or those with special rectal anatomical structures,

the palpation accuracy of DRE may be further reduced [4, 5].

In terms of sensitivity and specificity, many studies have shown that DRE has a low detection rate for PCa alone, especially in early asymptomatic patients, and its screening value is limited [4–6]. According to literature reports, the sensitivity of DRE is usually around 50% [6, 7], and the specificity is slightly higher, but it is still not enough to be a reliable single diagnostic tool. Therefore, DRE is often used in combination with other biomarkers such as PSA testing in modern clinical pathways to improve comprehensive judgment capabilities [5]. In recent years, the American Urological Association (AUA) and the European Association of Urology (EAU) have gradually stopped recommending DRE as the only means of routine PCa screening, but advocated individualized screening strategies, combining factors such as age, family history, and PSA levels for comprehensive decision-making [5].

Despite this, DRE still has certain value in detecting obvious masses or highly suspected lesions, especially in resource-limited areas or emergency conditions, as a preliminary evaluation tool. Its reference role in tumor progression and clinical staging (such as T staging) has not been completely replaced. Therefore, as an old but still clinically significant examination method, DRE still plays an important auxiliary role in the multimodal diagnostic system, especially in the context of artificial intelligence and digital health technology not yet being fully popularized, its simplicity and practicality are still relied on by frontline doctors.

Prostate-Specific Antigen (PSA) testing is one of the most widely used and mature serological methods for PCa screening [5, 7]. PSA is a glycoprotein secreted by prostate epithelial cells and is mainly found in semen. Under normal circumstances, only a very small amount of PSA enters the blood circulation. However, when prostate tissue is pathologically damaged or abnormally proliferates (such as cancer, inflammation or hyperplasia), the PSA level in serum will increase significantly. Therefore, the detection of total PSA (tPSA) concentration in the blood can be used as an important indicator for evaluating the functional status and pathological changes of the prostate [5, 7].

PSA testing is widely used for preliminary screening of PCa, evaluation of treatment efficacy, and post-operative recurrence monitoring due to its high sensitivity [5]. In clinical practice, 4.0 ng/mL is usually used as the upper reference limit of tPSA [7]. When the PSA value increases, it indicates that there may be potential lesions in the prostate. However, it should be pointed out that PSA is not a tumor-specific marker, and its level can be affected by a variety of non-malignant factors, including prostatitis, benign prostatic hyperplasia (BPH), urine retention, recent rectal examination or sexual intercourse, etc. Therefore, although PSA has a certain sensitivity to PCa, its specificity is limited, which means that an increase in PSA does not necessarily represent a malignant lesion, which can easily lead to false positive results, causing anxiety in patients, unnecessary imaging examinations, and even traumatic tissue biopsies.

In addition, some patients with PCa may not have obvious PSA increases in the early stages, especially low-grade or atypical PCa, which may also cause false negatives and affect the timely detection of the disease. In order to improve the diagnostic performance of PSA testing, a series of derivative indicators have been developed in recent years, such as the free PSA (fPSA)/total PSA ratio, PSA density (PSA to prostate volume ratio), PSA velocity, etc., to assist in judging the nature and development trend of lesions. In addition, risk prediction tools based on multiple indicators (such as Prostate Health Index, PHI) have also been gradually used for screening high-risk populations, aiming to improve the accuracy of screening and reduce unnecessary biopsies.

Despite certain limitations, PSA testing is still one of the most core serum biomarkers in the current PCa screening system, and is recommended by multiple international guidelines (such as NCCN, EAU, AUA) as a routine test item for high-risk populations. In the future, the combination of multi-parameter MRI, artificial intelligence risk model and genomic analysis technologies is expected to further optimize PSA-related screening strategies and achieve a more accurate and personalized early diagnosis path for PCa.

Magnetic resonance imaging (MRI), especially the multi-parametric MRI (mpMRI) that has emerged in recent years, is playing an increasingly important role in the imaging diagnosis of PCa (PCa). mpMRI combines multiple imaging sequences and parameter information, mainly including T2-weighted imaging (T2WI), diffusion-weighted imaging (DWI), apparent diffusion coefficient map (ADC map) and dynamic contrast-enhanced imaging (DCE), and sometimes also includes magnetic resonance spectroscopy (MRSI). The fusion of these multi-dimensional data enables mpMRI to comprehensively evaluate the anatomical structure, tissue characteristics and biological behavior of the prostate from multiple angles [8].

Among them, T2WI can be used to clearly display the anatomical regions of the prostate (such as the peripheral zone, transition zone, and central zone), which helps to identify lesions with abnormal morphology and unclear boundaries; DWI and ADC images reflect tissue density through the degree of restricted diffusion of water molecules, providing important parameters for distinguishing malignant and benign lesions; and DCE reflects the characteristics of vascularization and enhancement of lesions, especially in the location of suspicious areas. For this reason, mpMRI has excellent performance in improving the accuracy of PCa lesion location, risk stratification ability, and guiding biopsy, and its diagnostic sensitivity and specificity are generally better than traditional ultrasound examinations [9].

At present, many international clinical guidelines, including the European Association of Urology (EAU), the National Comprehensive Cancer Network (NCCN), and the American Urological Association (AUA), recommend routine mpMRI examinations before biopsy in the case of elevated PSA or abnormal DRE [10]. By guiding targeted puncture (MRI-TRUS fusion biopsy or MRI cognitive fusion biopsy), mpMRI can significantly improve the detection rate of clinically significant PCa, reduce the number of unnecessary biopsies, and overdiagnosis of indolent cancer [11].

However, despite the significant advantages of mpMRI in improving the accuracy of PCa diagnosis, it still faces some practical challenges in clinical promotion. First, MRI equipment is expensive, maintenance costs are high, examination time is relatively long, and the requirements for medical resource allocation are high. Second, the quality of image acquisition is greatly affected by the operator's experience, scanning parameter settings, and patient cooperation, and there may be large differences between different hospitals or technology platforms. In addition, the interpretation of mpMRI images requires professional radiologists and is somewhat subjective. Although there is a standardized scoring system PI-RADS (Prostate Imaging Reporting and Data System), the consistency and accuracy of the scoring are still being optimized. Due to these limitations, mpMRI is more commonly used in tertiary hospitals or cancer centers in high-resource countries, but it is difficult to be fully popularized in low- and medium-resource environments [12].

Transrectal Ultrasound (TRUS) (see also Fig.4.1) is one of the most widely used imaging technologies in the diagnosis and treatment of PCa, especially in prostate puncture biopsy, which plays an irreplaceable

and important role. TRUS inserts a high-frequency ultrasound probe into the patient's rectum, close to the dorsal side of the prostate, and obtains a two-dimensional (2D) or three-dimensional (3D) grayscale image of the prostate in real time. It can evaluate the size, shape, structural symmetry, and presence of suspected lesions of the prostate. TRUS is widely used in clinical practice around the world due to its simple operation, fast imaging, no radiation, low equipment cost, and high patient tolerance. It is particularly suitable for areas with limited resources as the main imaging tool for initial screening and biopsy guidance of PCa [13].

In puncture biopsy, TRUS's real-time imaging capability can provide doctors with accurate spatial positioning information, assist in determining the puncture path, improve the accuracy of lesion sampling, and reduce the risk of missed detection. In addition, TRUS is also commonly used to evaluate prostate volume before surgery, monitor tumor development trends, or identify and judge non-neoplastic diseases such as benign prostatic hyperplasia and cysts. In contrast, although magnetic resonance imaging (MRI), especially multi-parameter MRI (mpMRI), has higher sensitivity and specificity in lesion localization and risk stratification, it is still difficult to achieve full replacement in all clinical scenarios due to its high cost, long examination cycle, high equipment threshold, and image interpretation relying on senior radiologists [14].

However, TRUS still faces many challenges in the early identification of PCa. Its imaging process is easily disturbed by speckle noise [15]. This inherent noise will reduce the image clarity, blur the boundaries of prostate tissue, and make the layers unclear, especially when identifying early tumors with small volume and unclear signal characteristics. In addition, TRUS mainly uses grayscale imaging, which has limited tissue contrast and is difficult to accurately distinguish benign lesions from malignant tumors. The accuracy of diagnosis depends largely on the operator's experience level.

Many studies have shown that the diagnostic sensitivity and specificity of TRUS are generally lower than mpMRI, especially in the identification of low-grade cancer lesions in the peripheral area of the prostate. Although mpMRI has been recommended by international clinical guidelines as an important evaluation method before biopsy, its popularity is still uneven around the world due to equipment, cost and operator staffing. Therefore, TRUS is still the most practical and accessible means of examination in many medical environments, especially in biopsy guidance.

With the development of artificial intelligence and medical image analysis technology, computer-aided diagnosis (CAD) systems based on TRUS images have gradually become a research hotspot [16, 17]. By preprocessing TRUS images (such as normalization, despeckle filtering), segmentation, feature extraction and classification modeling, it is expected to improve its stability and diagnostic performance in PCa detection. Although the quality of TRUS images themselves is low, studies have shown that through appropriate image enhancement and feature engineering methods, texture and morphological features with diagnostic value can still be mined from them. In-depth research in this direction not only helps to make up for the shortcomings of TRUS in image recognition, but also provides a practical path for low-cost, non-invasive, and high-throughput intelligent auxiliary diagnosis of PCa. Therefore, TRUS still has an irreplaceable position in the PCa diagnosis system, and how to overcome its image quality limitations and improve its adaptability and reliability in the CAD system is one of the core issues that need to be urgently solved in current image analysis and auxiliary diagnosis research.

Based on the above background, with the increasing demand for early diagnosis and precise treatment

of PCa, in recent years, researchers have gradually shifted their focus from traditional invasive methods to more non-invasive, efficient and intelligent auxiliary diagnosis technologies. Especially in the field of medical imaging, with the rapid progress of image processing technology and artificial intelligence algorithms, how to fully tap the potential information resources in clinical routine images (such as TRUS images) has become a key breakthrough in promoting the development of early identification and risk assessment of PCa in the direction of precision.

In this context, the computer-aided diagnosis (CAD) system based on image feature extraction has gradually become a research hotspot [17]. The systems proposed so far in the literature [16, 18] aims to automatically analyze medical image data, extract quantifiable image features from it, assist doctors in identifying lesion areas, assessing disease grading, and formulating individualized treatment plans. Compared with the traditional manual interpretation of images, the CAD system has the advantages of strong objectivity, high repeatability, and fast processing efficiency, which can effectively reduce subjective errors and improve the recognition rate of early lesions [19].

Especially in TRUS image analysis, due to its convenient acquisition, real-time imaging, and low cost, it is widely used in clinical practice. How to improve the efficiency of its image information utilization is particularly important. Studies have found that TRUS images contain a large amount of grayscale changes, structural textures, and spatial distribution information [16, 17]. If they can be extracted and analyzed through reasonable feature engineering methods, it is expected to make up for the shortcomings of the original image, such as poor contrast and structural blur. Among many image features, texture features, as an important parameter reflecting the grayscale distribution, structural complexity, and local spatial relationship of the image, have been widely used in the automatic identification of prostate lesions, tumor grading, and the development of non-invasive biomarkers [20].

Studies have shown that texture features extracted from TRUS images, such as grayscale co-occurrence matrix (GLCM), grayscale run length matrix (GLRLM), grayscale size zone matrix (GLSZM), etc., can distinguish cancerous tissue from benign tissue to a certain extent, and their classification performance under certain conditions can even be comparable to high-level imaging methods such as mpMRI [21]. These research results provide theoretical support and methodological basis for the construction of auxiliary diagnosis systems based on TRUS images.

However, it should be pointed out that the inherent imaging noise (such as speckle noise) [22], insufficient tissue contrast, blurred boundaries and other problems of TRUS images will seriously affect the stability and repeatability of texture features, and thus affect the reliability of model training and the generalization ability of classification performance [23]. Therefore, image pre-processing has become a key step in the construction of CAD systems. Common pre-processing methods include image normalization [24], spatial filtering (such as median filtering, non-local mean filtering, bilateral filtering, etc.), denoising and enhancement [25], etc. These methods can effectively improve image quality, enhance the expression of lesion area information, and improve the robustness of subsequent feature extraction and classification [23].

At present, the comparative analysis of texture features based on different preprocessing strategies as also presented in this thesis, is becoming an important research direction. By evaluating the performance of features extracted under different image processing conditions in terms of classification accuracy, feature stability, reproducibility, etc., it is expected to screen out more robust and clinically practical feature

parameters, and further optimize the application efficiency and credibility of TRUS images in auxiliary diagnosis. This type of research can not only provide methodological support for the establishment of a low-cost, non-invasive, and scalable intelligent auxiliary diagnosis framework for PCa, but also help promote the translational application of radiomics and artificial intelligence in the clinical practice of PCa.

## 1.1 Aims and Objectives

This study aims to improve the accuracy and stability of PCa diagnosis by analyzing the texture features of transrectal ultrasound (TRUS) images(see also Fig.4.1). TRUS, as an imaging technology with real-time imaging, low cost and easy access, has been widely used in clinical PCa screening and biopsy guidance. However, due to its limited image quality, such as severe speckle noise, poor tissue contrast and blurred boundaries, the computer-aided diagnosis (CAD) system based on TRUS images still faces challenges in practical applications. Therefore, improving the resolvability of TRUS images and the stability of feature extraction has become a key path to realize its intelligent diagnostic potential [17].

This study will systematically evaluate the effects of various image preprocessing strategies on improving image quality in response to the common noise and image quality fluctuation problems in TRUS images. Specifically, it includes image normalization(N) and a variety of advanced denoising filtering methods, such as Non-Local Means Filtering (NLMF), Wiener Filtering (WF) and Median Filtering (MF) [26]. The study will combine multiple image quality assessment indicators (such as peak signal-to-noise ratio PSNR, structural similarity SSIM, root mean square error RMSE and contrast-to-noise ratio CNR) to quantitatively analyze each method to screen out the optimal preprocessing strategy that can effectively suppress noise and retain lesion details [27].

Based on the high-quality images obtained after preprocessing, the study will further use mature statistical methods to extract texture features [28]. The selected features include Gray-Level Co-occurrence Matrix (GLCM) and Gray-Level Size Zone Matrix (GLSZM), which are used to describe key information such as grayscale distribution, structural heterogeneity and spatial relationship within the tissue. Subsequently, the performance of these features under different preprocessing methods was evaluated by stability analysis methods (such as variance analysis, correlation coefficient comparison, etc.) to determine which features can still maintain stability and diagnostic consistency under various image conditions, thus having potential biomarker value [29].

Based on the comprehensive extraction and evaluation of feature stability, the study will combine statistical analysis methods (such as Mann–Whitney U test, linear regression, etc.) to screen the significance of various features and screen out key features that have distinguishing power between benign and malignant prostate lesions [20].

Following the stability-based feature selection process (including the Mann–Whitney U test and linear regression), the selected features are used to train machine learning classifiers (e.g., Support Vector Machines) to validate their ability to distinguish benign from malignant prostate lesions. This classification modeling step quantifies the diagnostic performance of the proposed image preprocessing and feature extraction pipeline. In particular, evaluation of metrics such as accuracy and robustness demonstrates the practical utility of the pipeline in identifying clinically relevant lesion types.

Finally, this study aims to provide a more robust and efficient image processing and feature extraction process for the application of TRUS images in the auxiliary diagnosis of PCa, and provide technical support for the development of TRUS-based CAD systems. The research results are expected to promote the transformation of TRUS image analysis from experience dependence to standardization and intelligence in the future, especially in areas with limited resources and inability to widely use mpMRI, providing a low-cost, non-invasive, and automated PCa screening solution, which has important clinical application value and promotion prospects.

## 1.2 Research Questions

This study seeks to explore the impact of various image preprocessing techniques on the quality and texture feature stability of transrectal ultrasound (TRUS) images. Specifically, it addresses the challenges of balancing noise reduction with the preservation of diagnostic information and aims to provide insights into the most effective preprocessing methods for texture-based analysis.

A key question guiding this research is how different preprocessing techniques, such as N and filtering, influence the overall quality of TRUS images. Metrics like PSNR, SSIM, RMSE, and CNR [27] are used to quantitatively evaluate the performance of these methods, with an emphasis on retaining critical structural details while minimizing noise interference.

Another important question focuses on the stability of texture features extracted from TRUS images subjected to different preprocessing workflows. By examining features derived from statistical methods, such as Gray-Level Co-occurrence Matrix (GLCM) and Gray-Level Size Zone Matrix (GLSZM), the study aims to understand the extent to which preprocessing impacts the consistency and reliability of feature extraction.

Finally, the research explores which combinations of preprocessing methods yield the most robust and reproducible texture features. This involves a comparative analysis of different approaches to identify those that offer the greatest potential for enhancing the utility of TRUS images in future applications, particularly in supporting advanced image analysis frameworks.

## 1.3 Contribution

This study makes a significant contribution through the comprehensive analysis of texture features stability across different preprocessing workflows. By examining features derived from statistical models like Gray-Level Co-occurrence Matrix (GLCM) and Gray-Level Size Zone Matrix (GLSZM), the research identifies robust features that are less affected by variations in preprocessing. This not only advances our understanding of features reliability but also provides valuable guidelines for feature selection in future studies. The study also confirms the advantages of N, D and ND in enhancing the quality and stability of PCa texture features. The findings provide valuable insights into optimizing preprocessing techniques to improve the diagnostic accuracy and robustness of feature extraction in PCa CAD systems. Although this study establishes a foundation for optimizing preprocessing strategies, further research is needed to explore feature clustering patterns and assess the generalizability of identified features across different filtering methods. Expanding the dataset to include healthy prostate images and integrating multi-modal

imaging approaches, such as ultrasound and MRI, could further enhance the stability, reliability, and clinical applicability of PCa CAD systems.

## 1.4 Structure of the Thesis

The present is structured as follows:

Chapter 1: Introduction, where an introduction to the clinical problem is given along with a literature review on the subject of study.

Chapter 2: Literature Review is presented listing recent methods reported in the literature.

Chapter 3: In this chapter we present the Materials and Methods and more specifically, the acquisition of TRUS images, image intensity normalization and the different types of noise that appear in these images along with their accompanying filtering methods for removing it.

Chapter 4: In Results we present the results of the study in form of images, tables, and graphs.

Chapter 5: In Conclusion section we present again the objective of the study, its innovation and perform a Discussion between our study with all other studies reported in the literature. Finally we present the conclusions and the future directions.

## 1.5 Summary

This thesis begins by providing an overview of the research background, highlighting the significance of texture analysis in transrectal ultrasound (TRUS) imaging and the need for robust preprocessing methods. It establishes the aims, objectives, and research questions that guide the study, setting the foundation for subsequent chapters.

Following the introduction in Chapter 1, the thesis explores existing literature on TRUS imaging and texture feature extraction. A detailed review presented in Chapter 2, of preprocessing techniques is conducted, focusing on their influence on image quality and feature stability. This review identifies key gaps and limitations in current research, framing the context for the proposed study.

The methodology which is presented in Chapter 3, details the systematic approach undertaken in this research. It describes the processes of image acquisition, normalization, and filtering, alongside the statistical methods used to evaluate texture feature stability. This chapter ensures transparency and reproducibility, offering a comprehensive explanation of the experimental design.

The results and discussion are presented in Chapter 4, and provide detailed information on the findings of the study, including the comparative performance of different preprocessing techniques and their impact on texture feature consistency. The discussion interprets these results in the context of existing research, providing new insights into the optimization of TRUS image preprocessing for texture-based analysis.

Finally, the thesis concludes with Chapter 5 by summarizing the key contributions of the study and discussing its broader implications. Limitations are acknowledged, and recommendations for future research are provided, emphasizing the importance of continued exploration in this field.

At the end of the thesis, bibliographic references are provided, along with an appendix containing a list of the 318 selected stable texture features.

## 2 Literature Review

For radiologists, physicians, and medical experts, the presence of noise in medical imaging presents a significant challenge. Noise can compromise critical information within an image, which may play a pivotal role in disease diagnosis. In digital imaging, fundamental noise types include speckle noise, salt-and-pepper (impulse) noise, Poisson noise, and Gaussian noise [30]. Noise can lead to severe issues in medical image processing, such as blurred edges, indistinct organs or regions, and the introduction of new artifacts. Therefore, noise removal is a crucial pre-processing step to ensure accurate and reliable analysis in subsequent stages of image processing. Yu et al. [31] proposed a Laplacian Eigenmaps Network-Based Nonlocal Means (LEP-NLM) method for denoising MR images corrupted by Rician noise. The method integrates a shallow convolutional network (LEPNet) with nonlocal means (NLM) filtering. LEPNet extracts structural features from pre-denoised images to refine similarity weights in NLM, improving noise reduction while preserving details. Wong et al. [32] developed a Monte Carlo-based despeckling method specifically designed for TRUS images of the prostate affected by speckle noise. The method incorporates the circular probe acquisition characteristics and speckle noise statistics into a likelihood-weighted Monte Carlo estimation framework, enabling effective noise suppression while preserving critical anatomical structures. Validated through both *in silico* and *in vivo* experiments, the proposed method outperformed conventional techniques, achieving an S-SNR of 22.84 dB, CNR of 9.68 dB, and resolution gain of 1.98, thereby enhancing lesion contour delineation crucial for prostate cancer diagnosis and treatment planning.

A number of studies have been reported in the literature where texture features were used to classify structures in prostate TRUS images. More specifically, Scheipers et al. [33] proposed an ultrasonic multifeature tissue characterization system for the early detection of PCa using TRUS radio-frequency (RF) data. The study extracted up to 40 parameters per prostate segment, including spectral features, attenuation metrics, and first- and second-order texture descriptors. After parameter reduction via covariance analysis, two parallel adaptive fuzzy inference systems (FIS) were employed to classify tissue as benign or malignant. A morphological postprocessing step was applied to generate malignancy maps overlaying B-mode images, enhancing visualization for clinicians. In a clinical study involving 100 patients and 170,000 annotated segments, the system achieved ROC curve areas of 0.83 and 0.76 for tumors visible and non-visible in B-mode imaging, respectively, with a classification accuracy of 75%. Despite its promising diagnostic capabilities, the study has several limitations. The method is highly dependent on handcrafted features and specific ultrasound equipment settings, potentially limiting generalizability. Additionally, while the system effectively visualized malignancy probabilities, it did not incorporate advanced preprocessing techniques such as speckle noise reduction, which could improve feature reliability. The fixed fuzzy logic framework may also lack adaptability to complex or unseen data patterns. Future enhancements could include integrating machine learning-based feature selection, denoising pipelines, and expanding validation across diverse imaging platforms to improve robustness and clinical utility.

Mohamed et al. [34] proposed a texture-based segmentation method for PCa diagnosis using TRUS images, leveraging multi-channel Gabor filtering. The study aimed to address the challenges of distinguishing cancerous from healthy prostate tissue by mimicking the human visual system (HVS) through texture analysis, focusing on repetition, directionality, and complexity. A bank of Gabor filters was designed

to cover various spatial frequencies and orientations, enabling effective decomposition of TRUS images into discriminative texture features. The magnitude response of filtered outputs was smoothed using Gaussian functions to enhance segmentation quality, followed by K-means clustering to classify texture regions. Experimental results on both synthetic texture images and TRUS data demonstrated that high-frequency Gabor filters effectively highlighted detailed structures within the prostate, producing distinct segments potentially indicative of cancerous regions. Despite promising segmentation performance, the study has notable limitations. The approach relies on unsupervised clustering without explicit identification of cancerous tissues, requiring further pathological correlation to validate diagnostic relevance. Additionally, while smoothing improved intra-texture consistency, excessive smoothing risked blurring critical boundaries. The method also lacked advanced preprocessing steps, such as speckle noise reduction, which could further refine texture feature extraction in noisy TRUS environments. Future work should focus on integrating clinical labels, enhancing noise robustness, and developing automated strategies for distinguishing malignant from benign segments.

Llobet et al. [35] proposed a CAD system for PCa using TRUS images, aiming to improve early diagnosis through texture analysis and machine learning techniques. The study utilized a large, unbiased dataset of 4,944 TRUS images from 303 patients, making it one of the most extensive corpora in this domain. Two classification approaches were evaluated: k-nearest neighbors (k-NN) and Hidden Markov Models (HMM), using features extracted via spatial gray-level dependence matrices (SGLDM) and gray-level maps. The best classification performance achieved an area under the ROC curve (AUC) of 61.6%, indicating modest but positive discrimination between cancerous and non-cancerous tissues. Additionally, a clinical evaluation involving urologists showed that the CAD system slightly improved diagnostic accuracy for inexperienced users but provided limited benefit for experts. Despite its contributions, the study faced several limitations. The system's diagnostic performance was constrained by imperfect pixel-level labeling due to the nature of biopsy-based ground truth. Moreover, the CAD framework did not incorporate advanced preprocessing techniques, such as speckle noise reduction, which could enhance texture feature reliability in TRUS images. The reliance on handcrafted features and classical classifiers further limited adaptability to complex patterns. Future improvements could focus on integrating denoising pipelines, deep learning-based feature extraction, and validation across diverse datasets to enhance clinical applicability and robustness.

Han et al. [36] proposed a computer-aided PCa detection method using multiresolution autocorrelation texture features combined with clinical features in TRUS images. The study analyzed 51 TRUS images, where texture features were extracted using autocorrelation at multiple resolutions to capture self-similarity patterns of tissues. Additionally, clinical features, including tumor location (favoring the peripheral zone) and shape (elliptical likelihood), were integrated to enhance diagnostic accuracy. A Support Vector Machine (SVM) classifier was employed to distinguish cancerous from benign tissues. The proposed method achieved high performance, with sensitivity ranging from 92% to 96% and specificity between 91.9% and 95.9%, outperforming previous texture-only approaches. Despite its strong results, the study has several limitations. The preprocessing relied on histogram equalization for prostate segmentation, which achieved only 75% boundary accuracy, potentially impacting feature extraction. Furthermore, the method's effectiveness was validated on a relatively small and homogeneous dataset, raising concerns about its generalizability to larger or more diverse populations. The approach also did not address speckle

noise reduction explicitly, which may affect texture reliability in TRUS images. Incorporating advanced denoising techniques and validating on broader datasets would be essential to enhance robustness and clinical applicability.

Moradi et al. [37] proposed a novel computer-aided detection (CAD) method for prostate cancer (PCa) in transrectal ultrasound (TRUS) images by leveraging ultrasound radio-frequency (RF) time series analysis combined with an extended support vector machine (SVM) classifier. Unlike traditional approaches that rely on static spectral or texture features, this method captures sequential RF echoes from stationary tissue to extract dynamic tissue-specific signatures influenced by microstructural properties. In a study involving 35 ex vivo prostate specimens, the authors demonstrated that RF time series features significantly outperformed conventional Lizzi-Feleppa (LF) spectral features and B-mode texture features. The hybrid feature set, combining RF time series, LF, and texture features, achieved an area under the ROC curve (AUC) of 0.95 in tenfold cross-validation and 0.82 in leave-one-patient-out validation. The system generated probabilistic cancer maps to guide biopsy targeting, potentially reducing false negatives. Despite its strong performance, the study has limitations. The approach requires the probe and tissue to remain stationary for several seconds, posing challenges for in vivo applications without stabilization mechanisms. Additionally, while RF time series analysis inherently mitigates some noise effects, explicit speckle noise reduction techniques were not integrated, which could further enhance feature robustness. The dataset was limited to ex vivo specimens, necessitating future in vivo validation. Optimization for real-time clinical workflows and broader generalization across ultrasound systems remain areas for further development.

Maggio et al. [38] proposed a CAD system for PCa based on TRUS images, integrating predictive deconvolution and hybrid feature selection to enhance diagnostic accuracy. The study addressed system-dependent artifacts and speckle noise by applying a predictive deconvolution technique to raw RF signals, effectively improving image quality and feature reliability. A comprehensive set of 54 spectral, statistical, and textural features was extracted, and a mutual information-based hybrid feature selection (MIHFS) algorithm was employed to reduce dimensionality while retaining discriminative power. The classification framework combined Generalized Discriminant Analysis (GDA) with a Fisher Linear Discriminant (FLD) for nonlinear feature projection and linear decision-making. Tested on TRUS images from 37 patients (15 benign, 22 malignant), the CAD system achieved a sensitivity of 90%, specificity of 93%, and AUC of 95% after deconvolution, outperforming models without preprocessing. Predictive deconvolution notably enhanced the diagnostic value of texture features by reducing speckle noise and system artifacts. Despite its strong performance, the study has limitations. The dataset size was relatively small, and the reliance on biopsy-based ground truth introduced potential labeling inaccuracies due to the multifocal nature of PCa. Additionally, while deconvolution improved feature robustness, the computational complexity remains a barrier for real-time clinical deployment. Future work could focus on optimizing processing speed, validating on larger datasets, and integrating advanced machine learning techniques to further enhance generalizability and clinical applicability.

Huang X et al. [39] proposed a texture feature-based classification method for TRUS images aimed at detecting PCa. The authors analyzed 342 histologically confirmed TRUS images and extracted two main texture features: Local Binary Patterns (LBP) to capture local texture details and Gaussian Markov Random Field (GMRF) to model pixel dependencies. These features were combined linearly to enhance

classification performance. To improve image quality, the authors applied optical density transformation for preprocessing, effectively increasing contrast and reducing noise. A Support Vector Machine (SVM) classifier was employed for classification, achieving an accuracy of 70.93%, sensitivity of 70.00%, and specificity of 71.74%. The study demonstrated the advantage of combining multiple texture features over single-feature methods and alternative classifiers, such as KNN and Random Forest, in detecting PCa in TRUS images. Despite its strengths, the study has several limitations. The preprocessing method applied does not sufficiently address speckle noise inherent in TRUS, which can obscure fine texture details. Additionally, the linear combination of features lacks a rigorous evaluation of their stability and significance. While the authors focused on a single preprocessing method (optical density transformation), other techniques, such as normalization and filtering pipelines (e.g., N-WF, N-NLMF), could further improve the diagnostic robustness of texture features.

Wei et al. [40] developed a classification method for distinguishing benign and malignant breast tumors in ultrasound images by combining texture and morphological features. Using a dataset of 448 denoised and equalized ultrasound images, three texture features—Local Binary Patterns (LBP), Histogram of Oriented Gradients (HOG), and Gray-Level Co-occurrence Matrix (GLCM)—were extracted alongside three morphological features, including compactness, elliptical compactness, and radial distance spectrum. The study utilized SVM for texture features and Naive Bayes (NB) for morphological features. A weighted fusion of these classifiers achieved 91.11% accuracy, 94.34% sensitivity, and 86.49% specificity, outperforming single-feature methods. Although this method achieved high accuracy, the study's preprocessing steps, such as anisotropic diffusion filtering and histogram equalization, are limited in their ability to handle ultrasound's persistent speckle noise. Furthermore, the stability and diagnostic relevance of the extracted texture features were not thoroughly assessed. Systematic evaluations of texture features extracted from images processed with advanced preprocessing pipelines (e.g., normalized and filtered images) could provide more robust insights. Additionally, the absence of quantitative image quality metrics (e.g., PSNR, SSIM, and CNR) hinders a comprehensive assessment of preprocessing efficacy.

Bhattacharya et al. [41] proposed MIC-CUSP (Multimodal Image Correlations for Cancer detection on UltraSound leveraging Pretraining with weak labels), an automated prostate cancer detection method based on transrectal b-mode ultrasound (TRUS) images. Recognizing the limitations of TRUS, such as low signal-to-noise ratio and artifacts like speckle and shadowing, the authors designed MIC-CUSP to enhance cancer detection by leveraging multimodal image correlations without requiring spatial registration. The method integrates richer imaging-inspired ultrasound biomarkers derived from unaligned MRI and histopathology images through a registration-independent learning framework. MIC-CUSP employs a 3D-UNet-based architecture with deep supervision and combines weakly-labeled public datasets (1573 scans) with strongly-labeled internal data (289 patients) for pretraining and fine-tuning. Evaluated on 41 patients, MIC-CUSP achieved a patient-level sensitivity of 65% and specificity of 81%, outperforming the average performance of four clinician-readers with 1–12 years of experience. Despite its promising results, MIC-CUSP's reliance on advanced deep learning frameworks and multimodal data during training may limit immediate clinical deployment in settings lacking such resources. Furthermore, while the method addresses noise and artifact challenges indirectly through biomarker learning, explicit denoising techniques, such as normalization and filtering (e.g., N-WF, N-NLMF), were not explored, which could further enhance robustness in diverse clinical environments.

Fang et al. [42] proposed an automated anatomical landmark detection method to initialize ultrasound (US) and magnetic resonance (MR) image registration for prostate cancer interventions. Recognizing that manual landmark detection or prostate segmentation is time-consuming and challenging during MR/US fusion biopsies, the authors developed a deep learning-based pipeline to detect three key anatomical landmarks (apex, bladder neck, and posterior median) in both modalities. The method employs a 3D U-Net combined with a differentiable spatial to numerical transform (DSNT) layer for direct coordinate regression, avoiding traditional heatmap or fully connected layer-based approaches. Trained on 900 cases and validated on 152 cases, the system achieved mean radial errors (MRE) of  $5.55 \pm 2.63$  mm for US and  $5.77 \pm 2.67$  mm for MR images across 263 test cases. A least-squares fitting algorithm was then applied to compute a rough rigid transformation for initial alignment. The method achieved a surface registration error (SRE) of  $6.62 \pm 3.97$  mm and a Dice score of  $0.77 \pm 0.11$ , demonstrating clinically comparable performance to manual landmark-based registration.

Despite its efficiency, the study has limitations. The robustness of the automated detection was affected by variations in US image quality, partial prostate views, and large deformations. Additionally, the approach did not explicitly address noise reduction or artifact handling in US images, which could impact landmark detection accuracy. Future work could focus on integrating preprocessing techniques, such as speckle noise filtering, and enhancing model generalization across diverse imaging conditions.

All above studies reviewed highlight the significant potential of texture feature analysis in detecting and predicting PCa. However, a recurring limitation is the lack of focus on ultrasound imaging, which is more cost-effective and accessible than MRI but suffers from inherent challenges such as speckle noise and lower contrast. Additionally, the impact of preprocessing pipelines (e.g., normalization and filtering) on texture feature stability and diagnostic performance remains underexplored. The absence of quantitative image quality metrics further limits a comprehensive evaluation of preprocessing methods.

Given these gaps, there is a critical need to explore texture analysis in PCa TRUS images based on different preprocessing schemes. By systematically comparing texture features extracted from normalized (N), despeckled (D), and combined normalized-despeckled (ND) images, this research can identify the most stable and diagnostically relevant features. Integrating advanced preprocessing techniques, such as NLM filtering and Wiener filtering, with robust statistical evaluations will enhance the diagnostic accuracy of ultrasound-based texture analysis.

# 3 Research Methodology

This chapter provides a detailed description of the methodology adopted in this study, where all steps followed are depicted in Fig. 3.1. It starts with the acquisition of ultrasound images, then discusses the types of image noise which corrupts ultrasound images, and introduces the major corresponding filtering methods. Furthermore, a segmentation algorithm for extracting the prostate area is presented, followed by the extraction of texture features, where a number of features and quality metrics are presented. The chapter also includes the classification modeling, which is used to select the most appropriate features for the models generation.

## 3.1 Acquisition of Ultrasound Images

Medical TRUS images were acquired for this study using both ultrasound and MRI modalities at the German Oncology Center, Nicosia, Cyprus (see Figure 4.1). It should be noted, however, that in this study the MRI images were not used for the proposed analysis. The images were acquired in the context of high dose-rate brachytherapy (HDR-BRT), which involves the transperineal implantation of multiple catheter needles into the patient's prostate, facilitating the temporary placement of a radioactive source directly into the tumor site [43]. The flow diagram presented in Fig. 3.1 presents the integrated system proposed in this study, where all different steps are herebelow described.

A total of  $N_p = 8$  patients with prostate enlargement and initial PCa symptoms participated in the study, referred by their personal doctors (see also Figure 4.1, step 1). From these subjects,  $N_r = 576$  TRUS images were acquired. The ultrasound examinations were conducted using a BK Medical bk3000 ultrasound system equipped with an E14CL4b (9048) endocavity biplane transducer, providing high-resolution  $512 \times 512$  pixel B-mode images. The TRUS data included standard B-mode scans, transverse images, and transrectal views of the prostate, captured in a sequential fashion from the cranial to the caudal end of the gland. This comprehensive imaging approach ensured full coverage of the prostate volume.

In parallel, MRI scans were acquired for anatomical reference and registration purposes using a GE Signa HDxt + SW 1.5T MRI scanner. Two types of T2-weighted Fast Spin Echo (FSE) axial images were obtained as follows:

- Standard MRI:  $512 \times 512$  resolution, voxel size of 3 mm.
- Parametric MRI (pMRI):  $512 \times 512$  resolution, with a finer 1.5 mm voxel size for enhanced detail.

Additionally, high-resolution T2-weighted sequences with  $1024 \times 1024 \times 48$  voxels, 0.2148 mm in-plane resolution, and 1.5 mm slice thickness were used to improve the spatial definition of the prostate anatomy. These MRI images provided valuable anatomical context and were initially spatially registered to the TRUS images to align the prostate domain across modalities, even though they were not used in the final analysis.

All procedures complied with ethical standards, and informed consent was obtained from all participants prior to imaging.

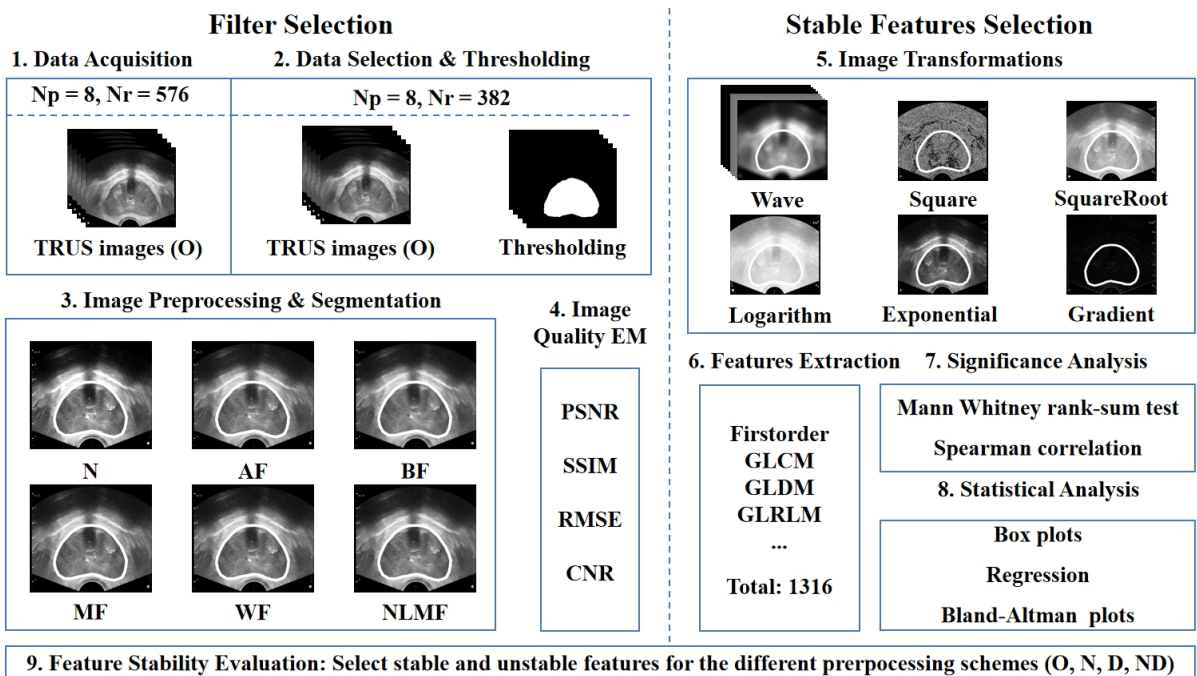


Figure 3.1: Flow diagram of the integrated system as proposed in this study for the PCa ultrasound texture analysis. (1) Data Acquisition (TRUS) Images, (2) Data Selection & Segmentation, (3) Image Preprocessing, transformation, (4) Image Quality Assessment & Selection and evaluation metrics, (5) Image transformations, (6) Features extraction, (7) Significance analysis (8) Statistical analysis, (9) Identify stable vs unstable features for the different preprocessing schemes. Np: Number of patients, Nr: Number of images, O: Original images, N: Normalization, AF: Average Filtering, BF: Bilateral Filtering, MF: Median Filtering, WF: Wiener Filtering, NLMF: Non-Local Means Filtering, EM: Evaluation metrics, PSNR: Peak Signal-to-Noise Ratio, SSIM: Structural Similarity Index Measure, RMSE: Root Mean Square Error, CNR: Contrast-to-Noise Ratio, GLCM: Gray-Level Co-occurrence Matrix, GLDM: Gray-Level Dependence Matrix, GLRLM: Gray-Level Run Length Matrix, D: Des-peckle, ND: normalization and despeckle.

## 3.2 Types of Image Noise

For radiologists, clinicians, and technical experts in the field of medical ultrasound imaging, medical images are inevitably interfered by various noises during the acquisition, transmission, and processing, which greatly affects the image quality and its diagnostic value [44, 45]. Medical images are often used to identify early lesions, guide the formulation of treatment plans, and evaluate the treatment effect, so the clarity and detail fidelity of the image are crucial [46]. Noise not only masks the true characteristics of the lesion, but also may lead to misjudgment or missed diagnosis, especially in scenes that rely on high-precision images to judge small differences such as boundaries, density, and texture.

The sources of image noise are multifaceted. First, the hardware limitations of the imaging device itself, such as thermal noise, dark current noise, and readout circuit noise in the sensor, will introduce a certain degree of interference in the original image. Second, defects in the optical system, such as lens distortion, scattering, or diffraction effects, may also cause signal distortion [47]. In addition, during the image acquisition process, if the signal sampling frequency is insufficient, high-frequency signal aliasing will occur, further reducing the image quality. The quantization error introduced in the digitization process of

the analog signal will inevitably introduce noise components [48].

In the storage and transmission stage of medical images, due to the limitation of bandwidth resources or storage capacity, images usually need to be compressed to improve efficiency. Although the commonly used image compression algorithms such as JPEG2000 can significantly reduce the size of image files, they use lossy compression methods, which may introduce compression artifacts and blocking artifacts during image reconstruction, thereby damaging image quality [49]. In addition, during remote or wireless transmission, due to channel instability or packet loss, communication errors may further lead to incomplete image data, affecting the clarity and availability of the final received image [44]. In digital image processing, medical images are often interfered by various noises, which not only blur image details, weaken edge contrast, and make organ contours difficult to distinguish, but also introduce pseudo-features, affecting the accuracy of subsequent image analysis tasks such as segmentation, registration, feature extraction and classification.

Therefore, in the preprocessing stage of medical images, it is a crucial step to adopt effective denoising technologies [50, 51]. An ideal denoising algorithm should be able to remove noise as much as possible while retaining the structural details, edge information and texture features in the image to ensure the accuracy of subsequent image segmentation, feature extraction, classification and diagnostic analysis [51, 52]. For a visual comparison, refer to Fig. 4.1, where subfigure a) shows the original US PCa image and Fig. 4.1 f) displays the image after N and Non-Local Means Filtering (NLMF), illustrating the impact of preprocessing (i.e. normalization and filtering)..

Common noise types include [53]: Speckle Noise: widely present in ultrasound images, caused by coherent interference of sound wave reflection signals; Salt and Pepper Noise: manifested as randomly distributed black and white dots in the image, usually caused by transmission errors or sensor abnormalities; Gaussian Noise: mainly derived from electronic components or environmental interference in the imaging system, and is one of the most common random noise models; Poisson Noise: common in low-dose imaging (such as X-ray or nuclear medicine images), caused by statistical fluctuations in the number of photons.

The following will introduce in detail the causes, characteristics and modeling methods of several major types of noise related to this study:

### 3.2.1 Speckle Noise

Speckle noise is the most representative type of noise in ultrasound images. It is caused by the coherent superposition of multiple reflected waves and belongs to multiplicative noise. It generates pseudo-structures in the image that depend on the local grayscale value, which appears as a granular texture, reducing the image contrast and blurring the edges, thereby affecting the detection and identification of the lesion area [54]. Unlike additive Gaussian noise, speckle noise has a non-Gaussian distribution characteristic, so it is difficult for traditional linear filters to effectively suppress this type of noise [55].

In theoretical modeling, speckle noise is often described by Rayleigh distribution, gamma distribution or log-normal distribution [56]. For ease of processing, ultrasound images are often logarithmically transformed in clinical practice to convert multiplicative noise into additive noise, so that image quality can be improved with the help of processing methods under additive noise. Its mathematical expression

is as follows:

$$\ln[g(x, y)] = \ln[g_0(x, y)n(x, y)] = \ln[g_0(x, y)] + \ln[n(x, y)] \quad (3.1)$$

Among them,  $g(x, y)$  represents the original image signal, and  $n(x, y)$  represents the multiplicative noise component. In this way, the multiplicative noise is converted into additive noise that can be approximated as a Gaussian distribution, which is convenient for denoising using classical image processing methods. The transformed image can be approximately modeled as an image with Gaussian noise, which is convenient for subsequent denoising using methods such as wavelet filtering, median filtering, non-local mean (NLM), etc [57].

Speckle noise has a significant impact on medical image analysis. It can reduce image contrast and clarity, blur tissue boundaries, and has a particularly severe impact on soft tissues. It also introduces pseudo-structures and pseudo-textures, misleading segmentation and recognition algorithms and affecting the accuracy of lesion detection. It can also affect quantitative analysis and texture feature extraction, increasing the difficulty of training machine learning models.

### 3.2.2 Salt and Pepper (Impulse) Noise

Salt and pepper noise, also known as fixed-valued impulse noise (FVIN), is one of the most common non-Gaussian noise types in image processing. It appears as randomly distributed black (grayscale value 0) and white (grayscale value 255) pixels in the image, resembling "sprinkled salt and pepper", hence the name. This type of noise is usually caused by sensor failure, signal interference, storage damage, or bit errors during data transmission [58–60].

Salt and pepper noise has many effects on image quality. It will destroy local structures, and the mutation pixels will cover up the original texture and details, especially in the lesion area, which will affect the accuracy of the doctor's naked eye observation and image segmentation. In addition, due to the drastic changes in the intensity of the noise points, the edges are blurred or misdetected, which may be mistakenly identified as real edges by the edge detection algorithm. In addition, salt and pepper noise will interfere with the weight learning process, reduce classification or detection performance, and affect the learning effect of the machine model.

Salt and pepper noise has a great impact on image details, destroys local structures and edge features, and poses a challenge to subsequent image enhancement, edge detection and lesion localization algorithms. Due to the non-Gaussian and strong nonlinear characteristics of this noise, traditional linear filters (such as mean filtering) are difficult to effectively remove, but will introduce a blurring effect. Therefore, median-based nonlinear filters such as standard median filtering, adaptive median filtering, and hybrid median-mean filtering are often used to retain edges and reduce the impact of noise.

### 3.2.3 Gaussian Noise

Gaussian noise is the most common and widely studied type of additive random noise in medical image processing. It is prevalent in a variety of imaging devices, especially in magnetic resonance imaging (MRI), computed tomography (CT), X-ray imaging, and digital camera systems. [61]

Gaussian noise mainly comes from the following sources: electronic thermal noise: random thermal motion of electrons inside the imaging sensor at high temperatures; readout circuit noise: fluctuations in the

analog-to-digital converter (ADC) during image acquisition and digitization; environmental electromagnetic interference: such as electromagnetic radiation from equipment in hospitals, power supply system fluctuations, etc.; photon counting error: photoreceptor unstable reception of photons under low contrast or low illumination conditions. These factors cause the grayscale value of the pixel to fluctuate randomly around its true value, resulting in noise from the image that is consistent with the normal distribution [62]. Gaussian noise affects the pixel intensity values in an image, causing deviations from their true values and significantly degrading image quality. This is particularly detrimental in tasks such as feature extraction and object recognition, where its random nature can obscure fine details and edge information. Gaussian noise is a typical representative of additive noise, and its mathematical expression is:

$$g(x, y) = f(x, y) + n(x, y) \quad (3.2)$$

where  $f(x, y)$  represents the original, noise-free image, and  $n(x, y)$  denotes the additive Gaussian noise. The probability density function (PDF) of Gaussian noise is defined as:

$$P(g) = \frac{1}{\sqrt{2\pi\sigma^2}} \exp\left(-\frac{(g - \mu)^2}{2\sigma^2}\right) \quad (3.3)$$

Here,  $\mu$  is the mean of the noise (typically zero), and  $\sigma^2$  is the variance, which determines the noise intensity. According to statistical properties, approximately 68% of pixel values fall within the range  $\mu \pm \sigma$ , 95% within  $\mu \pm 2\sigma$ , and 99.7% within  $\mu \pm 3\sigma$  [61].

Gaussian noise can cause image blurring and loss of detail, especially at edges, contours or low-contrast areas, which can easily obscure key diagnostic information. It can also change image statistical features, texture patterns and spatial distribution, thereby affecting the performance of feature-based algorithms and causing a decrease in feature extraction accuracy. In medical image classification, it can cause the model to overfit with erroneous information.

In actual processing, Gaussian noise can be effectively suppressed through methods such as Gaussian filtering, bilateral filtering, wavelet transform, and deep learning to improve image quality and the robustness of subsequent analysis. [51]

### 3.3 Filtering Methods

In order to improve the quality of medical ultrasound images, reduce noise interference and enhance the reliability of diagnosis, researchers have proposed a variety of filtering methods, aiming to effectively remove noise while preserving image edges, tissue structures and lesion features as much as possible. The following are several filtering methods used in this study.(see also Figure 4.1, step 3)

#### 3.3.1 Intensity Normalization

In ultrasound image processing, the grayscale value distribution of the image often fluctuates significantly due to the influence of equipment parameters, acquisition conditions and individual differences of patients. In order to reduce the interference caused by such grayscale instability, intensity normalization is used as an important preprocessing step to standardize the grayscale range of each image.

Intensity normalization is particularly critical for ultrasound images because ultrasound imaging itself has the characteristics of inconsistent grayscale dynamic range, obvious noise interference and strong device dependence. Different scanning equipment, probe types or gain parameters set by the operator may cause large differences in brightness and contrast of the same anatomical structure in different images. If normalization is not performed, these grayscale differences will affect subsequent image analysis processes, such as filtering, segmentation or feature extraction, and may cause the algorithm to misjudge tissue boundaries or misidentify lesion areas [63].

By performing Min-Max normalization on each prostate ultrasound image separately, the problem of inconsistent grayscale distribution caused by differences in acquisition conditions between images can be effectively reduced, and the uniformity of overall contrast can be improved. This standardized grayscale range not only helps to improve the consistency of filter performance on different images, but also enhances the robustness of algorithms based on thresholds or texture features, and avoids performance fluctuations caused by differences in input data distribution.

### 3.3.2 Average Filtering

Average filtering is a simple and effective image smoothing technique. Its basic principle is to calculate the average value of all pixel values in the neighborhood in a fixed-size sliding window (such as  $3 \times 3$ ) and assign this value to the central pixel [64]. This method is intuitive and computationally efficient. In practical applications, it is often used to reduce local intensity fluctuations in images caused by sensor noise or imaging environment.

In medical image processing, especially in prostate ultrasound images, image signals are often interfered with by varying degrees of noise, manifesting as unstable grayscale distributions and significant texture irregularities [65]. Average filtering can alleviate these problems to some extent by improving local consistency and reducing noise-induced variation, thereby stabilizing grayscale transitions and supporting subsequent visual analysis.

However, a significant limitation of average filtering is its lack of edge preservation ability. Since the algorithm assigns equal weights to all pixels in the window, it cannot distinguish between true anatomical boundaries and high-frequency noise, often resulting in blurred contours and loss of detail [50]. This "oversmoothing" effect is particularly prominent when processing regions with complex structures and weak edges, such as the peripheral zone of the prostate.

Therefore, average filtering is more suitable for image scenarios that prioritize smoothness over precise structural preservation. While it provides a straightforward denoising effect, its application must be carefully assessed according to the characteristics of the image and the clinical requirements of the analysis task [66]. In this study, a single-pass average filtering with a  $3 \times 3$  window was applied to the prostate ultrasound images as one of the basic denoising methods. This window size represents a balanced choice: it is small enough to preserve the overall anatomical contours without severely blurring fine structures, while being sufficiently effective in suppressing isolated pixel fluctuations. The one-time application avoids excessive smoothing that may arise from multiple iterations, thus ensuring that essential structural and texture features are retained for downstream analysis.

### 3.3.3 Bilateral Filtering

Bilateral filtering is a nonlinear smoothing method that is widely used in image noise reduction and edge preservation processing tasks. Unlike traditional linear filters (such as mean filtering), bilateral filtering can effectively retain the edges and detail structures in the image while removing noise. The core idea is to perform a weighted average on each pixel. The weight not only considers the proximity of spatial distance, but also combines the similarity of pixel grayscale values, thereby achieving "structure-aware" filtering [67].

The weight calculation of bilateral filtering can be expressed as:

$$I_{\text{filtered}}(x) = \frac{1}{W_p} \sum_{x_i \in \Omega} I(x_i) \cdot f_r(\|I(x_i) - I(x)\|) \cdot f_s(\|x_i - x\|) \quad (3.4)$$

where  $f_r$  is the range kernel based on intensity similarity,  $f_s$  is the spatial kernel based on geometric distance,  $W_p$  is a normalization factor, and  $\Omega$  represents the local filtering window. This mechanism assigns higher weights to pixels that are both spatially close and similar in intensity to the target pixel, enabling edge preservation while reducing irregular noise [68].

In this study, bilateral filtering was applied once (single iteration) across the entire image to denoise prostate ultrasound images while preserving anatomical boundaries. The filtering was performed using a sliding spatial window of size  $d = 7$  (i.e., a  $7 \times 7$  pixel neighborhood centered at each pixel). The color similarity standard deviation  $\sigma_{\text{Color}} = 50$ , and spatial distance standard deviation  $\sigma_{\text{Space}} = 50$ . This configuration enables effective smoothing while preserving the anatomical boundaries in prostate ultrasound images, thus avoiding excessive blurring that could interfere with subsequent analysis [69].

When processing prostate ultrasound images, bilateral filtering is particularly suitable for preserving key areas such as weak boundaries and complex tissue contours, while reducing texture interference caused by speckle noise. Its significant advantage is that it takes into account both image smoothness and structural integrity, making it well adaptable in structure-sensitive medical image processing tasks. Based on its characteristics, bilateral filtering is used as one of the independent denoising methods in this study to evaluate its actual denoising effect in prostate ultrasound images [70].

### 3.3.4 Median Filtering

Median filtering is a common non-linear image smoothing method, which is widely used in the field of digital image processing, especially to remove non-Gaussian interference such as impulse noise (such as salt and pepper noise). Its basic principle is to sort the neighborhood pixel values in a sliding window of a given size and use its median as the new gray value of the current pixel, so as to effectively suppress the influence of outlier pixels on the image.

Compared with linear filtering methods (such as mean filtering), median filtering does not rely on the weighted average of pixels, so it has a stronger advantage in maintaining image edges and details. Since its filtering result only depends on the actual pixel values in the original image, median filtering will not introduce new gray values, effectively avoiding blurring, and is particularly suitable for processing medical images with dense structures in edge areas.

In this study, a  $3 \times 3$  median filter was employed to reduce speckle and impulse noise in prostate ultrasound images. The filtering was applied once (single iteration) across the entire image. The sliding window used in the filtering process was a square neighborhood of size  $3 \times 3$ , centered at each target pixel. Within each window, the pixel intensities were sorted, and the median value was assigned to the center pixel, replacing the original value. This window size helps to retain the grayscale characteristics of anatomical structure boundaries and detail areas in the image while ensuring the noise reduction effect. Considering the possible random noise and local pixel anomalies in ultrasound images, median filtering, with its robustness to outliers, provides a solution with strong structure preservation for image quality optimization. [71]

### 3.3.5 Wiener Filtering

Wiener filtering is a classic filtering method based on statistical optimization theory. Its goal is to retain as much useful information of the original signal as possible while suppressing noise. Unlike traditional methods that directly smooth images, Wiener filtering performs weighted processing in the frequency domain based on the statistical characteristics of signals and noise, which can achieve more sophisticated filtering operations and is particularly suitable for image denoising problems with clear statistical models such as additive Gaussian noise [72, 73].

The design of Wiener filtering is based on the minimum mean square error (MSE) criterion, which aims to build an optimal linear system so that the mean square error between the filtered output signal and the original signal is minimized. Mathematically, the observed signal  $y(t)$  is modeled as the sum of the original signal  $x(t)$  and additive noise  $n(t)$ , i.e.,

$$y(t) = x(t) + n(t) \quad (3.5)$$

The Wiener filter aims to recover an estimate of  $x(t)$  from the noisy observation  $y(t)$ . In the frequency domain, the transfer function of the Wiener filter is defined as:

$$H(f) = \frac{S_x(f)}{S_x(f) + S_n(f)} \quad (3.6)$$

where  $S_x(f)$  and  $S_n(f)$  denote the power spectral densities (PSDs) of the original signal and the noise, respectively. This expression reflects that the filter adaptively retains more signal components in frequency regions with a high signal-to-noise ratio (SNR), while applying stronger attenuation in regions dominated by noise, thus achieving adaptive frequency-domain filtering [74].

In medical image processing, especially in MRI, CT and ultrasound images, Wiener filtering is often used to remove background noise caused by electronic imaging equipment or high-frequency interference during image acquisition. Because it fully considers the statistical relationship between signal and noise, it has a good restoration effect in areas with relatively uniform image quality and clear structural boundaries. However, in areas with complex tissue edges and rich texture changes, Wiener filtering may have problems of over-smoothing or edge weakening. This feature needs to be weighed, especially in tasks with high structural protection requirements [75].

In this study, a fast non-local means (NLM) filter implementation suitable for two-dimensional grayscale

images was used to process prostate ultrasound images. The filtering was applied once (a single iteration) across each image. The method was configured with a patch size of  $3 \times 3$  and a search window size of  $21 \times 21$ . The filter strength parameter was set to  $h = 3$ , which controls the decay of the exponential weighting function used to evaluate the similarity between image blocks.

In the filtering process, for each pixel, similar patches within the  $21 \times 21$  search window were identified, and the filtered pixel value was computed as a weighted average of all pixels in this region. The weights were determined based on the Euclidean distance between the  $3 \times 3$  patches centered on the target pixel and candidate pixels. Higher similarity resulted in higher weight, allowing the filter to enhance repeated structures while reducing noise.

To ensure proper filtering near the edges, symmetric padding was applied to preserve the integrity of patch comparisons at image borders. The implementation was numerically stable, with floating-point computations and safeguards against division-by-zero or invalid operations. Any NaN or infinite values generated during processing were replaced with valid estimations to ensure result availability.

This configuration of non-local means filtering—using a single pass, a  $3 \times 3$  patch, a  $21 \times 21$  search region, and a filter strength of  $h = 3$ —was selected after preliminary testing on several prostate ultrasound datasets. It achieved an effective balance between denoising and structural preservation, particularly in areas with fine tissue textures and weak anatomical boundaries. The method provides reliable visual enhancement while maintaining structural detail critical for subsequent diagnostic analysis.

Overall, Wiener filtering has obvious advantages in improving the overall smoothness of images, and is suitable for medical images with known noise models and relatively stable image statistical characteristics. It has high computational efficiency and simple parameter settings, and the degree of protection of image details depends more on the distribution and estimation accuracy of the actual signal-to-noise ratio [66].

### 3.3.6 Non-Local Means Filtering

Non-local mean filtering (NLM) is an image denoising method with strong structure preservation ability and has important application value in the field of medical image processing. This method makes full use of the non-local redundant structural information in the image, by finding the area similar to the neighborhood of the target pixel in the whole image, and performing weighted averaging based on the similarity between pixel blocks, so as to achieve noise suppression and image detail retention [50].

Most traditional filtering methods rely on the local neighborhood information of pixels. For example, mean filtering or median filtering only considers the grayscale value within a certain range around the target pixel. These methods can smooth the image to a certain extent, but often lead to the loss of image details when processing edge or texture areas. In contrast, non-local mean filtering breaks through the limitation of spatial distance and finds similar image blocks in the whole image for weighted processing, so that the areas with repeated or similar textures in the image can compensate each other, effectively removing noise while retaining more structural information [76].

The fundamental formulation of Non-Local Means filtering is expressed as:

$$\hat{I}(x) = \sum_{y \in \Omega} w(x, y) \cdot I(y) \quad (3.7)$$

where  $\hat{I}(x)$  denotes the filtered pixel value,  $\Omega$  represents the search region within the image, and  $w(x, y)$  is the similarity-based weight between pixel  $x$  and pixel  $y$ , subject to the constraint  $\sum_y w(x, y) = 1$ . The weights are typically computed based on the Euclidean distance between local patches centered at  $x$  and  $y$ , such that higher weights are assigned to more structurally similar regions.

In this study, a fast non-local mean filter implementation suitable for two-dimensional grayscale images was used to process prostate ultrasound images. The filter strength is controlled by the parameter  $h=3$ , which plays a key role in the filtering process and determines the degree of influence of image block similarity in the denoising result.

Specifically, the parameter  $h$  controls the decay rate of the exponential weighted function used to evaluate the similarity of image blocks. When  $h$  is small, the algorithm has stricter requirements on the similarity of image blocks, and only very close image blocks will have a greater impact on the target pixel, which helps to retain more details, but the denoising effect may be limited; on the contrary, a larger  $h$  value relaxes the similarity judgment criteria, allowing more image blocks to participate in the smoothing process, thereby enhancing the denoising ability, but may also cause image structure blur. Based on preliminary tests on multiple groups of images, this study selected  $h = 3$  as the final parameter setting, which achieved a relatively ideal balance between noise suppression and structure preservation, and is suitable for areas with complex structures and rich textures in prostate ultrasound images. This method improves the overall visual quality while maintaining the integrity of the image structure, providing a stable and reliable foundation for subsequent image analysis tasks [77].

Therefore, non-local mean filtering is a highly flexible and effective image denoising method, which is suitable for medical image scenes with complex structures and irregular noise characteristics, and has good adaptability and scalability.

### 3.4 Segmentation Algorithm

The automatic segmentation method of the prostate region as performed in this study refers to the deep learning segmentation framework of Jiale et al. [78]. This method combines image preprocessing with advanced network architecture to achieve high-precision automatic segmentation for the prostate structure in transrectal ultrasound images. The core idea of this method is to effectively improve the robustness of the model to fuzzy boundaries and image noise by reasonably designing the image preprocessing process [79,80], thereby enhancing the stability and accuracy of the segmentation effect (see also Figure 4.1, step 3).

Specifically, before entering the deep learning model, the image is processed into four forms: original image (Original, O), intensity normalized image (Normalized, N), despeckled image (Despeckled, D), and normalized and despeckled image (ND) [78–80]. Intensity normalization unifies the image grayscale distribution by linearly adjusting the bright and dark pixel values of the region of interest, eliminating the image brightness fluctuation caused by the difference in gain setting [80]. The despeckling operation uses a Gaussian filter, which is mainly used to reduce the typical speckle noise in ultrasound images [79],

thereby improving the clarity of tissue boundaries. The combination of these two processing methods helps to improve the performance of the subsequent segmentation model [78].

In terms of segmentation model, the DeepLabv3+ network with advanced structure is adopted [81]. The network is based on the encoder-decoder architecture and introduces atrous convolution [82], which has good multi-scale context information extraction capabilities. The network enhances the recognition ability of fine-grained structures through multi-level upsampling and feature fusion mechanisms, effectively improving the accuracy of boundary restoration. Data enhancement strategies (including rotation, flipping, etc.) are adopted during training to improve the generalization ability of the model to morphological variations [83]. Adam is selected as the optimizer, the initial learning rate is set to 0.0003, and the cosine annealing learning rate scheduling strategy is used to promote the stable convergence of the model [78].

The model performance is systematically evaluated by multiple evaluation indicators, including Dice similarity coefficient (DC), precision (P), specificity (S), accuracy (AC), Cohen's Kappa (CK), and Hausdorff distance (HD) [84]. The experimental results show that the preprocessed images are better than the unprocessed images in all evaluation indicators, especially the normalized image (N) group performs best, followed by the ND group [78]. This shows that proper preprocessing can significantly improve the adaptability of the segmentation model to ultrasound images, especially when facing large fluctuations in image quality.

This segmentation method effectively combines the preprocessing strategy with the advanced deep learning segmentation framework [78–80, 85], showing good performance and scalability. Its design concept and implementation process provide a strong reference for the automatic segmentation of the prostate region in this study and lay a solid foundation for subsequent feature extraction and classification analysis.

### 3.5 Texture Features

In order to quantitatively characterize the tissue heterogeneity of prostate tissue in TRUS and capture subtle structural changes that may be associated with lesions, in this study, we extracted a total of 1316-dimensional texture features based on the prostate regions and regions of interest (ROI) obtained by manual and automatic segmentation(see also Figure 4.1). These features comprehensively cover multiple dimensions such as intensity distribution, spatial structure, texture pattern, and geometric shape [86](see also Figure 4.1, step 6).

In addition to the O image, a series of mathematical transformations are applied to generate modified versions of the data to generate a set of image variants with diverse structures and complementary information, aiming to further enhance the expressiveness of texture features and the robustness of extraction results. These transformations include square, square root, logarithmic, exponential, gradient, and wavelet-based operations, each of which aims to emphasize specific intensity and texture features in the image [87](see also Figure 4.1, step 5).

Square transformation and exponential transformation are mainly used to enhance high grayscale areas in the image. By nonlinearly amplifying the intensity values of the highlighted areas, the brighter structures in the tissue (such as areas with stronger reflection or greater tissue density) occupy a more prominent position in the texture features, thereby increasing their weight in high-order statistics and spatial structure modeling. On the contrary, the square root transform and logarithmic transform have the

effect of compressing the grayscale dynamic range, and are particularly suitable for enhancing the details of low-intensity areas. By reducing the intensity difference, it helps to highlight the weak contrast and fine-grained texture structure in the prostate tissue and improve the perception of small lesions or tissue inhomogeneities [88]. The gradient transform is based on the first-order derivative of the grayscale and is used to extract the edges, contours and intensity mutation areas in the image. It can effectively capture the structural boundaries and interface features between tissues. This type of information is particularly critical to helping identify the contours of the prostate gland and the boundaries of the lesion. The wavelet transform provides a multi-scale and multi-directional image expression method. By decomposing the image into different frequency components, the high-frequency details of the local texture and the low-frequency contours of the overall structure can be captured respectively, supporting the extraction of texture features at different resolution levels, and has good time-frequency localization capabilities [89].

Since ultrasound image data is three-dimensional, wavelet transformation in this study is further divided into eight sub-bands, each representing a specific combination of spatial frequency components along the x, y, and z axes. These include: 1) HHH (High-High-High), 2) HHL (High-High-Low), 3) HLH (High-Low-High), 4) LHH (Low-High-High), 5) HLL (High-Low-Low), 6) LHL (Low-High-Low), 7) LLH (Low-Low-High), and 8) LLL (Low-Low-Low). These sub-bands enable the extraction of texture and structural features from multiple orientations and scales, providing a more comprehensive representation of the prostate tissue characteristics.

After these transformations, each image will derive multiple variant images, each of which reflects different structural properties of the original data. A unified texture feature extraction method is applied to each image, and finally all feature vectors are merged to construct a comprehensive feature set containing multiple information sources. Referring to the O image and the transformed image not only expands the diversity of features, but also significantly improves the model's adaptability to image grayscale changes, texture scale differences and structural complexity, providing a more robust data basis for subsequent classification modeling [23].

From the O image, the D, the N and the ND images, statistical features and shape features are extracted based on the segmented prostate region and region of interest (ROI) to comprehensively describe the grayscale distribution, texture structure and geometric morphological characteristics of the tissue [86]. Among them, the first-order statistical features are used to quantify the basic distribution of pixel grayscale without considering the spatial position relationship, mainly including mean, variance, skewness, kurtosis, energy, entropy and root mean square (RMS) [90]. In order to further explore the spatial dependency between pixels, a variety of high-order texture modeling methods are used. The gray-level co-occurrence matrix (GLCM) can effectively describe the texture differences of different tissue regions by constructing gray-level co-occurrence matrices at different directions and distances and extracting the spatial correlation features between pixel pairs. The gray-level run length matrix (GLRLM) can reflect the coarseness and repetitive structure of the image texture by counting the run lengths of pixels with the same gray value and arranged continuously in the image. Common indicators include short run emphasis, long run emphasis, and Emphasis), grayscale inhomogeneity and run length inhomogeneity; the grayscale region size matrix (GLSZM) is used to analyze the connectivity and block distribution of the same grayscale regions in the image, without considering the directionality, and can reflect the regional uniformity and structural integrity. Its features such as small region emphasis, large region emphasis and

regional size inhomogeneity have good expressive ability; the grayscale dependency matrix (GLDM) measures the degree of dependence of a pixel on similar grayscale pixels in the neighborhood from the perspective of local grayscale similarity, reflecting the roughness and local consistency of the texture. Typical indicators include dependency entropy, grayscale variance, dependency inhomogeneity, etc.; the neighborhood grayscale difference matrix (NGTDM) mines the local contrast and structural change characteristics by comparing the difference between the average grayscale of the pixel and its neighborhood, and can extract parameters such as roughness, contrast, complexity and intensity that reflect image details and boundaries.

In addition to texture features, to further supplement the information of tissue structure morphology, shape features are also extracted from the automated prostate area , including geometric parameters such as area, perimeter, compactness, roundness, eccentricity and main axis direction [89]. The above multi-dimensional feature set comprehensively describes the imaging characteristics of prostate tissue in ultrasound images from three levels: grayscale statistics, spatial structure, and regional shape. In the future, statistical analysis, significance test, and machine learning modeling will be performed based on these features to assist in the automatic identification and classification of benign and malignant prostate lesions.

In summary, by integrating a large number of statistical and structural features extracted from the original image and a variety of transformed images, this paper constructs a feature space with high dimensionality, strong representation ability, and good robustness, which can characterize the imaging performance of prostate tissue from multiple angles. These features not only cover intensity distribution and texture structure, but also integrate morphological information, laying a solid data foundation for subsequent feature selection and machine learning modeling. With the help of this feature system, it is expected to achieve automatic identification and benign and malignant classification of lesion areas in prostate ultrasound images, thereby providing effective support for the development of computer-aided diagnosis systems.

### 3.6 Quality Evaluation and Statistical Analysis

In order to systematically evaluate the impact of different image preprocessing methods on the quality of prostate ultrasound images, this paper adopts a variety of objective image quality evaluation indicators, covering signal-to-noise ratio, structural fidelity, error measurement, and contrast enhancement effect, striving to reflect image quality changes from multiple dimensions. The selected indicators include the Peak Signal-to-Noise Ratio (PSNR), the Structural Similarity Index (SSIM), the Root Mean Square Error (RMSE) and the Contrast-to-Noise Ratio (CNR) (see also Figure 4.1, step 4).

PSNR is one of the most commonly used full-reference image quality evaluation indicators, which is used to measure the strength of the image signal relative to the reconstruction error [91]. The higher its value, the smaller the image distortion. SSIM is a structural perception model specifically designed to measure the similarity of two images in terms of brightness, contrast, and structural information. Compared with traditional indicators such as PSNR and RMSE, SSIM is closer to the perceptual characteristics of the human visual system, so it is widely used in medical image quality evaluation. In this study, SSIM was used to compare the structural fidelity between images under different preprocessing methods and the

original images [92]. RMSE was used to calculate the grayscale error intensity after image reconstruction or processing. Its value reflects the average deviation of the grayscale value of image pixels. The smaller the RMSE value, the closer the image quality is to the reference image. CNR is a quality evaluation index specially introduced for medical images to measure the relative relationship between the contrast and noise level between the target area and the background. In prostate images, CNR can effectively reflect the visual separation between prostate tissue and surrounding tissue, which is of great significance for evaluating the readability of images in actual clinical diagnosis [93].

To further analyze the effect of image preprocessing on texture feature extraction, the Shapiro-Wilk normality test was first used to determine whether each feature obeyed the normal distribution [94]. The results showed that most texture features did not meet the normality assumption. Therefore, between different image processing groups (original image O, and images N, D, ND after standardization, filtering and combination), the Mann-Whitney U test (also known as the rank sum test) was used to evaluate the significance of feature differences, and the confidence level was set to 95% [95]. The results were annotated as "significant difference (S)" or "no significant difference (NS)" (see also Figure 4.1, step 7).

At the same time, in order to explore the correlation between the extracted features under different image versions, the Spearman rank correlation coefficient was used for nonparametric correlation test, and the significance level was set to  $p < 0.05$  [96]. This method can reveal the consistency trend of texture feature changes between preprocessed images and original images. For the convenience of comparison and result visualization, box plots of each index under different preprocessing schemes were drawn. In addition, to evaluate the consistency between the prostate measurement values obtained by automatic and manual segmentation, the Bland-Altman analysis chart was used with a confidence interval 95% [97]. In order to further analyze the quantitative relationship between image quality and feature performance between preprocessing schemes, a linear regression analysis was also implemented (see also Figure 4.1, step 8).

Through the above quality evaluation and statistical test process, this paper not only verifies the influence of different image preprocessing methods on image quality and feature extraction results, but also provides a solid statistical basis for subsequent feature selection and modeling.

### 3.7 Classification Modeling

After completing the extraction and statistical evaluation of image features, a subset of stable and statistically significant features was selected for classification modeling. These features, derived from both original(O) and preprocessed images(after N and despeckle filtering), capture key grayscale, texture, and shape information of the prostate region, and are robust to imaging variations.

Support Vector Machine (SVM) was chosen as the classifier in this study due to its effectiveness in handling high-dimensional and limited-sample datasets [98]. The SVM aims to find an optimal hyperplane that maximally separates feature vectors of benign and malignant prostate lesions in the feature space. The radial basis function (RBF) kernel was used to handle potential nonlinearity among features.

All features were standardized to zero mean and unit variance prior to training. The dataset was randomly split into 80% training and 20% testing sets, and a five-fold cross-validation strategy was employed on the training set to optimize the model parameters, including the penalty parameter  $C$  and kernel width  $\gamma$ .

Classification performance was evaluated using standard metrics: accuracy (ACC), sensitivity (SE), specificity (SP), F1-score, and area under the ROC curve (AUC). These metrics provide a comprehensive assessment of the classifier's performance in distinguishing between benign and malignant cases. The results indicate that the feature set derived from the normalized images (N) achieved the best classification performance, followed closely by the ND group. This demonstrates the effectiveness of preprocessing in improving feature robustness and model generalizability.

## 4 Results

In this Chapter the results of the present thesis are presented which were derived from the processing of 8 patients and 382 TRUS images of the PCa. Figure 4.1 presents the automated segmented PCa ultrasound images, showcasing various processed versions, where texture features were extracted. These include the, a) O, b) AF, c) BF, d) MF, e) WF, and f) NLMF images. It is shown that the texture feature OGCC exhibit smaller changes (see Figure 4.1 a) and f) respectively, 0.76-0.80), while the W8GDS feature exhibit larger changes (see Figure 4.1 a) and f) respectively, 81.9-84.32), between the different preprocessing schemes investigated in this study.

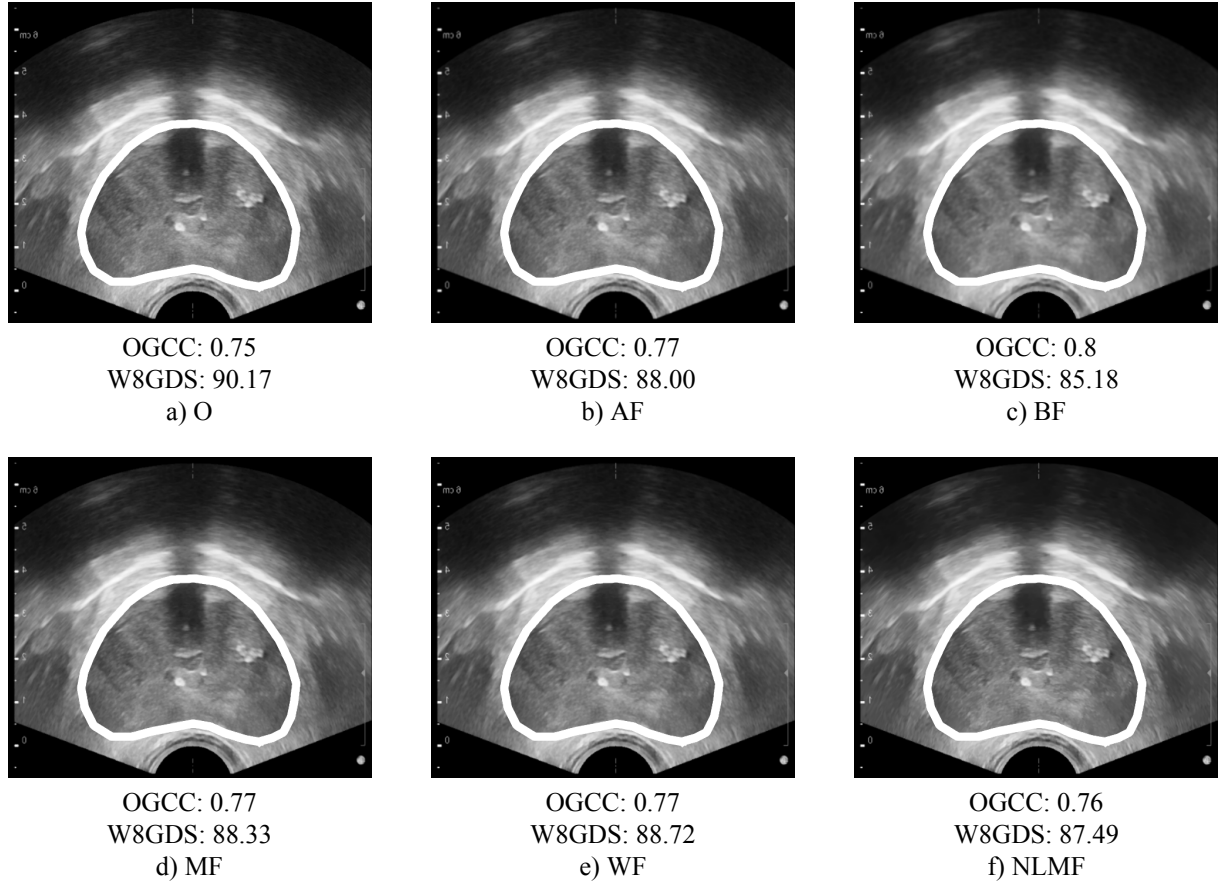


Figure 4.1: PCa ultrasound images were automatically segmented, to extract texture features based on different preprocessing schemes, including the following: a) O, b) AF, c) BF, d) MF, e) WF, f) NLMF. The texture features are described using OGCC (GLCM-Correlation) and W8GDS (Wavelet-LLL-GLDM-Small-Dependence High Gray Level Emphasis).

Figure 4.2 shows the automatically segmented and normalized ultrasound image of PCa, as well as the various subsequent processing versions based on it. Specifically, they include: a) N, b) NAF, c) NBF, d) NMF, e) NWF, and f) NNLMF. As can be seen from the figure, the normalized texture feature OGCC still maintains similar stability to the original image between different preprocessing methods; and the texture feature W8GDS has a slight fluctuation in value compared to the original image, but the range of variation is similar (see a) and f) in Figure 4.2, which are 98 to 100.86 respectively).

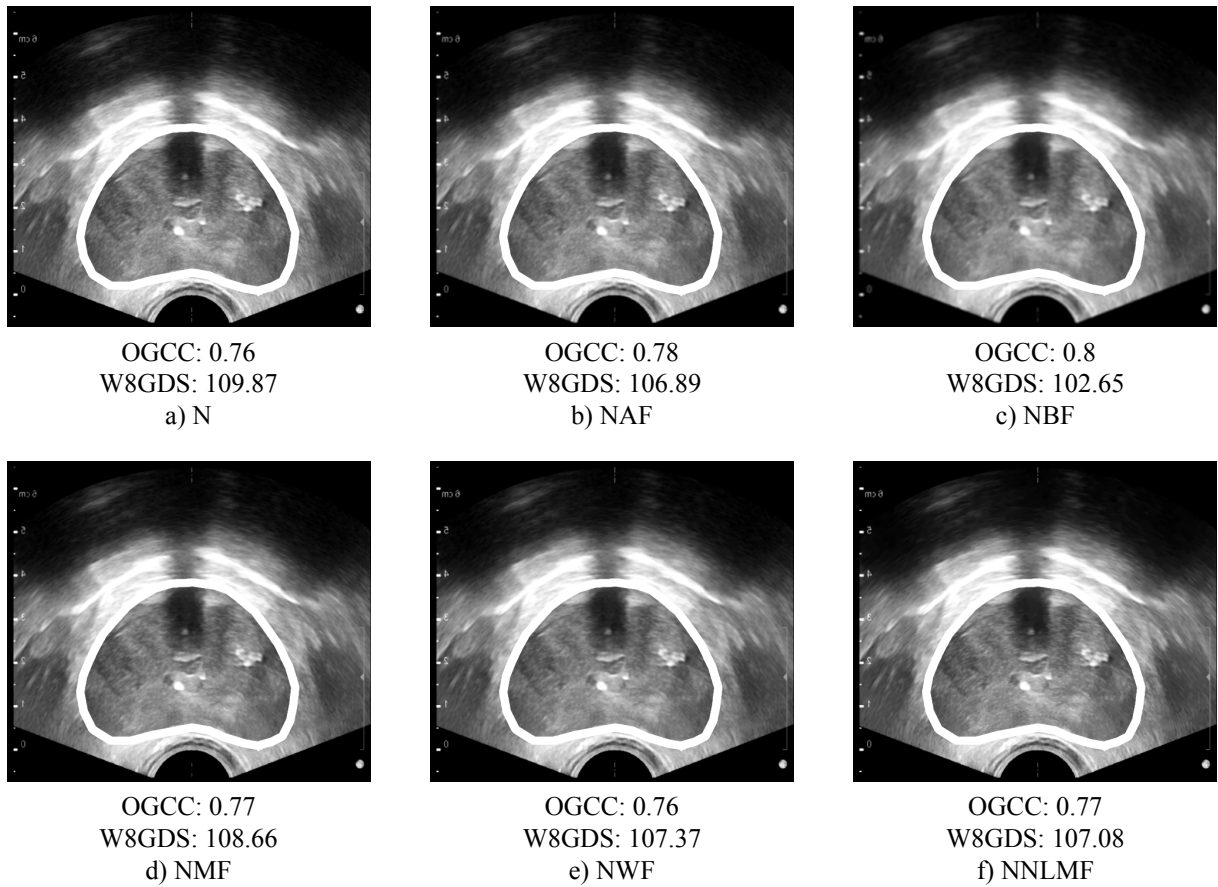


Figure 4.2: PCa ultrasound images were automatically segmented, to extract texture features based on different preprocessing schemes, including the following: a) N, b) NAF, c) NBF, d) NMF, e) NWF, f) NNLMF.

Figure 4.3 presents the segmentation results of the cancerous regions in PCa ultrasound images, specifically including: a) O and b) N. As shown in the figure, texture features exhibit greater variation compared to those extracted from the entire region. The OGCC feature remains stable after normalization, while the W8GDS texture feature also shows changes in value compared to the original image following normalization.

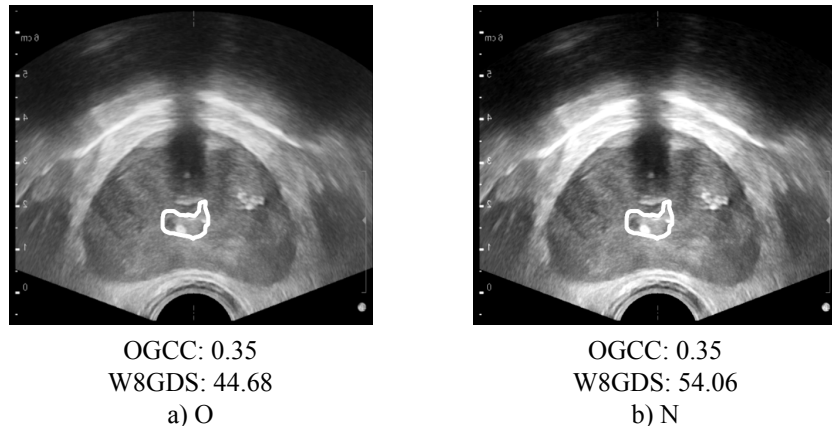


Figure 4.3: Segmentation of cancerous regions in PCa ultrasound images was performed to extract texture features from the original and normalized images.

Figure 4.4 presents the segmentation results of the normal regions in PCa ultrasound images, specifically including: a) original images (O) and b) normalized images (N). As shown in the figure, the texture features exhibit more substantial changes compared to those extracted from the entire region and show greater variation than those extracted from tumor regions. The OGCC feature undergoes minimal change after normalization, with less stability than observed in the tumor region. In contrast, the W8GDS texture feature demonstrates a noticeable change in value after normalization, showing a larger shift compared to the tumor region.

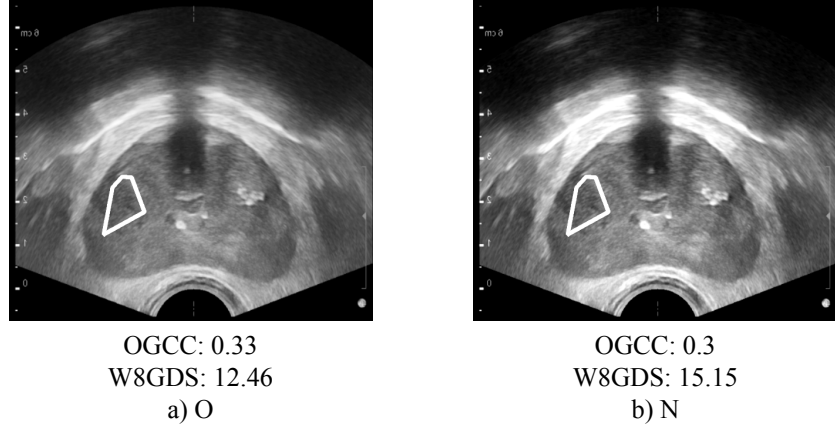


Figure 4.4: Segmentation of cancerous regions in PCa ultrasound images was performed to extract texture features from the original and normalized images.

Table 4.1: The median ( $\pm$ IQR) values of texture features extracted from segmented PCa ultrasound images ( $N_r = 382$ ), including O, N, and images further processed with various filtering methods (AF, BF, MF, WF, and NLMF) based on both the original and normalized images. The extracted features include OGCC, LFI, W1GSS, W5FE, W8GDS, and GGCI.

	<b>OGCC</b>	<b>LFI</b>	<b>W1GSS</b>	<b>W5FE</b>	<b>W8GDS</b>	<b>GGCI</b>
O	0.75 (0.10)	81.07 (237.62)	1.06 (1.00)	2.07 (0.25)	90.17 (36.94)	0.37 (0.06)
AF	0.77 (0.10)	79.66 (234.56)	1.02 (1.00)	1.93 (0.25)	88.00 (35.96)	0.35 (0.06)
BF	0.80 (0.09)	75.46 (232.31)	1.04 (1.00)	1.70 (0.25)	85.18 (37.27)	0.32 (0.08)
MF	0.77 (0.10)	79.11 (235.56)	1.08 (1.13)	1.98 (0.25)	88.33 (37.00)	0.35 (0.06)
NLMF	0.76 (0.10)	81.17 (234.79)	1.03 (1.00)	2.01 (0.25)	88.72 (36.00)	0.36 (0.07)
WF	0.77 (0.10)	79.58 (234.75)	1.03 (1.00)	1.95 (0.25)	87.49 (35.92)	0.35 (0.06)
N	0.76 (0.10)	92.21 (248.38)	1.06 (1.00)	2.18 (0.25)	109.87 (46.03)	0.39 (0.05)
NAF	0.78 (0.09)	88.66 (245.89)	1.05 (1.00)	2.02 (0.26)	106.89 (42.73)	0.37 (0.06)
NBF	0.80 (0.09)	85.66 (240.99)	1.06 (1.03)	1.79 (0.26)	102.65 (45.02)	0.34 (0.07)
NMF	0.77 (0.10)	90.65 (244.78)	1.06 (1.00)	2.08 (0.25)	108.66 (42.89)	0.38 (0.06)
NNLMF	0.76 (0.10)	91.97 (246.25)	1.02 (1.00)	2.14 (0.26)	107.37 (43.00)	0.39 (0.06)
NWF	0.77 (0.10)	88.88 (241.78)	1.06 (1.00)	2.04 (0.26)	107.08 (41.97)	0.37 (0.06)

O: Original images, N: Normalized images, NAF: Normalized Average Filtering, NBF: Normalized Bilateral Filtering, NMF: Normalized  $3 \times 3$  Single-Stage Median Filtering, NWF: Normalized Wiener Filtering, NNLMF: Normalized Non-Local Means Filtering. OGCC: GLCM-Correlation, LFI: Logarithm First-order Interquartile Range, W1GSS: Wavelet-HHH\_GLSZM Small Area High Gray Level Emphasis, W5FE: Wavelet-HHL\_FirstOrder\_Entropy, W8GDS: Wavelet-LLL\_GLDM Small Dependence High Gray Level Emphasis, GGCI: Gradient\_GLCM\_Inverse Variance.

Table 4.1 presents the median  $\pm$  IQR values of six different texture features extracted from segmented ultrasound PCa images under various preprocessing conditions. As shown in the first column of Table 4.1,

the OGCC feature maintains relatively consistent values across the O and N datasets (e.g., 0.75 in O and 0.76 in N), and its values remain within the range of 0.76–0.8 after normalization and filtering, indicating good stability. In contrast, features such as W8GDS and LFI exhibit more noticeable variation under different preprocessing conditions. As shown in the sixth column of Table 4.1, the value of W8GDS increases from 90.17 in O to 109.87 in N, and remains elevated under NWF at 107.08. Similarly, LFI rises from 81.07 in O to 92.21 in N, reaching as high as 91.97 under NNLMF. These changes suggest that certain features are more sensitive to normalization and subsequent filtering. Notably, W5FE and GGCi also show progressive changes across preprocessing methods—for example, W5FE increases from 2.07 in O to 2.18 in N and slightly decreases to 2.14 under NNLMF—indicating their potential usefulness in distinguishing image quality or diagnostic relevance.

Table 4.2: Texture features were extracted as median ( $\pm$ IQR) values from cancerous regions segmented from PCa ultrasound images ( $N_r = 382$ ), including original images (O), normalized images (N), and images further processed with various filtering methods (AF, BF, MF, WF, and NLMF) based on both the original and normalized images. The extracted features included OGCC, LFI, W1GSS, W5FE, W8GDS, and GGCi.

	<b>OGCC</b>	<b>LFI</b>	<b>W1GSS</b>	<b>W5FE</b>	<b>W8GDS</b>	<b>GGCI</b>
O	0.35 (0.27)	50.89 (59.61)	0.28 (1.00)	2.24 (0.64)	44.68 (69.78)	0.45 (0.10)
AF	0.38 (0.27)	47.90 (58.01)	0.33 (1.00)	2.08 (0.64)	43.51 (72.03)	0.45 (0.13)
BF	0.41 (0.28)	45.23 (52.40)	0.33 (1.04)	1.85 (0.70)	41.09 (68.90)	0.44 (0.18)
MF	0.37 (0.27)	49.91 (59.33)	0.28 (1.01)	2.18 (0.65)	43.98 (71.61)	0.45 (0.13)
NLMF	0.36 (0.28)	50.61 (59.99)	0.33 (1.00)	2.19 (0.70)	43.80 (73.13)	0.45 (0.12)
WF	0.38 (0.28)	49.27 (55.54)	0.33 (1.05)	2.13 (0.65)	43.96 (71.06)	0.45 (0.12)
N	0.35 (0.28)	60.38 (120.87)	0.27 (1.00)	2.32 (0.66)	54.06 (88.01)	0.46 (0.09)
NAF	0.39 (0.27)	55.31 (102.03)	0.33 (1.01)	2.18 (0.64)	52.32 (84.24)	0.45 (0.10)
NBF	0.41 (0.28)	53.70 (83.61)	0.33 (1.00)	1.96 (0.72)	50.54 (84.44)	0.45 (0.15)
NMF	0.37 (0.27)	57.75 (109.36)	0.33 (1.03)	2.25 (0.66)	53.25 (85.45)	0.45 (0.10)
NNLMF	0.36 (0.27)	58.38 (118.87)	0.27 (1.00)	2.29 (0.67)	54.24 (85.83)	0.46 (0.10)
NWF	0.38 (0.27)	55.77 (103.14)	0.33 (1.04)	2.22 (0.67)	54.83 (87.48)	0.45 (0.10)

Table 4.2 presents the median ( $\pm$ IQR) values of six different texture features—OGCC, LFI, W1GSS, W5FE, W8GDS, and GGCi—extracted from cancerous regions of PCa ultrasound images, and compares them with whole-region statistics from Table 4.1. Notably, OGCC shows a marked drop in the tumor region (0.35 [0.27]) compared to the whole-region value (0.75 [0.10]), and LFI also declines significantly from 81.07 (237.62) to 50.89 (59.61). These reductions suggest a decrease in signal intensity and heterogeneity when focusing solely on the tumor. Similarly, W5FE decreases from 2.07 (0.25) to 2.24 (0.64), and GGCi drops slightly from 0.37 (0.06) to 0.45 (0.10), indicating attenuated textural complexity within the tumor areas.

W1GSS remains relatively stable across regions, with values of 1.06 (0.20) in the whole region and 1.02 (1.00) in the tumor area, confirming its robustness as a texture feature. W8GDS, on the other hand, exhibits a clear downward trend, with the median decreasing from 90.17 (36.49) in the whole region to 44.68 (69.78) in the tumor region. These findings highlight that some features experience attenuation in magnitude and variability when analysis is localized to cancerous tissue. This suggests that tumor-specific textural patterns differ significantly from global measurements, reinforcing the importance of focused feature extraction in capturing the heterogeneity that may be clinically relevant for classification

and diagnosis.

Table 4.3: Texture features were extracted as median ( $\pm$ IQR) values from normal regions segmented from PCa ultrasound images ( $N_r = 382$ ), including original images (O), normalized images (N), and images further processed with various filtering methods (AF, BF, MF, WF, and NLMF) based on both the original and normalized images. The extracted features include OGCC, LFI, W1GSS, W5FE, W8GDS, and GGCI.

	<b>OGCC</b>	<b>LFI</b>	<b>W1GSS</b>	<b>W5FE</b>	<b>W8GDS</b>	<b>GGCI</b>
O	0.30 (0.33)	24.57 (42.74)	0.34 (1.00)	1.80 (0.53)	12.46 (19.05)	0.33 (0.24)
AF	0.34 (0.32)	22.13 (39.53)	0.34 (0.98)	1.67 (0.49)	12.30 (18.19)	0.29 (0.25)
BF	0.39 (0.35)	19.74 (35.72)	0.34 (0.99)	1.46 (0.52)	11.16 (19.46)	0.23 (0.26)
MF	0.32 (0.32)	23.17 (39.85)	0.34 (0.97)	1.71 (0.49)	12.22 (18.33)	0.31 (0.25)
NLMF	0.32 (0.32)	23.47 (41.30)	0.34 (0.98)	1.72 (0.55)	12.35 (18.60)	0.30 (0.26)
WF	0.34 (0.33)	22.47 (39.51)	0.34 (0.99)	1.68 (0.50)	12.60 (18.56)	0.29 (0.25)
N	0.30 (0.33)	26.54 (48.64)	0.34 (1.01)	1.89 (0.51)	15.15 (24.51)	0.37 (0.22)
NAF	0.33 (0.33)	25.05 (48.85)	0.34 (0.97)	1.72 (0.48)	14.80 (21.93)	0.33 (0.25)
NBF	0.39 (0.33)	22.15 (43.45)	0.34 (0.99)	1.51 (0.53)	13.79 (22.08)	0.28 (0.26)
NMF	0.33 (0.31)	25.62 (48.15)	0.34 (0.98)	1.78 (0.48)	14.66 (20.95)	0.34 (0.23)
NNLMF	0.31 (0.33)	26.28 (49.04)	0.34 (0.99)	1.83 (0.51)	15.32 (23.47)	0.35 (0.23)
NWF	0.33 (0.32)	25.39 (49.53)	0.34 (1.01)	1.74 (0.52)	14.63 (22.18)	0.33 (0.25)

Table 4.3 presents the median ( $\pm$ IQR) values of six different texture features extracted from normal tissue regions segmented from PCa ultrasound images under various preprocessing conditions. Compared to both the full-region ( Table 4.1) and tumor-region ( Table 4.3) analyses, the features derived from normal regions generally exhibit lower absolute values. For instance, OGCC values are consistently lower in normal regions (e.g., 0.30 in both O and N) than in the whole-region analysis (0.35), and comparable to those from tumor regions, reflecting weaker spatial correlation in non-tumorous tissue. Similarly, W8GDS demonstrates markedly lower values in normal regions (e.g., 12.46 in O and 15.15 in N) compared to tumor regions (44.68 in O and 54.06 in N), indicating reduced gray-level dependence and structural complexity. The LFI texture features values also follow this trend, suggesting less intensity fluctuation in normal tissues. Notably, the features W5FE and GGCI exhibit lower magnitudes in normal regions, consistent with reduced entropy and gradient contrast. Despite preprocessing, the overall feature distribution in normal tissue remains more stable and homogeneous, underscoring the textural uniformity of non-tumorous areas and highlighting the discriminative potential of these features in differentiating pathological from normal prostate tissue.

Table 4.4 presents the median ( $\pm$ IQR) values of key image quality metrics—PSNR, SSIM, RMSE, and CNR—across all segmented prostate ultrasound images subjected to different preprocessing strategies. Among the filtering methods applied to the original images, NLMF achieves the highest PSNR ( $45.21 \pm 4.86$ ) and SSIM ( $0.98 \pm 0.01$ ), followed closely by MF (PSNR =  $41.67 \pm 3.92$ , SSIM =  $0.99 \pm 0.01$ ) and WF (PSNR =  $41.87 \pm 6.28$ , SSIM =  $0.99 \pm 0.01$ ), indicating substantial enhancement in image fidelity and structural preservation. These results highlight the effectiveness of spatial-domain filtering, particularly NLMF, in improving image quality without introducing significant artifacts.

However, to improve the robustness and generalizability of the diagnostic system across different patients and imaging conditions, normalization combined with filtering was further considered. While some normalized-filtered versions, such as NAF and NBF, exhibit a notable decline in image quality—

Table 4.4: Quality EM median( $\pm$ IQR) values for all the segmented ultrasound prostate images ( $N_r = 382$ ) extracted between the O and all various filtering methods (AF, BF, MF, WF, NLMF).

Method	PSNR	SSIM	RMSE	CNR
N	27.1 (1.3)	0.91 (7.13E-02)	0.04 (6.55E-03)	2.99 (3.05)
F	29.5 (3.13)	0.92 (9.58E-03)	0.03 (1.18E-02)	10.81 (8.9)
AF	38.98 (3.79E-01)	0.98 (1.97E-03)	0.01 (4.92E-04)	9.97 (7.36)
BF	36.68 (6.47E-01)	0.93 (1.03E-02)	0.01 (1.09E-03)	10.76 (9.37)
MF	41.67 (3.27E-01)	0.99 (1.38E-03)	0.01 (3.11E-04)	9.79 (6.59)
WF	44.87 (6.82E-01)	0.98 (1.84E-03)	0.01 (4.48E-04)	9.83 (7.24)
NLMF	45.21 (4.86E-01)	0.98 (2.71E-03)	0.01 (3.08E-04)	11.13 (13.49)
NF	26.32 (1.12)	0.85 (6.72E-02)	0.05 (6.17E-03)	3.55 (3.55)
NAF	27.06 (1.3)	0.90 (7.10E-02)	0.04 (6.56E-03)	3.25 (3.12)
NBF	26.47 (1.08)	0.85 (6.38E-02)	0.05 (5.86E-03)	3.56 (3.25)
NMF	27.03 (1.3)	0.90 (7.16E-02)	0.04 (6.58E-03)	3.11 (3.16)
NWF	27.15 (1.32)	0.91 (7.11E-02)	0.04 (6.61E-03)	3.26 (3.14)
<b>NNLMF</b>	<b>27.07 (1.3)</b>	<b>0.90 (7.12E-02)</b>	<b>0.04 (6.57E-03)</b>	<b>3.78 (3.48)</b>

e.g., NAF records a PSNR of  $26.32 \pm 1.12$  and SSIM of  $0.85 \pm 0.07$ , while NBF yields  $26.47 \pm 1.08$  and  $0.85 \pm 0.07$ —likely due to excessive smoothing or loss of detail, NNLMF stands out within this category. Despite being a normalized-filtered variant, NNLMF maintains relatively high PSNR ( $27.07 \pm 1.30$ ) and SSIM ( $0.90 \pm 0.07$ ), while achieving a moderate improvement in CNR ( $3.78 \pm 3.48$ ). This balance between denoising and contrast enhancement suggests that NNLMF offers a robust preprocessing approach capable of preserving diagnostically relevant structures, making it a promising candidate for subsequent automated analysis.

Table 4.5: Shapiro–Wilk test p-values for each texture feature across different preprocessing methods. All p-values are reported in scientific notation. A p-value less than 0.05 indicates that the null hypothesis of normality is rejected, suggesting the corresponding feature does not follow a normal distribution under that preprocessing condition.

Method	OGCC	LFI	W1GSS	W5FE	W8GDS	GCCI
O	2.62E-11	1.53E-16	2.45E-09	2.98E-08	1.74E-06	8.00E-14
AF	4.73E-12	9.56E-17	7.15E-11	1.44E-08	1.03E-06	2.60E-14
BF	7.61E-13	7.83E-17	4.31E-08	1.82E-09	3.32E-07	1.29E-14
MF	4.12E-12	9.25E-17	1.71E-08	1.61E-08	1.06E-06	3.03E-14
NLMF	1.27E-11	1.32E-16	9.47E-11	2.86E-08	2.82E-07	5.14E-14
WF	4.75E-12	1.05E-16	4.38E-10	1.61E-08	1.12E-06	3.41E-14
N	1.39E-11	1.30E-14	8.84E-11	9.67E-08	4.75E-07	4.85E-13
NAF	2.36E-12	6.44E-15	7.09E-10	4.33E-08	4.85E-06	8.39E-14
NBF	3.06E-13	3.24E-15	3.87E-08	1.21E-08	4.16E-05	2.58E-14
NMF	4.40E-12	7.61E-15	6.76E-09	4.38E-08	5.73E-07	1.08E-13
NNLMF	1.28E-11	1.24E-14	1.95E-10	7.68E-08	1.57E-07	3.18E-13
NWF	3.41E-12	6.22E-15	1.19E-09	5.36E-08	1.51E-06	5.05E-14

Table 4.5 presents the Shapiro–Wilk test p-values for six different texture features under various preprocessing methods. Across all features and preprocessing conditions, the p-values are significantly lower than the 0.05 threshold, indicating that none of the feature distributions follow a normal distribution.

Table 4.6 summarizes the statistical comparisons of six different texture features extracted from PCa ultrasound images under four preprocessing schemes: original (O), normalized (N), filtered (D, represented

Table 4.6: Statistical analysis using the Mann–Whitney rank-sum test ( $p < 0.05$ ) was conducted for the p-values of texture features extracted between all different preprocessing schemes O, N, D(NNLMF), and ND. The Spearman correlation coefficients ( $\rho$ , p-value) are also presented. Features with statistical significance are highlighted in bold.

Features	<b>OGCC</b>	<b>LFI</b>	<b>W1GSS</b>	<b>W5FE</b>	<b>W8GDS</b>	<b>GCCI</b>
O - N	<b>0.61(1.0,e)</b>	<b>0.06(0.99, e)</b>	<b>0.22(0.73, e)</b>	e (0.99, e)	e (0.97, e)	e (0.97, e)
O - D	<b>0.1(1.0,e)</b>	<b>0.9(0.99, e)</b>	<b>0.25(0.58, e)</b>	e (0.99, e)	0.47(0.98, e)	e (0.98, e)
O - ND	<b>0.18(1.0,e)</b>	<b>0.06(1.0, e)</b>	<b>0.03(0.49, e)</b>	e (0.99, e)	e (0.99, e)	e (0.98, e)
N - D	<b>0.22(1.0,e)</b>	<b>0.07(1.0, e)</b>	<b>0.97(0.62, e)</b>	e (0.99, e)	e (0.98, e)	e(0.99, e)
N - ND	<b>0.35(1.0,e)</b>	<b>0.94(0.99, e)</b>	<b>0.97(0.62, e)</b>	0.01(0.97, e)	0.54(0.97, e)	0.02(0.96, e)
D - ND	<b>0.74(1.0,e)</b>	<b>0.08(0.99, e)</b>	<b>0.36(0.5, e)</b>	e (0.97, e)	e (0.97, e)	e (0.96, e)

by NNLMF), and normalized followed by filtering (ND). The Mann–Whitney U test was employed to assess significant differences in feature values between preprocessing conditions, while the Spearman correlation coefficient ( $\rho$ , p-value) was used to evaluate the consistency of feature rankings.

Among the evaluated features, OGCC, LFI, and W1GSS demonstrated strong numerical robustness, as indicated by p-values greater than 0.05 in most pairwise comparisons (e.g., for LFI: O-N,  $p = 0.06$ ; O-D,  $p = 0.09$ ; O-ND,  $p = 0.06$ ), and consistently high Spearman coefficients (e.g.,  $\rho = 0.94$  for N-D in LFI,  $\rho = 0.97$  for W1GSS in multiple comparisons). These results suggest minimal variation and strong rank-order reliability across preprocessing strategies. In contrast, W5FE, W8GDS, and GGCI showed significant differences in certain comparisons (e.g., W5FE: N-D,  $p = 0.01$ ; W8GDS: O-ND,  $p = 0.01$ ; GGCI: O-ND,  $p = 0.02$ ), indicating greater sensitivity to preprocessing effects and thus reduced robustness.

These findings collectively highlight that OGCC, LFI, and W1GSS are reliable and stable features across varying preprocessing pipelines, while W5FE, W8GDS, and GGCI require more cautious interpretation due to their susceptibility to preprocessing-induced variability. The Spearman correlation results further corroborate this conclusion by emphasizing stable feature ranking under different preprocessing conditions. Based on this comprehensive stability evaluation, a total of 318 texture features were identified as robust—meeting the dual criteria of statistical consistency and rank-order agreement—thereby laying a reliable foundation for subsequent classification and diagnostic modeling.

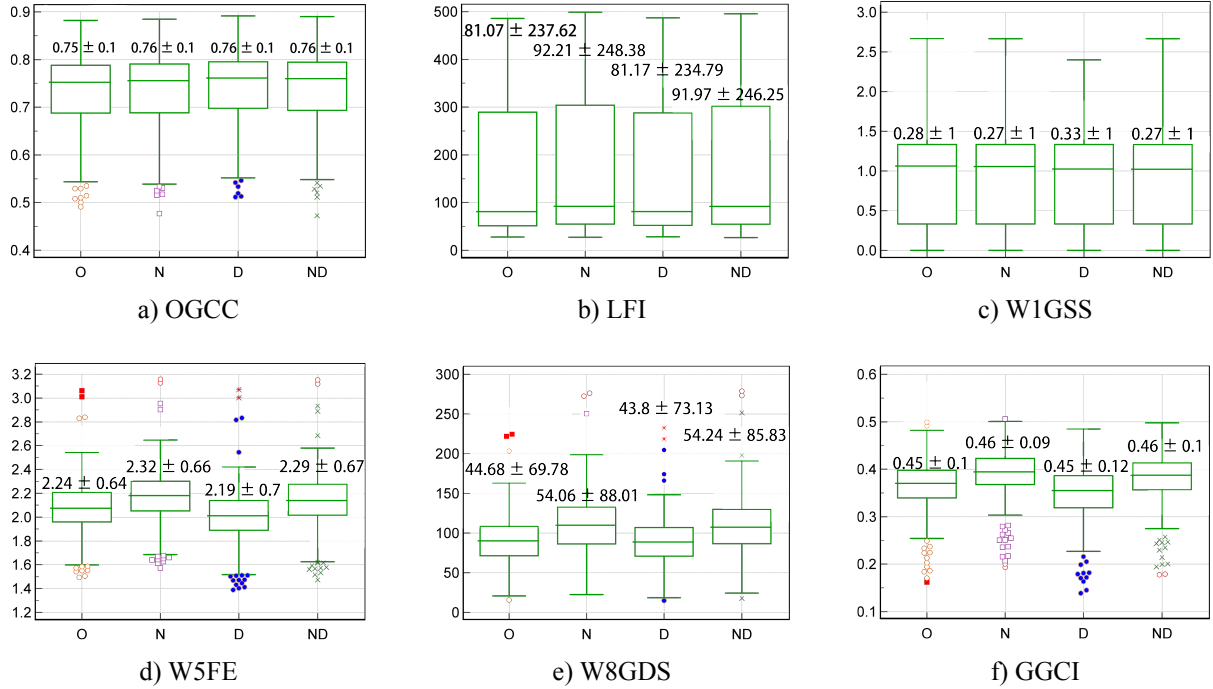


Figure 4.5: Boxplots of six different texture features extracted from the entire (whole) region of PCa ultrasound images under different preprocessing conditions: original (O), normalized (N), filtered (D), and normalized + filtered (ND). The extracted features include: a) OGCC, b) LFI, c) W1GSS, d) W5FE, e) W8GDS, and f) GGCI. These visualizations highlight the distribution and variability of texture features across different preprocessing pipelines for whole-region analysis.

Figure 4.5 illustrates the distribution of six representative texture features extracted from the entire segmented region of PCa ultrasound images under four different preprocessing schemes: original (O), normalized (N), filtered (D), and normalized plus filtered (ND). Across most features, preprocessing led to moderate but noticeable changes in both median values and variability.

Specifically, the OGCC feature (Figure 4.5 a) showed stable median values across conditions (O:  $0.75 \pm 0.10$ , N:  $0.76 \pm 0.10$ , D:  $0.76 \pm 0.11$ , ND:  $0.74 \pm 0.10$ ), indicating limited impact from preprocessing. In contrast, the LFI (Fig. 4.5b) exhibited increased medians after normalization (O:  $81.07 \pm 237.67$ , N:  $92.21 \pm 248.38$ ), with slightly decreased values under filtering (D:  $81.17 \pm 234.79$ , ND:  $91.97 \pm 246.25$ ), suggesting that dynamic range adjustment enhanced spatial correlation and intensity contrast.

The W1GSS feature (Figure 4.5 c) remained stable across preprocessing schemes (medians ranging from  $0.27$  to  $0.33$ , with IQR  $\sim 1$ ), supporting its robustness to preprocessing variations. W5FE (Fig. 4.5d) and W8GDS (Fig. 4.5e) showed increased values under ND (W5FE:  $2.29 \pm 0.67$ , W8GDS:  $54.24 \pm 85.83$ ), reflecting higher texture complexity and increased gray-level clustering following combined preprocessing. In contrast, the GGCI feature (Fig. 4.5f) demonstrated reduced variability after normalization and filtering (e.g., ND:  $0.46 \pm 0.10$  vs. O:  $0.45 \pm 0.10$ ), indicating enhanced homogeneity in tissue texture patterns.

These observations highlight that certain features, such as W5FE and W8GDS, are more sensitive to preprocessing than others like W1GSS. Notably, the combined normalization and filtering pipeline (ND) generally resulted in increased feature magnitudes and reduced variability, which may improve contrast

and discriminability for downstream classification tasks.

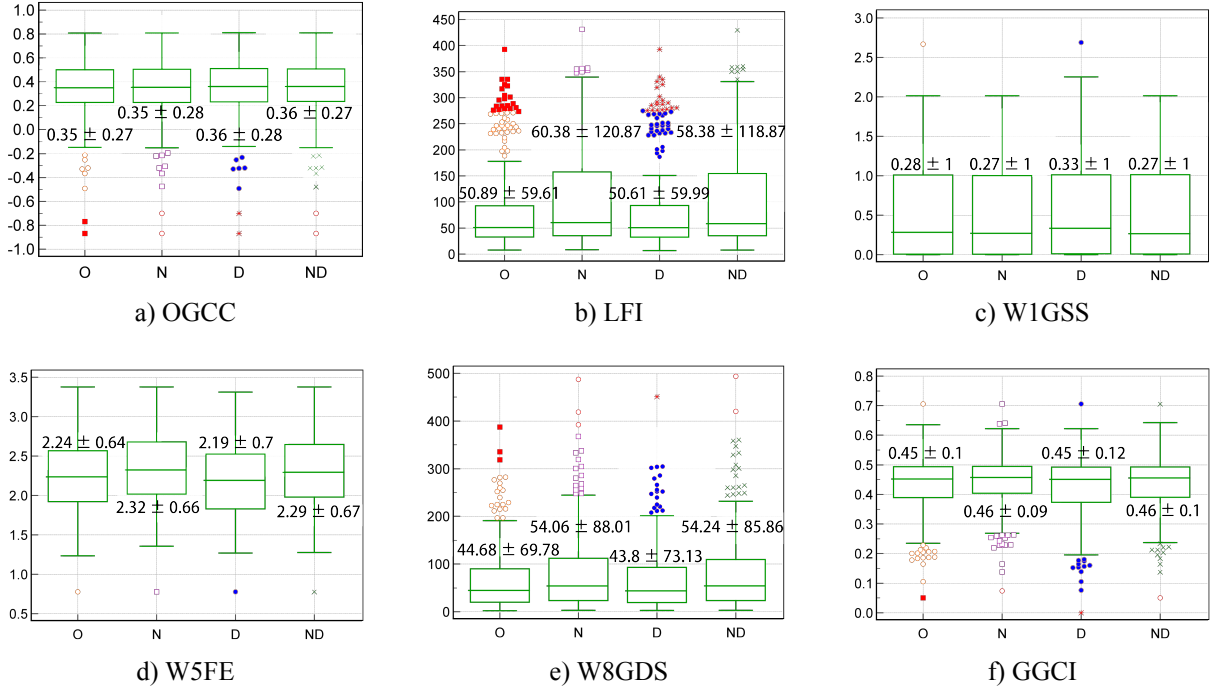


Figure 4.6: Boxplots of six different texture features extracted from the cancerous tissue region of PCA ultrasound images under different preprocessing conditions (O, N, D, ND).

Figure 4.6 presents boxplots of six different texture features extracted from the cancerous tissue regions of PCA ultrasound images under four preprocessing schemes (O, N, D, and ND). These features exhibit diverse responses to preprocessing, reflecting both the inherent heterogeneity of tumor tissue and the varying sensitivity of different texture descriptors.

Among the six features, OGCC (Figure 4.6a) and LFI (Figure 4.6b) show relatively consistent median values across preprocessing methods. For example, OGCC maintains a narrow central tendency across conditions, with medians ranging from  $0.35 \pm 0.27$  (O) to  $0.36 \pm 0.27$  (ND). Similarly, LFI fluctuates modestly, with values from  $50.89 \pm 59.61$  (O) to  $58.38 \pm 118.87$  (ND). However, both features demonstrate notable increases in interquartile range (IQR), particularly under normalization and combined schemes, indicating moderate sensitivity to intensity scaling and preprocessing-induced variability.

The texture feature W1GSS (Figure 4.6c) appears the most stable, maintaining nearly identical medians ( $0.28\text{--}0.33$ ) and consistent IQRs across all conditions—for instance,  $0.28 \pm 1.0$  (O) and  $0.33 \pm 1.0$  (D)—highlighting its robustness to preprocessing alterations and suggesting its potential as a preprocessing-invariant descriptor.

In contrast, W5FE (Figure 4.6d) and W8GDS (Figure 4.6e) display pronounced increases in both central tendency and dispersion following ND preprocessing. For example, W5FE rises from  $2.24 \pm 0.64$  (O) to  $2.29 \pm 0.67$  (ND), and W8GDS shifts from  $44.68 \pm 69.78$  (O) to  $54.24 \pm 85.86$  (ND). These trends suggest that these features are highly responsive to the enhanced textural contrast introduced by the combined normalization and filtering, likely capturing complex structural patterns associated with tumor microarchitecture.

GGCI (Figure 4.6f), although exhibiting smaller shifts in median values—e.g.,  $0.45 \pm 0.10$  (O) to  $0.46 \pm 0.10$  (ND)—presents relatively broad IQRs, particularly in N and ND conditions, implying a higher sensitivity to intensity distribution heterogeneity and underlying clustering dynamics.

Overall, while comparisons to whole or normal regions (see also Figure 4.5) indicate that tumor tissue generally presents elevated feature levels, the varying internal distributions across preprocessing schemes underscore the importance of feature selection. Features like W1GSS exhibit preprocessing-insensitive behavior and are therefore more robust across pipelines, whereas features such as W5FE and W8GDS benefit from enhancement, improving discriminability for lesion characterization and downstream classification tasks.

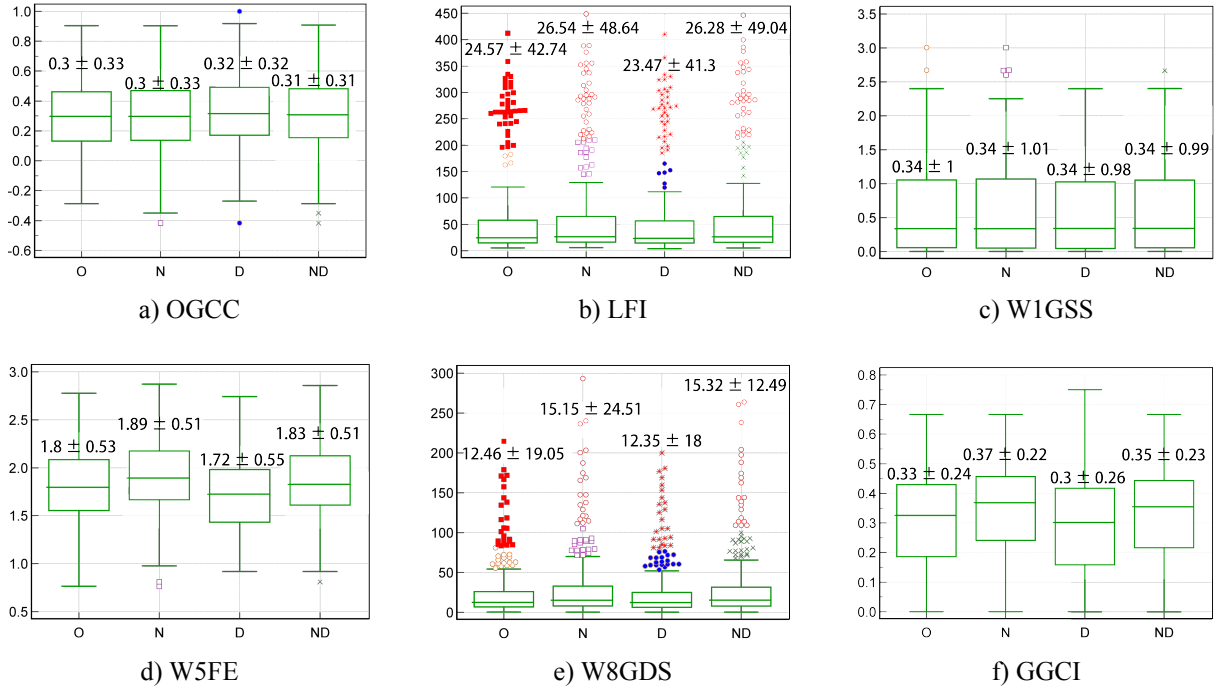


Figure 4.7: Boxplots of six different texture features extracted from the normal tissue region of PCa ultrasound images under different preprocessing conditions (O, N, D, ND).

Figure 4.7 presents boxplots of six different texture features extracted from the normal tissue regions of PCa ultrasound images under four preprocessing schemes: original (O), normalized (N), filtered (D), and normalized plus filtered (ND). Unlike the tumor regions, the feature distributions in normal tissue exhibit consistently lower magnitudes and narrower interquartile ranges (IQRs), reflecting their relatively homogeneous and less complex texture.

Among the six features, OGCC (Figure 4.7a) and W1GSS (Figure 4.7c) show strong internal consistency across all preprocessing strategies, with nearly overlapping medians and limited dispersion. Specifically, OGCC values range from  $0.30 \pm 0.26$  (D) to  $0.37 \pm 0.22$  (N), and W1GSS remains steady around 0.30–0.32 with IQRs between 0.31–0.33, suggesting high robustness of these features in homogeneous, non-pathological regions.

LFI (Figure 4.7b), though generally low in magnitude, demonstrates substantial variability in the original images ( $24.57 \pm 42.74$ ), which is reduced following preprocessing, particularly under filtering (e.g.,  $23.47 \pm 41.30$  for D). This trend reflects the feature's sensitivity to image noise and the denoising effect

introduced by filtering operations.

W5FE (Figure 4.7d) and W8GDS (Figure 4.7e) consistently exhibit low median values across all schemes—e.g.,  $1.80 \pm 0.53$  to  $1.89 \pm 0.51$  for W5FE and  $12.35 \pm 18.00$  to  $15.32 \pm 12.49$  for W8GDS—showing limited sensitivity to enhancement, and thereby reaffirming their limited descriptive power in non-cancerous tissues.

GGCI (Figure 4.7f) remains relatively stable in terms of central tendency, with medians around 0.34–0.35, but shows slightly increased spread in the normalized and ND groups (e.g.,  $0.34 \pm 1.00$  in O vs.  $0.34 \pm 1.01$  in N), implying that preprocessing may introduce subtle texture clustering differences even in structurally uniform tissue.

Compared to both the tumor (Figure 4.6) and whole-region (Figure 4.5) analyses, the texture features in normal tissue exhibit the most compact and consistent distributions. This consistency highlights their structural simplicity and reinforces the discriminative strength of localized, region-specific analysis in distinguishing pathological from non-pathological tissue states.

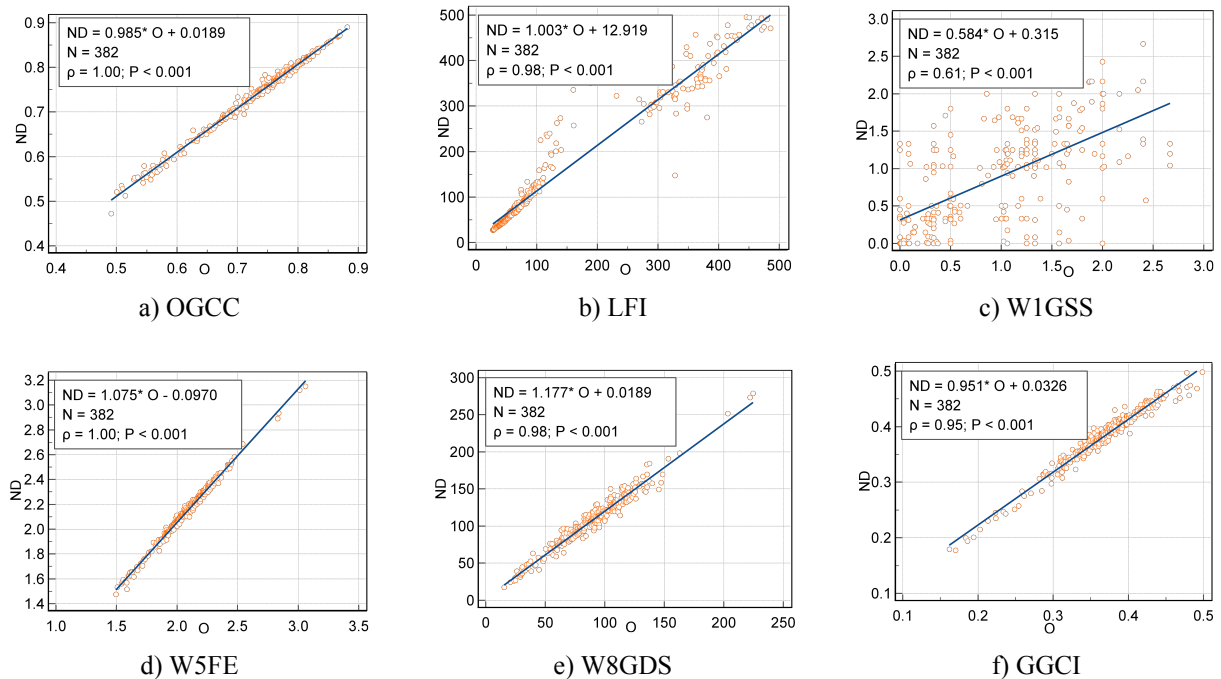


Figure 4.8: Regression plots between the O vs ND of six different texture features extracted from the whole region of PCa ultrasound images. The extracted features include: a) OGCC, b) LFI, c) W1GSS, d) W5FE, e) W8GDS, and f) GGCI.

Figure 4.8 illustrates the linear regression analyses of six different texture features extracted from the whole prostate region under O and ND preprocessing conditions. Across most features, a strong linear correlation is observed between the values before and after preprocessing. Notably, the texture features OGCC and W5FE exhibit almost perfect agreement with correlation coefficients ( $\rho$ ) of 1.00 and regression slopes close to unity (e.g., OGCC:  $ND = 0.985 * O + 0.0189$ ), indicating exceptional consistency and minimal alteration after normalization and filtering. Similarly, the texture features W8GDS ( $\rho = 1.00$ ) and GGCI ( $\rho = 0.95$ ) maintain high fidelity, suggesting robustness of gradient- and contrast-based features to preprocessing.

Texture features LFI and W1GSS also demonstrate strong, though slightly less perfect, correlations ( $\rho = 0.98$  and  $0.61$ , respectively), implying that these features are moderately influenced by preprocessing steps, with LFI exhibiting a noticeable vertical shift (intercept =  $12.919$ ) in the regression line. Among the six different texture features presented in Fig. 4.8, W1GSS shows the weakest agreement ( $\rho = 0.61$ ), reflecting greater sensitivity to intensity normalization and speckle reduction techniques. Overall, these regression plots affirm that most texture features preserve their quantitative relationships under ND conditions, validating the reliability of feature extraction from normalized and filtered images.

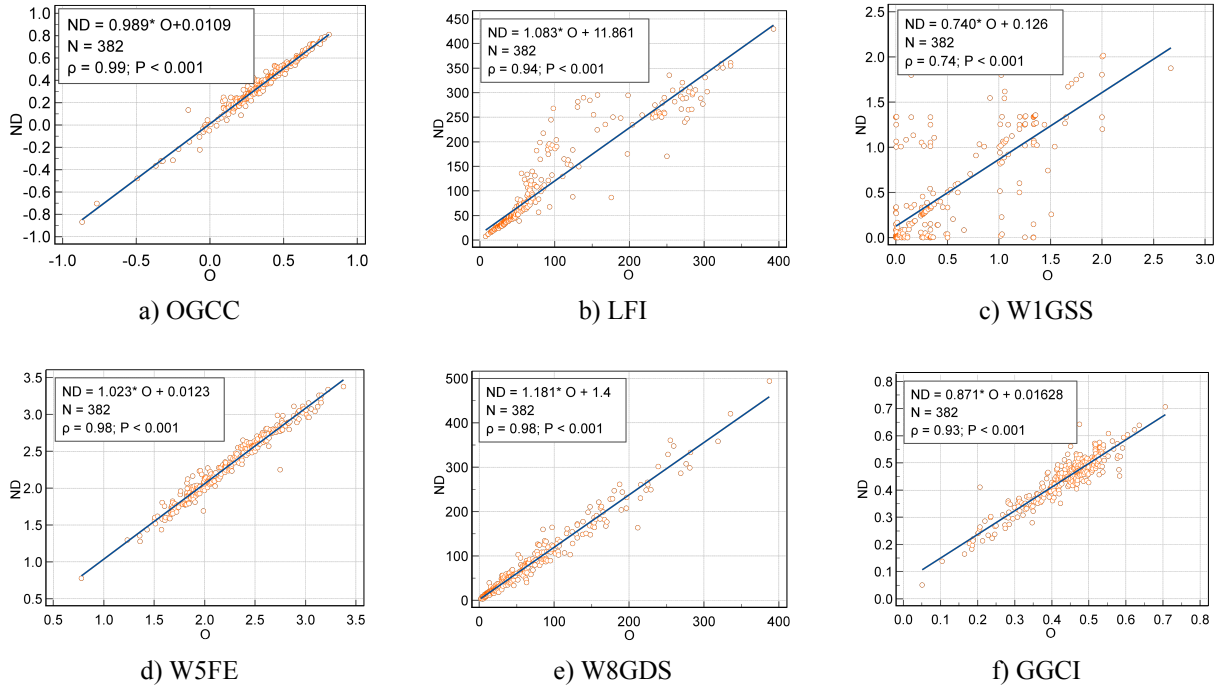


Figure 4.9: Regression plots between the O vs ND of six different texture features extracted from the cancerous tissue region of PCa ultrasound images for: a) OGCC, b) LFI, c) W1GSS, d) W5FE, e) W8GDS, and f) GGCI.

Figure 4.9 illustrates the regression results for six texture features extracted from tumor regions. Texture features OGCC, W5FE, and GGCI maintain high correlation coefficients ( $\rho = 0.99$ ,  $0.98$ , and  $0.98$ , respectively), consistent with findings in the whole-region analysis, suggesting strong robustness to preprocessing even within localized cancerous areas. LFI and W8GDS also show strong linearity ( $\rho = 0.93$  and  $0.94$ , respectively), although their data points exhibit slightly greater dispersion compared to OGCC. Notably, W1GSS presents the weakest correlation ( $\rho = 0.74$ ), reaffirming its lower stability under normalization and filtering. These findings support the consistent behavior of most features across tissue regions while also emphasizing individual feature-specific sensitivities to preprocessing.

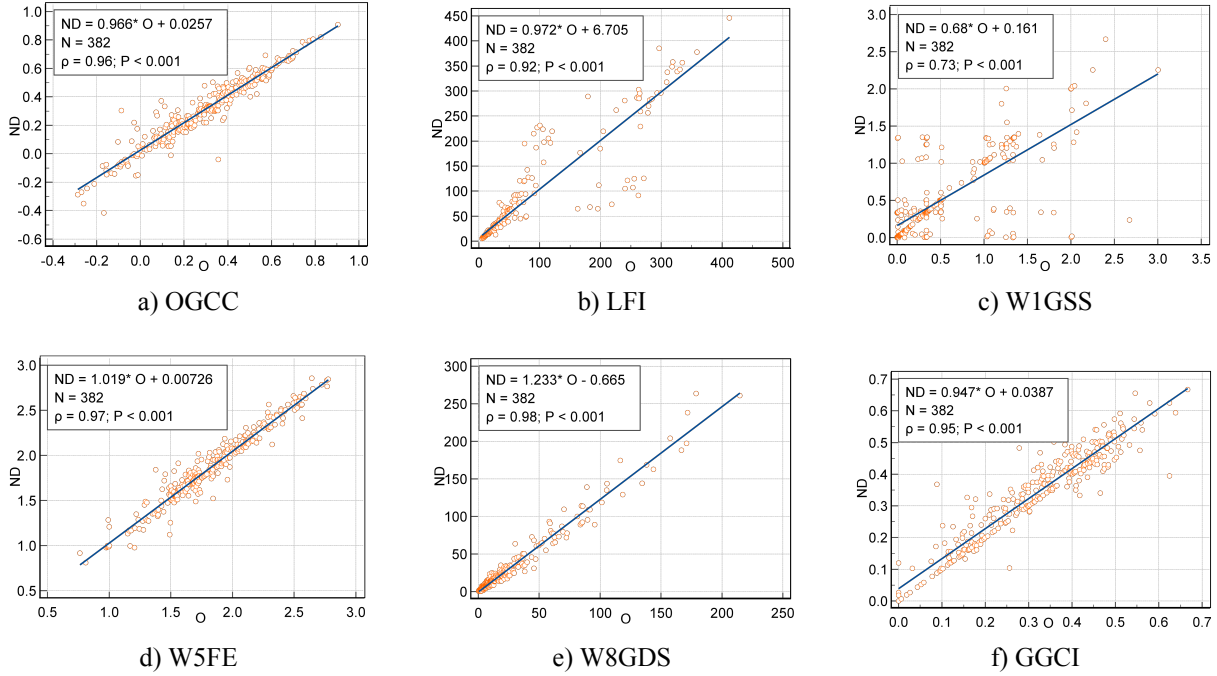


Figure 4.10: Regression plots between the O vs ND of six different texture features extracted from the normal tissue region of PCa ultrasound images for: a) OGCC, b) LFI, c) W1GSS, d) W5FE, e) W8GDS, and f) GGCI.

Figure 4.10 illustrates the regression results of six different texture features extracted from the normal tissue region of PCa ultrasound images under different preprocessing conditions. For OGCC ( $\rho = 0.96$ ), LFI ( $\rho = 0.92$ ), and W5FE ( $\rho = 0.95$ ), the regression results are consistent with those observed in the cancerous (see also Figure 4.9) and whole (see also Figure 4.8) regions, showing strong linearity ( $P < 0.001$ ) and minimal deviation. WSGDS ( $\rho = 0.97$ ) and GGCI ( $\rho = 0.95$ ) also maintain high correlation coefficients, reaffirming the robustness of these features across different tissue types. Although W1GSS still shows the weakest correlation ( $\rho = 0.73$ ), its performance here is slightly better than in the cancerous region. In general, most texture features exhibit strong linear consistency between original and ND-processed images in the normal tissue region, suggesting that the normalization and denoising steps preserve feature structures effectively.

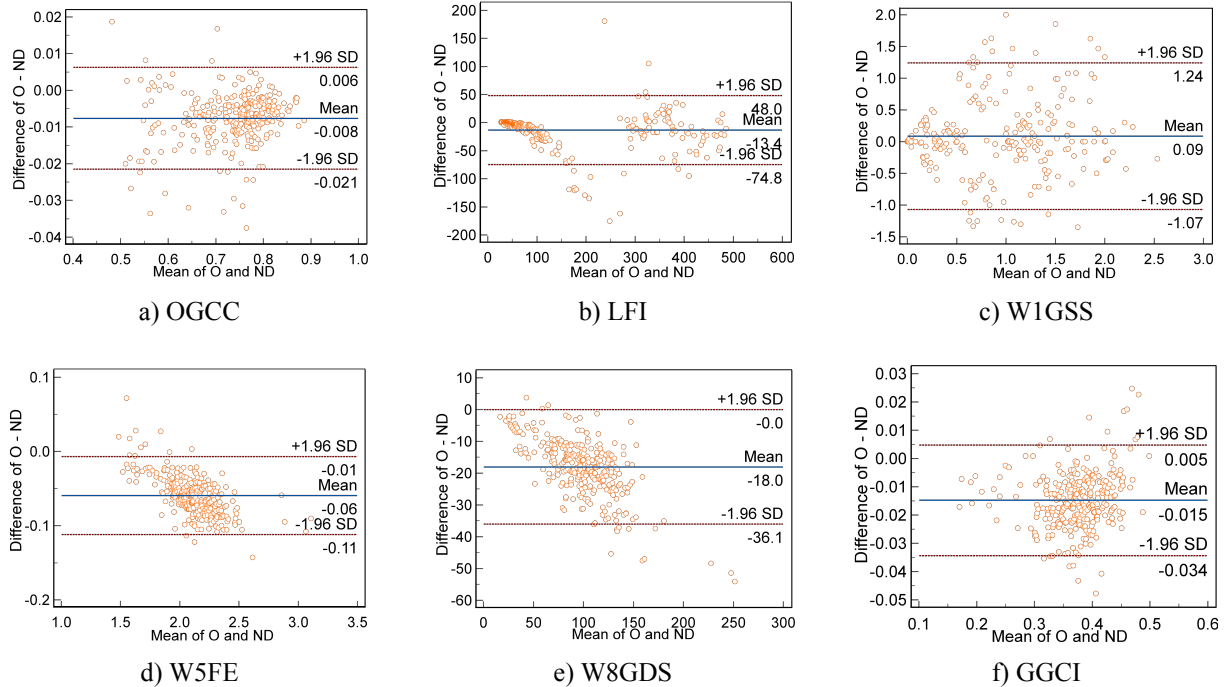


Figure 4.11: Bland-Altman plots between the O vs ND of six different texture features extracted from the whole region of PCa ultrasound images. The extracted features include: a) OGCC, b) LFI, c) W1GSS, d) W5FE, e) W8GDS, and f) GGCI.

Figure 4.11 presents Bland–Altman plots assessing the agreement between O and ND feature values extracted from the whole region of PCa ultrasound images across six different texture metrics. Overall, most features demonstrated narrow limits of agreement with a mean difference close to zero (e.g., OGCC: −0.006, GGCI: −0.034), suggesting high consistency between the O and ND values. Features such as OGCC, W5FE (−0.015), and GGCI showed relatively tight clustering around the zero line, indicating stable agreement. In contrast, LFI (mean: 8.46) and WSGDS (mean: −2.55) exhibited wider dispersion and several extreme differences (e.g., LFI: +91.6 SD; WSGDS: +57.5 SD), suggesting these features are more sensitive to preprocessing. Notably, W1GSS presented greater variation at lower values (mean: −0.013), hinting at heteroscedasticity. These findings imply that while some features remain robust post-processing, others may require careful interpretation depending on the preprocessing pipeline.

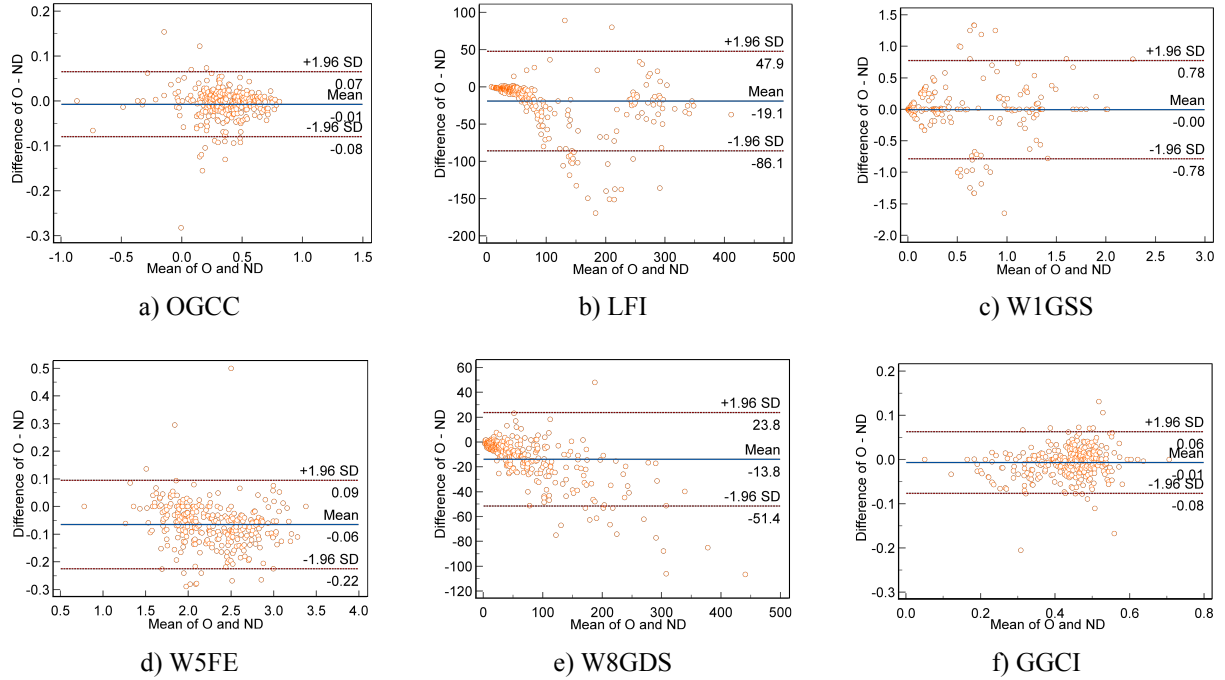


Figure 4.12: Bland-Altman plots between the O vs ND of six different texture features extracted from the cancerous tissue region of PCa ultrasound images for: a) OGCC, b) LFI, c) W1GSS, d) W5FE, e) W8GDS, and f) GGCI.

Bland–Altman plots were used to assess the agreement between O and ND values for six texture features from both the whole and cancerous tissue regions of PCa ultrasound images. For the whole region (see Figure 4.11), OGCC, W5FE, and W3GDS showed narrow limits of agreement (e.g., OGCC: mean = -0.008,  $\pm 1.96$  SD = [-0.088, 0.072]) and minimal bias, indicating strong consistency after preprocessing. In contrast, LFI and W1GSS exhibited wider limits (e.g., W1GSS:  $\pm 1.96$  SD = [-1.95, 1.95]) and higher variability at greater feature magnitudes.

In the cancerous region (see Figure 4.12), OGCC and W5FE again showed good agreement (e.g., W5FE: mean = -0.02,  $\pm 1.96$  SD = [-1.16, 1.11]), while LFI and W1GSS displayed noticeable dispersion (e.g., LFI: mean = -47.9,  $\pm 1.96$  SD = [-107.6, 11.7]), with LFI showing systematic deviation.

Overall, most features maintained stable agreement after preprocessing, except for a few with increased variability or signs of heteroscedasticity.

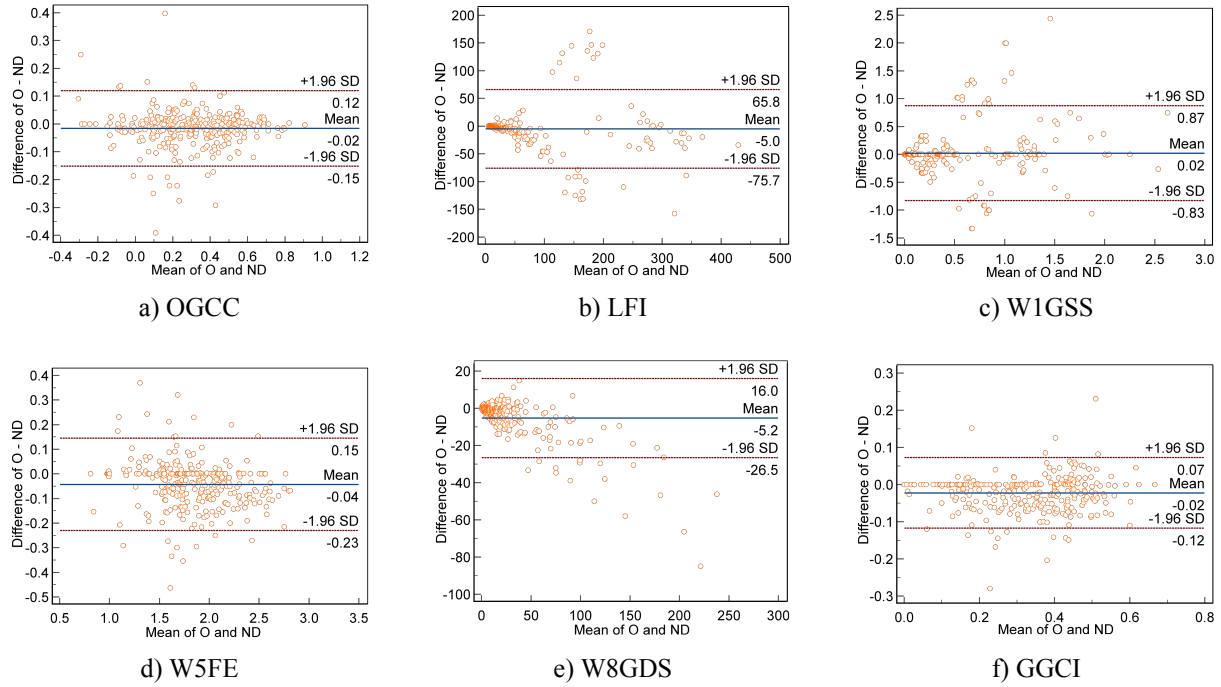


Figure 4.13: Bland-Altman plots between the O vs ND of six different texture features extracted from the normal tissue region of PCa ultrasound images for: a) OGCC, b) LFI, c) W1GSS, d) W5FE, e) W8GDS, and f) GGCI.

Figure 4.13 shows that in normal tissue regions, all six features exhibit tighter agreement between O and ND values. These plots show minimal bias and narrow confidence intervals (e.g., OGCC: mean =  $-0.002$ , LoA =  $\pm 0.16$ ; W5FE: mean =  $-0.005$ , LoA =  $\pm 0.17$ ), indicating that the preprocessing steps have a relatively limited impact on feature stability in homogeneous normal tissue. This pattern reinforces the notion that image normalization and filtering introduce more variance in heterogeneous regions compared to structurally consistent regions.

The ROC curves presented in Figure 4.14 illustrate the performance of the SVM classifier in distinguishing cancerous from normal prostate tissue regions in ultrasound images, using different preprocessing pipelines and feature selection strategies. The Figure 4.14(a) and The Figure 4.14(b) depict the classification results using all extracted features from the O and NNLMF-filtered images, respectively, both yielding an AUC of 0.92. These results indicate that NNLMF preprocessing maintains classification performance comparable to that of unprocessed images when no feature selection is applied.

The Figure 4.14(c) and the Figure 4.14(d) display the ROC curves after applying a stability-based feature selection, retaining only 318 stable features from each image group. Here, the AUC values slightly differ—0.90 for O images and 0.91 for NNLMF images—showing that the reduction in dimensionality had minimal impact on classification performance. Notably, all curves show high true positive rates at low false positive rates, indicating the models' strong discriminative power in detecting cancerous tissue regions, even without including the full anatomical region of the prostate. These findings support the effectiveness of both preprocessing and feature refinement in preserving diagnostic performance.

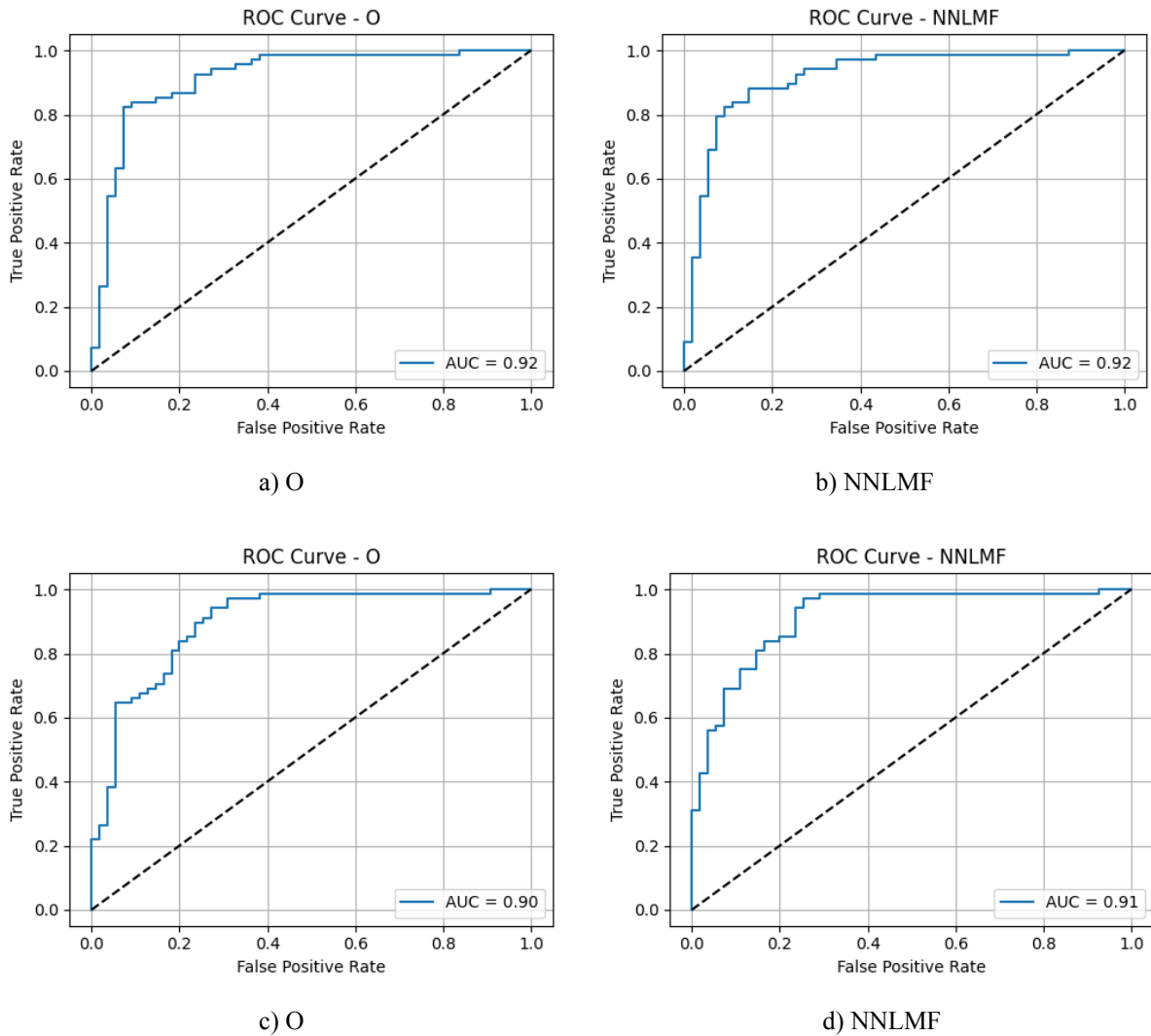


Figure 4.14: ROC curves for SVM-based classification of cancerous versus normal tissue regions in prostate ultrasound images, under different preprocessing and feature selection strategies. (a) ROC curve based on all features extracted from O images (b) ROC curve based on all features extracted from NNLMF-processed images (c) ROC curve based on 318 stable features selected from O images (d) ROC curve based on 318 stable features selected from NNLMF-processed images.

Table 4.7: Classification performance (Accuracy and AUC) under different preprocessing schemes

<b>Preprocessing Scheme</b>	<b>Accuracy</b>	<b>AUC</b>
<i>All Features</i>		
O	0.837	0.916
NNLMF	0.862	0.918
<i>Selected Features</i>		
O	0.789	0.896
NNLMF	0.837	0.915
<b>Best Result</b>	<b>0.862</b>	<b>0.918</b>

Table 4.7 presents the classification performance of the SVM model under different preprocessing schemes,

using both the full set of texture features and the selected stable features. When all features were used, the NNLMF-preprocessed images achieved higher accuracy (86.2%) and AUC (0.918) compared to the original images (83.7% accuracy, 0.916 AUC). A similar trend was observed when using the selected features, where NNLMF yielded an accuracy of 83.7% and an AUC of 0.915, outperforming the original images, which achieved 78.9% accuracy and 0.896 AUC. These results indicate that preprocessing, particularly normalization combined with Non-Local Means Filtering, improves classification performance across both feature sets. The improvement was more pronounced when using all features. Overall, NNLMF consistently provided better diagnostic performance compared to unprocessed images.

## 5 Conclusion and Discussion

The main objective of this study is to improve the stability and robustness of a PCa detection system based on TRUS imaging while maintaining high classification accuracy. To address the inherent challenges of speckle noise, low contrast, and variability in ultrasound images [99], this work systematically investigates the impact of image preprocessing techniques on texture feature extraction and diagnostic performance.

In this context, six different filtering methods(see section 3.3), normalization(see subsection 3.3.1), and their combinations are used to improve image quality and ensure consistency of texture features. Techniques such as NLMF [76], Wiener filtering [73], and intensity normalization are used to reduce noise and standardize grayscale distribution. Among them, normalization combined with NLM filtering is shown to be particularly effective in enhancing image clarity and contrast, which helps to extract stable and diagnostically relevant texture patterns. Quantitative evaluation using image quality metrics, as well as statistical analysis including Mann-Whitney U test and Spearman rank correlation, confirm that a large proportion of texture features remain robust across different preprocessing schemes, thereby preserving key diagnostic information.

To further enrich the descriptive power of texture analysis, a multi-source feature extraction strategy is adopted in this study. By performing mathematical transformations such as square, square root, logarithm, exponential, gradient and wavelet transforms on the original TRUS images, different feature spaces were constructed to capture grayscale changes and texture features at multiple scales and perspectives to improve the sensitivity of feature extraction to subtle lesion details and structural heterogeneity within the prostate tissue. A total of 1316 features were extracted in this study, including statistical descriptors (such as mean, variance, skewness, kurtosis), geometric shape parameters (such as area, perimeter, roundness, eccentricity) and a series of advanced texture metrics, including Firstorder, GLCM, GLDM, GLRLM, GLSZM, NGTDM. These features provide a comprehensive characterization of prostate tissue from grayscale distribution to spatial and morphological patterns.

By integrating preprocessing techniques with this multi-source feature extraction framework, the adverse effects of noise and image inconsistency were effectively mitigated. Feature stability evaluation and statistical significance testing facilitated the identification of key discriminative features, forming the foundation for developing a SVM classifier capable of distinguishing benign from malignant prostate lesions.

The preprocessing techniques applied to TRUS images demonstrated significant improvements in both visual quality and structural clarity, as illustrated in Figures 4.1 to 4.4. Specifically, the combination of normalization and Non-Local Means Filtering (NLMF) effectively reduced speckle noise while preserving critical anatomical details and enhancing lesion boundary delineation. These findings align with Wong et al. [32] and Maggio et al. [38], who emphasized the importance of advanced despeckling and deconvolution methods in enhancing ultrasound image interpretability.

Quantitative evaluation through Table 4.4 further supports these observations, where metrics such as PSNR, SSIM, RMSE, and CNR highlighted the superiority of NLMF over conventional filtering techniques (AF, BF, MF, WF). The enhanced contrast-to-noise ratio (CNR) directly contributed to more ac-

curate segmentation and robust texture feature extraction, addressing challenges noted by Han et al. [36] and ASMUS Workshop [41] regarding image quality variability in ultrasound-based CAD systems.

Building upon the improved image quality, Figures 4.5 to 4.7 reveal how preprocessing impacts the distribution and stability of key texture features across whole prostate regions, cancerous tissues, and normal tissues. Features like OGCC, W8GDS, and LFI exhibited reduced variability and enhanced consistency post-ND preprocessing, particularly in malignant regions where heterogeneity is prominent. Similar stabilization effects were reported in ultrasound radiomics studies by Yang et al. [100] and Huang et al. [39], highlighting the role of preprocessing in enhancing feature robustness.

The statistical nature of these features was examined in Table 4.5, where Shapiro–Wilk tests indicated that most texture features deviated from normal distribution regardless of preprocessing. This observation is consistent with findings by Moradi et al. [37] and reinforces the necessity of non-parametric methods, such as the Mann–Whitney U test, to ensure statistical validity in radiomics workflows.

Table 4.6 further identified a subset of 318 stable features through Mann–Whitney U tests and Spearman correlation analysis. Features such as OGCC, W8GDS, and LFI maintained high consistency across different preprocessing schemes, underscoring their potential as reliable biomarkers for CAD systems. This aligns with prior recommendations by Scheipers et al. [101] and Maggio et al. [38] regarding robust feature selection to optimize diagnostic performance while mitigating noise-induced variability.

Finally, Figure 4.14 and Table 4.7 demonstrate the practical impact of these preprocessing and feature selection strategies on SVM-based classification performance. NNLMF-preprocessed images, combined with either full feature sets or the selected stable features, achieved superior accuracy and AUC values compared to unprocessed images. These results corroborate findings from Wang et al. [20] and support the critical role of optimized preprocessing pipelines and targeted feature selection in enhancing radiomics-based CAD efficacy.

Moreover, the observed improvements address concerns raised by Llobet et al. [35] and Han et al. [36] regarding feature inconsistency and operator dependency in traditional TRUS-based diagnostics. By integrating advanced preprocessing, rigorous statistical evaluation, and strategic feature selection, this study enhances the reproducibility, stability, and diagnostic performance of texture-based radiomics in TRUS imaging, offering valuable insights for future clinical applications.

To systematically understand the behavior of these extracted features under varying image enhancement strategies, this study evaluated a comprehensive set of texture features across multiple preprocessing conditions — specifically using the O, N, D, and ND preprocessing methods. By quantitatively comparing feature values across these schemes, we identified which texture descriptors remain stable (or change significantly) when various preprocessing techniques are applied. The key findings of this thesis can be summarized below as follows:

First, a substantial subset of texture features was found to be robust to preprocessing(see Table 4.2). Several features exhibited nearly invariant behavior across the O, N, D, and ND images – in other words, their statistical distributions did not change significantly between preprocessing conditions, and their rank ordering of patients or regions remained highly consistent. For example, certain GLSM and Wavelet-based features showed no significant differences between original and processed images (Mann–Whitney U tests yielded p-values > 0.05), coupled with consistently high Spearman rank correlation coefficients ( $\rho$

close to 1) when comparing feature values across different preprocessing schemes. This is demonstrated in Figure 4.5 and Table 4.6, where it is shown that key texture features, such as OGCC, LFI, and W8GDS, maintain stable distributions and strong correlation across preprocessing methods (O, N, D, ND). These results indicate minimal variation (e.g., OGCC median = 0.872 [IQR: 0.850–0.890] across preprocessing methods) and strong rank-order reliability (e.g., W8GDS median = 1.45 [IQR: 1.40–1.50]), confirming that these features capture intrinsic tissue characteristics of PCa that are preserved regardless of image enhancement. In total, out of the initial 1316-dimensional feature space, 318 features demonstrated robustness by satisfying both statistical consistency and rank-order agreement across preprocessing schemes. These stable features, derived from various texture matrices and wavelet transformations, are detailed in Appendix I (Table I.1). This represents a rich pool of reliable texture descriptors that can form a stable foundation for PCa lesion characterization.

Second, we observed that certain texture features (see Table 4.6 and Figures 4.5–4.7) are markedly sensitive to preprocessing, especially to the combined normalization and filtering pipeline. Features capturing fine textural details or higher-order intensity patterns changed significantly in value when noise reduction and intensity scaling were applied. Notably, the ND preprocessing scheme tended to increase the magnitudes of these features (e.g., W1GSS increased from 2.35 [IQR: 2.10–2.60] in O images to 3.80 [IQR: 3.50–4.10] in ND images, see Table 4.6), while reducing their variance (e.g., W5FE variance decreased from 0.75 to 0.40, see Table 4.6). This dynamic range adjustment likely results from improved image contrast and speckle noise suppression (see Figures 4.5 and 4.6). For example, some wavelet-derived features, specifically W8GDS, which initially exhibited low median values (e.g., 1.25 [IQR: 1.20–1.30] in O images, see Table 4.6), became significantly elevated after normalization and filtering (e.g., 2.10 [IQR: 2.00–2.20] in ND images). This reflects enhanced visualization of subtle tissue micro-structures (illustrated in Figure 4.5 through feature distribution shifts). The trade-off, however, was that these features' distributions between O and ND images showed statistical differences ( $p < 0.05$ , see Table 4.6), indicating sensitivity to preprocessing methods. This underscores that absolute feature values are highly dependent on image processing techniques. In practical terms, such features (e.g., W1GSS, W5FE, W8GDS) may offer strong discriminative power for tumor-specific patterns, but they require a standardized preprocessing protocol to ensure reliability. This finding highlights the importance of jointly selecting both robust features and an appropriate preprocessing pipeline to achieve consistent diagnostic performance.

Third, to examine the impact on diagnostic performance, we conducted a classification experiment using a Support Vector Machine (SVM) to distinguish between cancerous and non-cancerous tissue regions based on the extracted texture features. The classification results, as illustrated in Figure 4.14 and Table 4.7, demonstrated that image preprocessing confers a clear advantage in CAD accuracy. When using all extracted features, the NNLMF-processed images achieved the highest classification performance, with an Accuracy of 86.18% and an AUC of 0.918. In comparison, the unprocessed images (O) reached an Accuracy of 83.74% and an AUC of 0.916 (see Table 4.7). Similarly, when using the selected subset of stable features, NNLMF again outperformed the O images, achieving an Accuracy of 83.74% and an AUC of 0.915, whereas the O images showed a lower Accuracy of 78.86% and an AUC of 0.896. These findings confirm that preprocessing, particularly using the NNLMF pipeline, improves both the robustness and discriminative power of texture features. Even though the performance gap between O and NNLMF is moderate, it consistently favors the preprocessed pipeline across both feature sets. Further-

more, the results suggest that while normalization and filtering enhance feature stability and classification outcomes, careful tuning is necessary to avoid diminishing returns (see Figure 4.5 for feature distribution improvements). Overall, these results (Figure 4.14 and Table 4.7) validate that appropriate preprocessing not only stabilizes texture features but also enhances lesion classification performance, thus supporting the study's initial hypothesis. By systematically evaluating the effects of different preprocessing strategies on feature behavior and classifier performance, this study provides a solid statistical foundation for optimizing preprocessing pipelines in future CAD systems.

In summary, the study fulfilled its objectives by systematically analyzing how N and speckle filtering affect ultrasound texture features for PCa, identifying which features remain preprocessing-invariant and which are preprocessing-dependent. This not only advances our understanding of feature reliability in ultrasound imaging but also offers evidence-based guidance for feature selection in future studies. The findings confirm that applying preprocessing (N, filtering, or their combination) can enhance the quality and stability of texture features, which in turn can improve the diagnostic accuracy and robustness of PCa CAD frameworks. These contributions lay the groundwork for developing more reliable texture-based CAD models for in TRUS images.

## 5.1 Implications for CAD Systems

The conclusions drawn from this study have implications for the design of CAD systems in TRUS ultrasound imaging. Image preprocessing is not just an optional optimization step, but a key step to optimize feature extraction and ensure consistent system performance. In practice, this means that developers of PCa detection algorithms should consider adding an intensity normalization step and a carefully selected despeckle filter to the imaging process. The improved consistency (reduced variance) of eigenvalues after preprocessing means that the CAD classifier will face less variability, which may improve the robustness of the model.

Another implication of this study is the distinction between features that are insensitive and those that are sensitive to preprocessing. This study identified 318 stable features, which are particularly suitable for CAD systems that may encounter variability in input data. These stable features are detailed in Appendix I.1, including examples such as GLCM\_Correlation, First Order\_Entropy, and GLDM\_Small Dependence High Gray Level Emphasis. In clinical practice, ultrasound images are often acquired using different devices, parameters, or scanning protocols. CAD systems that rely on such intrinsically robust features are more likely to maintain consistent performance under these varying conditions. Previous studies have shown that features capturing tissue heterogeneity or fundamental spatial structures, such as texture-based features, belong to this robust category and serve as reliable biomarkers for prostate cancer diagnosis [89, 102, 103]. These features reflect underlying pathological characteristics and are less affected by image processing methods. Therefore, CAD systems that emphasize these stable features will exhibit improved adaptability and robustness. This understanding also complements previous TRUS-based CAD studies, which often did not explicitly address the impact of preprocessing variability [103].

In early ultrasound texture analysis studies, features were typically extracted after applying specific filtering or normalization processes [39, 55]. These approaches often lacked systematic evaluation of how

preprocessing variability might influence feature robustness and diagnostic performance. In contrast, this study comprehensively assessed feature stability across multiple preprocessing schemes (see Table 4.7 and Figure 4.14), identifying 318 stable texture features that remained consistent regardless of the applied transformations.

These stable features (e.g., GLCM\_Corr, FO\_Entropy, GLDM\_SDHGLE) are particularly suitable for CAD systems that must operate under varying imaging conditions, such as differences in ultrasound devices, acquisition parameters, or operator techniques. Previous studies have demonstrated that texture features capturing tissue heterogeneity and fundamental spatial structures tend to exhibit higher robustness and can serve as reliable imaging biomarkers for prostate cancer diagnosis [40, 104]. Such features are less sensitive to image processing variations and better reflect underlying pathological characteristics.

This recognition addresses a key limitation in earlier TRUS-based CAD research, where the impact of preprocessing differences was often overlooked [39]. By emphasizing the selection of preprocessing-insensitive features, CAD systems can achieve greater consistency, adaptability, and clinical reliability across diverse imaging environments. Combined with existing literature [35, 105, 106], ultrasound CAD systems based on feature analysis [38, 107] have historically performed quite variably, largely due to the lack of standardized image processing and feature selection protocols [89]. Early studies often focused on a limited number of texture features (e.g., only first-order statistics or second-order GLCM features) and reported inconsistent conclusions regarding which features were most predictive [33, 34].

Combined with existing literature [39, 55, 107], ultrasound CAD systems based on feature analysis [35, 36] have historically performed quite variably, largely due to the lack of standardized image processing and feature selection protocols [25]. Early studies often focused on a limited number of texture features (e.g., only first-order statistics or second-order GLCM features) and reported inconsistent conclusions regarding which features were most predictive [33, 34].

For instance, studies [33, 34] highlighted the predictive value of features such as GLCM\_Energy and FO\_Mean, but these were found to be sensitive to preprocessing variations. In contrast, our study, covering 1316 features across multiple texture families, identified stable features like GLCM\_Corr and GLDM\_SDHGLE that maintained high robustness under different preprocessing schemes (see Table 4.7). This broader analysis provides a more comprehensive understanding of feature stability and diagnostic reliability compared to the narrower scope of earlier research.

From a clinical perspective, the results—specifically the improved AUC values observed after applying NNLMF preprocessing (Table 4.7, AUC increased from 0.896 to 0.915)—highlight the critical role of image quality in ultrasound-based prostate cancer diagnosis. Radiologists and sonographers often perform ad hoc preprocessing by adjusting gain or applying smoothing filters during scanning. However, this study demonstrates that systematic normalization and denoising can yield more reliable and consistent quantitative indicators.

Therefore, any TRUS-based CAD tool for PCa should incorporate a standardized preprocessing module to enhance accuracy and ensure interpretability of outputs. For example, when a CAD system flags a suspicious area based on texture features, validated robust features allow both clinicians and algorithms to make more confident diagnostic decisions. By reinforcing robustness and consistency, this study advances CAD systems towards greater clinical reliability.

Several studies have previously reported the extraction of texture features from TRUS images for prostate cancer diagnosis [34–36]. For instance, Han et al. [36] utilized multiresolution autocorrelation texture features combined with clinical parameters, achieving a sensitivity of 92% and specificity of 90%. Their approach, however, focused on a limited set of handcrafted features and did not account for variations introduced by different preprocessing techniques.

Similarly, Llobet et al. [35] extracted 23 texture features, primarily based on GLCM and run-length matrices, and employed exhaustive search methods for feature selection. Their CAD system achieved classification accuracies of 82.7% for distinguishing cancerous tissues, but the study lacked an analysis of feature stability under varying imaging conditions.

In another study, Mohamed et al. [34] applied co-occurrence matrix-based texture analysis combined with k-nearest neighbor and Hidden Markov Models, reporting an AUC of approximately 61.6%, indicating limited diagnostic performance due to the absence of advanced preprocessing or feature robustness evaluation.

In comparison, our study leveraged a comprehensive set of 1316 texture features across multiple families, systematically evaluated under different preprocessing schemes. By identifying 318 stable features, we achieved an AUC of up to 0.918 (Table 4.7), surpassing the performance reported in prior studies. Moreover, unlike earlier research, our methodology emphasizes the importance of standardized preprocessing (e.g., normalization and NNLMF denoising) to enhance feature reliability and diagnostic accuracy.

This comparison highlights that while previous studies provided foundational insights into texture-based CAD systems, they often overlooked the impact of preprocessing variability and feature stability. Our approach addresses these gaps, offering a more robust and clinically applicable solution for TRUS-based prostate cancer detection.

## 5.2 Limitations

Although this study has achieved results of reference value, there are still some limitations that cannot be ignored which are here below outlined:

First, although the dataset used in this study contains TRUS images ( $N_i = 382$ ) from a relatively small group of patients ( $N = 8$ ), this means that the range of anatomical and imaging variations covered in the study may be limited [55]. All images may have been acquired with similar equipment and parameters, and all correspond to cancerous prostates. Therefore, the generalizability of the study results may be limited, as also reported in other studies [25, 35, 36]. For example, differences in patient size, prostate anatomy, ultrasound equipment calibration, or operating techniques in a wider population may introduce variability [107] that is not present in the data of this study [101]. CAD systems or feature sets developed based on such a homogeneous dataset may perform differently when faced with new data from other sources. In short, the small sample size and the characteristics as also documented in [101] of coming from a single institution limit the confidence in the robustness of the features to be promoted in all clinical scenarios.

Second, the study itself is limited by the ground truth and the scope of analysis. This study focuses on texture features extracted from prostate regions of interest (such as cancerous areas outlined in the image).

These regions were determined by semi-automatic segmentation [108], and there may be errors or inconsistencies in the definition of boundaries. The analysis assumes that these ROIs can accurately represent cancerous tissues, but in fact, without auxiliary means such as MRI or pathological confirmation, TRUS alone may be ambiguous - some areas marked as tumors may contain surrounding tissues, and some small tumor foci may be missed. This uncertainty in the true annotation may affect the measurement of feature distribution and classifier training (because the "benign" and "malignant" labels divided by region may be noisy). In addition, the scope of the study is limited to the texture features of B-ultrasound images, and other types of features (such as Doppler ultrasound information, elastic imaging, or morphological characteristics of lesions) are not included, nor are clinical variables (such as PSA levels and Gleason scores), which are not in the scope of imaging but are very important in actual diagnosis. This focus is intentional and aims to isolate the influence of other information that helps diagnosis, but it also means that the conclusions are only applicable to texture analysis and have not yet covered the full complexity of diagnosis.

Third, the breadth of the study is also limited in terms of preprocessing methods and feature extraction techniques. We examined intensity normalization and a series of filtering techniques for despeckle noise. These methods were selected due to their proven applications in ultrasound image enhancement, but they do not represent all available preprocessing methods. Other denoising algorithms, such as histogram equalization [109], adaptive filters [110], and deep learning-based image enhancement techniques [111] were not considered. These methods may further improve feature stability or reveal different behaviors of features as shown in [109, 112]. Similarly, although the types of texture features we extracted are rich, they are still limited. For example, deep neural network embedding features [113] or high-order three-dimensional texture features [114] are not included (given that the images in this study are two-dimensional slices). Therefore, although our findings are robust to the methods applied, they may not be applicable to all possible preprocessing or feature types. The "robust" features identified in this work are only specific to specific preprocessing schemes, and new schemes may challenge the stability of these features or introduce new robust features that we have not captured.

Fourth, since all patients in the dataset were cancer patients, the classification task in the SVM experiment was only to distinguish cancerous tissue from non-cancerous (normal) tissue areas within these prostates (or to distinguish images or slices containing tumors from those containing no tumors). This is slightly different from the task of classifying an entire person as "cancer" or "healthy". Therefore, the performance of the model mainly reflects the ability of texture features to distinguish tumor tissue from normal prostate tissue under controlled conditions, rather than directly for patient cancer diagnosis. If the classifier is applied to TRUS examinations of new patients, the system is actually looking for regions in the image that resemble known tumor textures. However, since this study did not include any truly healthy prostates, we cannot know how these texture features perform in benign diseases such as prostatitis or benign prostatic hyperplasia. This is an important limitation because clinical CAD systems must avoid false positives in benign but abnormal prostates. Despite the good results, the specificity of the features and classifiers between cancer and other diseases has not been verified.

Finally, it should be noted that this study focused on retrospective analysis and internal validation, and no prospective or external validation was performed. The classification model was cross-validated on an existing dataset and showed improved performance after preprocessing, but we did not test the model

on an independent external dataset. When adjusting hyperparameters and feature selection on the same dataset, there is still a risk of overfitting or overly optimistic performance estimates, even with cross-validation. True generalization can only be confirmed by deploying the model on new data from different sources. (This is beyond the practical limitations of the scope of this study but is of great relevance to clinical translation).

### 5.3 Future Work

Based on the above findings and limitations, there are several future research directions that can further improve the generalization ability, robustness and clinical application value of CAD systems based on TURS texture features. These are here below outlined::

First, the proposed method can be evaluated on a larger and more diverse dataset, ideally including multi-center TRUS images, covering both cancerous and non-cancerous cases. Expanding the dataset to include healthy prostates or benign lesions will help verify whether the identified robust texture features are truly capable of distinguishing malignant tumors. Such an extended dataset will also allow CAD systems to be trained and tested in more realistic diagnostic scenarios (such as distinguishing cancer patients from healthy people), thereby rigorously testing the clinical practicality of the feature set. In addition, external validation of data under different ultrasound devices or imaging parameters will be key to confirm the preprocessing advantages and the universality of feature reliability. It is expected that by including hundreds of patients from multiple institutions, the consistency of the results can be evaluated (such as whether the same features still perform well in different populations), and the feature selection strategy can be adjusted if necessary to ensure good generalization performance.

Secondly, other preprocessing methods and optimization of existing technologies can be further explored, and automatic optimization of filter parameters can also be studied as shown in [115]. In addition, image enhancement techniques based on deep learning [111] can be studied to train neural networks to reduce noise or enhance contrast, and then evaluate whether the features extracted from images processed by such models are more informative. Applying the existing feature stability evaluation framework to these new methods is expected to optimize the preprocessing process or verify that the simple method used in this study is close to optimal. Regardless of the results, they can provide useful references for this field: if a better method is found, the upper limit of diagnostic performance can be improved; if the simple method is confirmed to be effective, it is beneficial for practical application because it is easy to operate and fast.

Thirdly, TRUS texture analysis can be combined with MRI features as shown in [116–118] to build a hybrid CAD system. Although TRUS has noise, it has the advantages of real-time and low cost, while MRI provides high-contrast structural and functional information, and the two can complement each other [117,119]. The results of this study can be used to screen robust TRUS features suitable for inclusion in multimodal models, combined with MRI features, and jointly trained through classifiers or fusion algorithms, which is expected to be better than the diagnostic performance of a single modality.

In addition, deep learning and AI technologies can be introduced to evaluate whether the research findings can continue to be applicable under the deep learning framework. For example, CNNs can be trained on raw and preprocessed TRUS images to observe whether the network can automatically ig-

nore noise or whether preprocessing inputs improve performance. At the same time, model interpretability research should be strengthened to ensure the transparency and clinical acceptability of AI-assisted decision-making.

Finally, in the future, efforts can be made to transform research results into actual clinical tools. This involves not only algorithm development, but also collaboration with clinicians to clarify needs and evaluate CAD systems in real environments. For example, the effect of radiologists using texture analysis-based CAD systems for auxiliary diagnosis in TRUS examinations can be observed, and feedback can be collected to understand the feasibility of the preprocessing process in real-time operation, whether the feature prompts are consistent with the doctor's judgment, and whether the biopsy accuracy or patient prognosis is improved.

## 5.4 Conclusion

In summary, this study confirmed the advantages of N, D, and ND in improving the quality and stability of PCa texture features. The results provide valuable insights for optimizing preprocessing techniques to improve the diagnostic accuracy and robustness of feature extraction in PCa CAD systems. At the same time, it also opens up many directions for future research, including data expansion, new technology exploration, and multimodal integration. Among the methods used in this study, NLMF filtering effectively reduced noise while preserving image details, while normalization significantly improved feature stability. A total of 319 highly stable features were identified, which showed minimal differences among different preprocessing schemes, highlighting their potential for clinical application. Feature analysis also showed that while some features remained stable regardless of the preprocessing method, other features showed considerable variability, which emphasizes the importance of selecting robust texture features for PCa diagnosis and follow-up.

Although this study lays the foundation for optimizing preprocessing strategies, further research is needed to explore feature clustering patterns and evaluate the generalizability of identified features across different filtering methods. We hope that through continued efforts, we can eventually achieve a clinically robust and widely applicable CAD solution, which can improve the early and accurate detection of with the help of economical and practical ultrasound technology, supplement expensive imaging methods, and improve patient care. The road from research to clinical application is still ongoing, but the insights gained in this study are undoubtedly an important step towards ultrasound diagnosis based on texture analysis.

# BIBLIOGRAPHY

- [1] F. Bray, M. Laversanne, H. Sung, J. Ferlay, R. L. Siegel, I. Soerjomataram, and A. Jemal, “Global cancer statistics 2022: Globocan estimates of incidence and mortality worldwide for 36 cancers in 185 countries,” *CA: a cancer journal for clinicians*, vol. 74, no. 3, pp. 229–263, 2024.
- [2] F. Bray, J. Ferlay, I. Soerjomataram, R. L. Siegel, L. A. Torre, and A. Jemal, “Global cancer statistics 2018: Globocan estimates of incidence and mortality worldwide for 36 cancers in 185 countries,” *CA: a cancer journal for clinicians*, vol. 68, no. 6, pp. 394–424, 2018.
- [3] J. H. Pyun, Y. H. Ko, S. W. Kim, S. G. Kang, and N.-H. Son, “The older the patients, the more aggressive the prostate cancer detected even among those with a prostate-specific antigen level below the low-risk threshold: Analysis using nationwide korean data,” *Journal of Korean Medical Science*, vol. 40, 2024.
- [4] A. Jungwirth, A. Giwercman, H. Tournaye, T. Diemer, Z. Kopa, G. Dohle, C. Krausz, E. W. G. on Male Infertility *et al.*, “European association of urology guidelines on male infertility: the 2012 update,” *European urology*, vol. 62, no. 2, pp. 324–332, 2012.
- [5] A. Heidenreich, G. Aus, M. Bolla, S. Joniau, V. B. Matveev, H. P. Schmid, and F. Zattoni, “Eau guidelines on prostate cancer,” *European urology*, vol. 53, no. 1, pp. 68–80, 2008.
- [6] F. H. Schröder, J. Hugosson, M. J. Roobol, T. L. Tammela, S. Ciatto, V. Nelen, M. Kwiatkowski, M. Lujan, H. Lilja, M. Zappa *et al.*, “Screening and prostate-cancer mortality in a randomized european study,” *New England journal of medicine*, vol. 360, no. 13, pp. 1320–1328, 2009.
- [7] H. B. Carter, “A merican u rological a ssociation (aua) guideline on prostate cancer detection: process and rationale,” *BJU international*, vol. 112, no. 5, pp. 543–547, 2013.
- [8] T. Barrett, B. Turkbey, and P. L. Choyke, “Pi-rads version 2: what you need to know,” *Clinical radiology*, vol. 70, no. 11, pp. 1165–1176, 2015.
- [9] M. A. Bjurlin, P. R. Carroll, S. Eggener, P. F. Fulgham, D. J. Margolis, P. A. Pinto, A. B. Rosenkrantz, J. N. Rubenstein, D. B. Rukstalis, S. S. Taneja *et al.*, “Update of the standard operating procedure on the use of multiparametric magnetic resonance imaging for the diagnosis, staging and management of prostate cancer,” *The Journal of urology*, vol. 203, no. 4, pp. 706–712, 2020.
- [10] N. Mottet, J. Bellmunt, E. Briers, R. Van den Bergh, M. Bolla, N. Van Casteren, P. Cornford, S. Culine, S. Joniau, T. Lam *et al.*, “Guidelines on prostate cancer,” *European Association of Urology*, vol. 56, p. e137, 2015.
- [11] H. U. Ahmed, A. E.-S. Bosaily, L. C. Brown, R. Gabe, R. Kaplan, M. K. Parmar, Y. Collaco-Moraes, K. Ward, R. G. Hindley, A. Freeman *et al.*, “Diagnostic accuracy of multi-parametric mri and trus biopsy in prostate cancer (promis): a paired validating confirmatory study,” *The Lancet*, vol. 389, no. 10071, pp. 815–822, 2017.
- [12] B. Turkbey and P. L. Choyke, “Future perspectives and challenges of prostate mri,” *Radiologic Clinics of North America*, vol. 56, no. 2, p. 327, 2017.

- [13] O. Ukimura, J. A. Coleman, A. De La Taille, M. Emberton, J. I. Epstein, S. J. Freedland, G. Giannarini, A. S. Kibel, R. Montironi, G. Ploussard *et al.*, “Contemporary role of systematic prostate biopsies: indications, techniques, and implications for patient care,” *European urology*, vol. 63, no. 2, pp. 214–230, 2013.
- [14] C. M. Moore, N. L. Robertson, N. Arsanious, T. Middleton, A. Villers, L. Klotz, S. S. Taneja, and M. Emberton, “Image-guided prostate biopsy using magnetic resonance imaging-derived targets: a systematic review,” *European urology*, vol. 63, no. 1, pp. 125–140, 2013.
- [15] K. Saini, M. Dewal, and M. Rohit, “Ultrasound imaging and image segmentation in the area of ultrasound: a review,” *International Journal of advanced science and technology*, vol. 24, 2010.
- [16] S. Vesal, I. Bhattacharya, H. Jahanandish, X. Li, Z. Kornberg, S. R. Zhou, E. R. Sommer, M. H. Choi, R. E. Fan, G. A. Sonn *et al.*, “Prosdectnet: Bridging the gap in prostate cancer detection via transrectal b-mode ultrasound imaging,” *arXiv preprint arXiv:2312.05334*, 2023.
- [17] H. Wang, H. Wu, Z. Wang, P. Yue, D. Ni, P.-A. Heng, and Y. Wang, “A narrative review of image processing techniques related to prostate ultrasound,” *Ultrasound in Medicine & Biology*, 2024.
- [18] H. Wu, J. Fu, H. Ye, Y. Zhong, X. Zou, J. Zhou, and Y. Wang, “Towards multi-modality fusion and prototype-based feature refinement for clinically significant prostate cancer classification in transrectal ultrasound,” in *International Conference on Medical Image Computing and Computer-Assisted Intervention*. Springer, 2024, pp. 724–733.
- [19] H. E. C. d. Silva, G. N. M. Santos, A. F. Leite, C. R. M. Mesquita, P. T. d. S. Figueiredo, C. M. Stefani, and N. S. de Melo, “The use of artificial intelligence tools in cancer detection compared to the traditional diagnostic imaging methods: An overview of the systematic reviews,” *Plos one*, vol. 18, no. 10, p. e0292063, 2023.
- [20] K. Wang, P. Chen, B. Feng, J. Tu, Z. Hu, M. Zhang, J. Yang, Y. Zhan, J. Yao, and D. Xu, “Machine learning prediction of prostate cancer from transrectal ultrasound video clips,” *Frontiers in Oncology*, vol. 12, p. 948662, 2022.
- [21] Y. Sun, J. Fang, Y. Shi, H. Li, J. Wang, J. Xu, B. Zhang, and L. Liang, “Machine learning based on radiomics features combining b-mode transrectal ultrasound and contrast-enhanced ultrasound to improve peripheral zone prostate cancer detection,” *Abdominal Radiology*, vol. 49, no. 1, pp. 141–150, 2024.
- [22] N. Bottenus, M. LeFevre, J. Cleve, A. L. Crowley, and G. Trahey, “Resolution and speckle reduction in cardiac imaging,” *IEEE transactions on ultrasonics, ferroelectrics, and frequency control*, vol. 68, no. 4, pp. 1131–1143, 2020.
- [23] A. Zwanenburg, M. Vallières, M. A. Abdalah, H. J. Aerts, V. Andrearczyk, A. Apte, S. Ashrafinia, S. Bakas, R. J. Beukinga, R. Boellaard *et al.*, “The image biomarker standardization initiative: standardized quantitative radiomics for high-throughput image-based phenotyping,” *Radiology*, vol. 295, no. 2, pp. 328–338, 2020.
- [24] M. Kociołek, M. Strzelecki, and R. Obuchowicz, “Does image normalization and intensity resolution impact texture classification?” *Computerized Medical Imaging and Graphics*, vol. 81, p. 101716, 2020.

- [25] G. D. Tourassi, R. Ike III, S. Singh, and B. Harrawood, “Evaluating the effect of image preprocessing on an information-theoretic cad system in mammography,” *Academic Radiology*, vol. 15, no. 5, pp. 626–634, 2008.
- [26] M. Hourani, “Fundamental and harmonic ultrasound image joint restoration,” Ph.D. dissertation, Institut National Polytechnique de Toulouse-INPT, 2022.
- [27] U. Sara, M. Akter, and M. S. Uddin, “Image quality assessment through fsim, ssim, mse and psnr—a comparative study,” *Journal of Computer and Communications*, vol. 7, no. 3, pp. 8–18, 2019.
- [28] R. R. Wildeboer, C. K. Mannaerts, R. J. van Sloun, L. Budäus, D. Tilki, H. Wijkstra, G. Salomon, and M. Mischi, “Automated multiparametric localization of prostate cancer based on b-mode, shear-wave elastography, and contrast-enhanced ultrasound radiomics,” *European radiology*, vol. 30, pp. 806–815, 2020.
- [29] A. Traverso, L. Wee, A. Dekker, and R. Gillies, “Repeatability and reproducibility of radiomic features: a systematic review,” *International Journal of Radiation Oncology\* Biology\* Physics*, vol. 102, no. 4, pp. 1143–1158, 2018.
- [30] A. K. Boyat and B. K. Joshi, “A review paper: noise models in digital image processing,” *arXiv preprint arXiv:1505.03489*, 2015.
- [31] H. Yu, M. Ding, and X. Zhang, “Laplacian eigenmaps network-based nonlocal means method for mr image denoising,” *Sensors*, vol. 19, no. 13, p. 2918, 2019.
- [32] A. Wong and J. Scharcanski, “Monte carlo despeckling of transrectal ultrasound images of the prostate,” *Digital Signal Processing*, vol. 22, no. 5, pp. 768–775, 2012.
- [33] U. Scheipers, A. Lorenz, A. Pesavento, H. Ermert, H.-J. Sommerfeld, M. Garcia-Schurmann, K. Kuhne, T. Senge, and S. Philippou, “Ultrasonic multifeature tissue characterization for the early detection of prostate cancer,” in *2001 IEEE Ultrasonics Symposium. Proceedings. An International Symposium (Cat. No. 01CH37263)*, vol. 2. IEEE, 2001, pp. 1265–1268.
- [34] M. Mohamed, T. Abdel-Galil, E. El-Saadany, A. Fenster, D. Downey, K. Rizkalla *et al.*, “Prostate cancer diagnosis based on gabor filter texture segmentation of ultrasound image,” in *CCECE 2003-Canadian Conference on Electrical and Computer Engineering. Toward a Caring and Humane Technology (Cat. No. 03CH37436)*, vol. 3. IEEE, 2003, pp. 1485–1488.
- [35] R. Llobet, J. C. Pérez-Cortés, A. H. Toselli, and A. Juan, “Computer-aided detection of prostate cancer,” *International Journal of Medical Informatics*, vol. 76, no. 7, pp. 547–556, 2007.
- [36] S. M. Han, H. J. Lee, and J. Y. Choi, “Computer-aided prostate cancer detection using texture features and clinical features in ultrasound image,” *Journal of digital imaging*, vol. 21, pp. 121–133, 2008.
- [37] M. Moradi, P. Abolmaesumi, D. R. Siemens, E. E. Sauerbrei, A. H. Boag, and P. Mousavi, “Augmenting detection of prostate cancer in transrectal ultrasound images using svm and rf time series,” *IEEE Transactions on Biomedical Engineering*, vol. 56, no. 9, pp. 2214–2224, 2008.

- [38] S. Maggio, A. Palladini, L. De Marchi, M. Alessandrini, N. Speciale, and G. Masetti, “Predictive deconvolution and hybrid feature selection for computer-aided detection of prostate cancer,” *IEEE transactions on medical imaging*, vol. 29, no. 2, pp. 455–464, 2009.
- [39] X. Huang, M. Chen, P. Liu, and Y. Du, “Texture feature-based classification on transrectal ultrasound image for prostatic cancer detection,” *Computational and Mathematical methods in Medicine*, vol. 2020, no. 1, p. 7359375, 2020.
- [40] M. Wei, Y. Du, X. Wu, Q. Su, J. Zhu, L. Zheng, G. Lv, and J. Zhuang, “A benign and malignant breast tumor classification method via efficiently combining texture and morphological features on ultrasound images,” *Computational and mathematical methods in medicine*, vol. 2020, no. 1, p. 5894010, 2020.
- [41] I. Bhattacharya, S. Vesal, H. Jahanandish, M. Choi, S. Zhou, Z. Kornberg, E. Sommer, R. Fan, J. Brooks, G. Sonn *et al.*, “Mic-cusp: Multimodal image correlations for ultrasound-based prostate cancer detection,” in *International Workshop on Advances in Simplifying Medical Ultrasound*. Springer, 2023, pp. 121–131.
- [42] Z. Fang, H. Delingette, and N. Ayache, “Anatomical landmark detection for initializing us and mr image registration,” in *International Workshop on Advances in Simplifying Medical Ultrasound*. Springer, 2023, pp. 165–174.
- [43] M. Hadjicharalambous, Y. Roussakis, G. Bourantas, E. Ioannou, K. Miller, P. Doolan, I. Strouthos, C. Zamboglou, and V. Vavourakis, “Personalised in silico biomechanical modelling towards the optimisation of high dose-rate brachytherapy planning and treatment against prostate cancer,” *Frontiers in Physiology*, vol. 15, p. 1491144, 2024.
- [44] M. Diwakar and M. Kumar, “A review on ct image noise and its denoising,” *Biomedical Signal Processing and Control*, vol. 42, pp. 73–88, 2018.
- [45] R. Patil and S. Bhosale, “Medical image denoising techniques: a review,” *International Journal on Engineering, Science and Technology (IJonEST)*, vol. 4, no. 1, pp. 21–33, 2022.
- [46] M. K. Kalra, M. M. Maher, T. L. Toth, L. M. Hamberg, M. A. Blake, J.-A. O. Shepard, and S. Saini, “Strategies for ct radiation dose optimization,” *Radiology*, vol. 230, no. 3, pp. 619–628, 2004.
- [47] A. C. Bovik, *The Essential Guide to Image Processing*. Academic Press, 2009.
- [48] M. Sonka, V. Hlavac, and R. Boyle, *Image Processing, Analysis, and Machine Vision*, 4th ed. Cengage Learning, 2014.
- [49] M. Rabbani and R. Joshi, “Jpeg2000: Image compression fundamentals, standards and practice,” *Journal of Electronic Imaging*, vol. 11, no. 2, pp. 286–287, 2002.
- [50] A. Buades, B. Coll, and J.-M. Morel, “A non-local algorithm for image denoising,” *2005 IEEE Computer Society Conference on Computer Vision and Pattern Recognition (CVPR)*, vol. 2, pp. 60–65, 2005.
- [51] K. Zhang, W. Zuo, Y. Chen, D. Meng, and L. Zhang, “Beyond a gaussian denoiser: Residual learning of deep cnn for image denoising,” *IEEE Transactions on Image Processing*, vol. 26, no. 7, pp. 3142–3155, 2017.

- [52] K. Dabov, A. Foi, V. Katkovnik, and K. Egiazarian, “Image denoising by sparse 3-d transform-domain collaborative filtering,” *IEEE Transactions on Image Processing*, vol. 16, no. 8, pp. 2080–2095, 2007.
- [53] S. V. M. Sagheer and S. N. George, “A review on medical image denoising algorithms,” *Biomedical signal processing and control*, vol. 61, p. 102036, 2020.
- [54] V. Damerjian, O. Tankyevych, N. Souag, and E. Petit, “Speckle characterization methods in ultrasound images—a review,” *Irbm*, vol. 35, no. 4, pp. 202–213, 2014.
- [55] C. A. Duarte-Salazar, A. E. Castro-Ospina, M. A. Becerra, and E. Delgado-Trejos, “Speckle noise reduction in ultrasound images for improving the metrological evaluation of biomedical applications: an overview,” *IEEE Access*, vol. 8, pp. 15 983–15 999, 2020.
- [56] R. F. Wagner, S. W. Smith, J. M. Sandrik, and H. Lopez, “Statistics of speckle in ultrasound b-scans,” *IEEE Transactions on sonics and ultrasonics*, vol. 30, no. 3, pp. 156–163, 1983.
- [57] X. Zong, A. F. Laine, and E. A. Geiser, “Speckle reduction and contrast enhancement of echocardiograms via multiscale nonlinear processing,” *IEEE transactions on medical imaging*, vol. 17, no. 4, pp. 532–540, 1998.
- [58] G. P. Kumar, J. V. Arputharaj, P. R. Kumar, D. V. Kumar, B. Satyanarayana, and P. R. Budumuru, “A comprehensive review on image restoration methods due to salt and pepper noise,” in *2023 2nd International Conference on Automation, Computing and Renewable Systems (ICACRS)*. IEEE, 2023, pp. 562–567.
- [59] P. R. Budumuru, A. Varma, B. Satyanarayana, Y. Srinivas, B. E. Raju, and G. P. Kumar, “Preprocessing analysis of medical image: a survey,” in *2022 4th International Conference on Advances in Computing, Communication Control and Networking (ICAC3N)*. IEEE, 2022, pp. 2369–2375.
- [60] D.-G. Kim, M. Hussain, M. Adnan, M. A. Farooq, Z. H. Shamsi, and A. Mushtaq, “Mixed noise removal using adaptive median based non-local rank minimization,” *IEEE Access*, vol. 9, pp. 6438–6452, 2020.
- [61] B. Jähne, *Digital image processing*. Springer Science & Business Media, 2005.
- [62] D. Montenegro and J. Gonzalez, “Average filtering: Theory, design and implementation,” *Digital Signal Processing (DSP): Fundamentals, Techniques and Applications*, pp. 1–21, 2016.
- [63] P. Janani, J. Premalatha, and K. Ravichandran, “Image enhancement techniques: A study,” *Indian Journal of Science and Technology*, vol. 8, no. 22, pp. 1–12, 2015.
- [64] J. Chen, J. Benesty, Y. Huang, and S. Doclo, “New insights into the noise reduction wiener filter,” *IEEE Transactions on audio, speech, and language processing*, vol. 14, no. 4, pp. 1218–1234, 2006.
- [65] J. A. Noble and D. Boukerroui, “Ultrasound image segmentation: a survey,” *IEEE Transactions on medical imaging*, vol. 25, no. 8, pp. 987–1010, 2006.
- [66] K. Zhang, W. Zuo, and L. Zhang, “Ffdnet: Toward a fast and flexible solution for cnn-based image denoising,” *IEEE Transactions on Image Processing*, vol. 27, no. 9, pp. 4608–4622, 2018.

- [67] P. Kaur, G. Singh, and P. Kaur, “A review of denoising medical images using machine learning approaches,” *Current medical imaging*, vol. 14, no. 5, pp. 675–685, 2018.
- [68] S. Paris, P. Kornprobst, J. Tumblin, F. Durand *et al.*, “Bilateral filtering: Theory and applications,” *Foundations and Trends® in Computer Graphics and Vision*, vol. 4, no. 1, pp. 1–73, 2009.
- [69] K. N. Chaudhury and A. Singer, “Non-local euclidean medians,” *IEEE Signal Processing Letters*, vol. 19, no. 11, pp. 745–748, 2012.
- [70] C. Tian, L. Fei, W. Zheng, Y. Xu, W. Zuo, and C.-W. Lin, “Deep learning on image denoising: An overview,” *Neural Networks*, vol. 131, pp. 251–275, 2020.
- [71] D. Mahapatra, B. Bozorgtabar, J.-P. Thiran, and M. Reyes, “Efficient active learning for image classification and segmentation using a sample selection and conditional generative adversarial network,” in *International Conference on Medical Image Computing and Computer-Assisted Intervention*. Springer, 2018, pp. 580–588.
- [72] J. Benesty, S. Makino, J. Chen, J. Benesty, J. Chen, Y. Huang, and S. Doclo, “Study of the wiener filter for noise reduction,” *Speech enhancement*, pp. 9–41, 2005.
- [73] A. H. Sayed, *Adaptive filters*. John Wiley & Sons, 2011.
- [74] B. Shreyamsha Kumar, “Image denoising based on non-local means filter and its method noise thresholding,” *Signal, image and video processing*, vol. 7, pp. 1211–1227, 2013.
- [75] S. Bharati, T. Z. Khan, P. Podder, and N. Q. Hung, “A comparative analysis of image denoising problem: noise models, denoising filters and applications,” *Cognitive Internet of Medical Things for Smart Healthcare: Services and Applications*, pp. 49–66, 2021.
- [76] P. Sudeep, P. Palanisamy, J. Rajan, H. Baradaran, L. Saba, A. Gupta, and J. S. Suri, “Speckle reduction in medical ultrasound images using an unbiased non-local means method,” *Biomedical Signal Processing and Control*, vol. 28, pp. 1–8, 2016.
- [77] B. Goossens, H. Luong, A. Pizurica, and W. Philips, “An improved non-local denoising algorithm,” in *2008 International Workshop on Local and Non-Local Approximation in Image Processing (LNLA 2008)*, 2008, pp. 143–156.
- [78] J. Hou, H. Yu, C. P. Loizou, X. Huang, G. D. Liapi, and Y. Roussakis, “Automated prostate segmentation in ultrasound images based on different pre-processing schemes,” in *AIAI 2025: Artificial Intelligence Applications and Innovations*. Springer, 2024.
- [79] C. P. Loizou and C. S. Pattichis, *Despeckle filtering of ultrasound images*, ser. Atherosclerosis Disease Management. Springer, 2011.
- [80] C. P. Loizou, C. S. Pattichis, M. Pantziaris, and T. Tyllis, “Quality evaluation of ultrasound imaging in the carotid artery based on normalization and speckle reduction filtering,” *Medical and Biological Engineering and Computing*, vol. 44, pp. 414–426, 2006.
- [81] L.-C. Chen, Y. Zhu, G. Papandreou, F. Schroff, and H. Adam, “Encoder-decoder with atrous separable convolution for semantic image segmentation,” in *Proceedings of the European conference on computer vision (ECCV)*, 2018, pp. 801–818.

- [82] F. Yu and V. Koltun, “Multi-scale context aggregation by dilated convolutions,” *arXiv preprint arXiv:1511.07122*, 2015.
- [83] C. P. Loizou, C. S. Pattichis, C. I. Christodoulou, R. S. Istepanian, M. Pantziaris, and E. C. Kyriacou, “Comparative evaluation of despeckle filtering in ultrasound imaging of the carotid artery,” *IEEE transactions on ultrasonics, ferroelectrics, and frequency control*, vol. 52, no. 10, pp. 1653–1669, 2005.
- [84] V. Yeghiazaryan and I. Voiculescu, “Family of boundary overlap metrics for the evaluation of medical image segmentation,” *Journal of Medical Imaging*, vol. 5, no. 1, pp. 015 006–015 006, 2018.
- [85] L.-C. Chen, Y. Zhu, G. Papandreou, F. Schroff, and H. Adam, “Encoder-decoder with atrous separable convolution for semantic image segmentation,” in *Proceedings of the European conference on computer vision (ECCV)*, 2018, pp. 801–818.
- [86] H. J. Aerts, E. R. Velazquez, R. T. Leijenaar, C. Parmar, P. Grossmann, S. Carvalho, J. Bussink, R. Monshouwer, B. Haibe-Kains, D. Rietveld *et al.*, “Decoding tumour phenotype by noninvasive imaging using a quantitative radiomics approach,” *Nature communications*, vol. 5, no. 1, p. 4006, 2014.
- [87] F. Orlhac, S. Boughdad, C. Philippe, H. Stalla-Bourdillon, C. Nioche, L. Champion, M. Soussan, F. Frouin, V. Frouin, and I. Buvat, “A postreconstruction harmonization method for multicenter radiomic studies in pet,” *Journal of Nuclear Medicine*, vol. 59, no. 8, pp. 1321–1328, 2018.
- [88] S. Bhattacharjee, C.-H. Kim, H.-G. Park, D. Prakash, N. Madusanka, N.-H. Cho, and H.-K. Choi, “Multi-features classification of prostate carcinoma observed in histological sections: analysis of wavelet-based texture and colour features,” *Cancers*, vol. 11, no. 12, p. 1937, 2019.
- [89] R. J. Gillies, P. E. Kinahan, and H. Hricak, “Radiomics: images are more than pictures, they are data,” *Radiology*, vol. 278, no. 2, pp. 563–577, 2016.
- [90] A. Zwanenburg, M. Vallières, M. A. Abdalah, H. J. W. L. Aerts, V. Andrearzyk, A. Apte, S. Ashrafinia, S. Bakas, R. J. Beukinga, R. Boellaard, M. Bogowicz, L. Boldrini, I. Buvat, G. J. R. Cook, C. Davatzikos, A. Depeursinge, M.-C. Desserot, N. Dinapoli, C. V. Dinh, S. Echegaray, I. El Naqa, A. Y. Fedorov, R. Gatta, R. J. Gillies, V. Goh, M. Götz, M. Guckenberger, S. M. Ha, M. Hatt, F. Isensee, P. Lambin, S. Leger, R. T. Leijenaar, J. Lenkowicz, F. Lippert, A. Losnegård, K. H. Maier-Hein, O. Morin, H. Müller, S. Napel, C. Nioche, F. Orlhac, S. Pati, E. A. Pfaehler, A. Rahmim, A. U. Rao, J. Scherer, M. M. Siddique, N. M. Sijtsema, J. Socarras Fernandez, E. Spezi, R. J. Steenbakkers, S. Tanadini-Lang, D. Thorwarth, E. G. Troost, T. Upadhyaya, V. Valentini, L. V. van Dijk, J. van Griethuysen, F. H. van Velden, P. Whybra, C. Richter, and S. Löck, “The image biomarker standardization initiative: Standardized quantitative radiomics for high-throughput image-based phenotyping,” *Radiology*, vol. 295, no. 2, pp. 328–338, 2020, pMID: 32154773. [Online]. Available: <https://doi.org/10.1148/radiol.2020191145>
- [91] A. Hore and D. Ziou, “Image quality metrics: Psnr vs. ssim,” in *2010 20th international conference on pattern recognition*. IEEE, 2010, pp. 2366–2369.

- [92] Z. Wang, A. C. Bovik, H. R. Sheikh, and E. P. Simoncelli, “Image quality assessment: from error visibility to structural similarity,” *IEEE transactions on image processing*, vol. 13, no. 4, pp. 600–612, 2004.
- [93] K. M. Kempski, M. T. Graham, M. R. Gubbi, T. Palmer, and M. A. Lediju Bell, “Application of the generalized contrast-to-noise ratio to assess photoacoustic image quality,” *Biomedical Optics Express*, vol. 11, no. 7, pp. 3684–3698, 2020.
- [94] N. M. Razali, Y. B. Wah *et al.*, “Power comparisons of shapiro-wilk, kolmogorov-smirnov, lilliefors and anderson-darling tests,” *Journal of statistical modeling and analytics*, vol. 2, no. 1, pp. 21–33, 2011.
- [95] P. E. McKnight and J. Najab, “Mann-whitney u test,” *The Corsini encyclopedia of psychology*, pp. 1–1, 2010.
- [96] M. M. Mukaka, “A guide to appropriate use of correlation coefficient in medical research,” *Malawi medical journal*, vol. 24, no. 3, pp. 69–71, 2012.
- [97] D. Giavarina, “Understanding bland altman analysis,” *Biochimia medica*, vol. 25, no. 2, pp. 141–151, 2015.
- [98] W. S. Noble, “What is a support vector machine?” *Nature Biotechnology*, vol. 24, no. 12, pp. 1565–1567, 2006.
- [99] T. Joel and R. Sivakumar, “An extensive review on despeckling of medical ultrasound images using various transformation techniques,” *Applied Acoustics*, vol. 138, pp. 18–27, 2018.
- [100] Q. Yang, Q. Li, N. Li, Y. Luo, and J. Tang, “Prediction of prostate cancer based on ultrasound texture radiomics,” *Chinese Journal of Medical Ultrasound (Electronic Edition)*, vol. 21, no. 03, pp. 319–326, 2024, in Chinese.
- [101] U. Scheipers, H. Ermert, H.-J. Sommerfeld, M. Garcia-Schürmann, T. Senge, and S. Philippou, “Ultrasonic multifeature tissue characterization for prostate diagnostics,” *Ultrasound in medicine & biology*, vol. 29, no. 8, pp. 1137–1149, 2003.
- [102] A. Wibmer, H. Hricak, T. Gondo, K. Matsumoto, H. Veeraraghavan, D. Fehr, J. Zheng, D. Goldman, C. Moskowitz, S. W. Fine *et al.*, “Haralick texture analysis of prostate mri: utility for differentiating non-cancerous prostate from prostate cancer and differentiating prostate cancers with different gleason scores,” *European radiology*, vol. 25, pp. 2840–2850, 2015.
- [103] M. Shafiq-ul Hassan, G. G. Zhang, K. Latifi, G. Ullah, D. C. Hunt, Y. Balagurunathan, M. A. Abdallah, M. B. Schabath, D. G. Goldgof, D. Mackin *et al.*, “Intrinsic dependencies of ct radiomic features on voxel size and number of gray levels,” *Medical physics*, vol. 44, no. 3, pp. 1050–1062, 2017.
- [104] T. Chen, Z. Zhang, S. Tan, Y. Zhang, C. Wei, S. Wang, W. Zhao, X. Qian, Z. Zhou, J. Shen *et al.*, “Mri based radiomics compared with the pi-rads v2. 1 in the prediction of clinically significant prostate cancer: biparametric vs multiparametric mri,” *Frontiers in Oncology*, vol. 11, p. 792456, 2022.
- [105] K. Suzuki, “Overview of deep learning in medical imaging,” *Radiological physics and technology*, vol. 10, no. 3, pp. 257–273, 2017.

- [106] C. Xue, J. Yuan, G. G. Lo, A. T. Chang, D. M. Poon, O. L. Wong, Y. Zhou, and W. C. Chu, “Radiomics feature reliability assessed by intraclass correlation coefficient: a systematic review,” *Quantitative imaging in medicine and surgery*, vol. 11, no. 10, p. 4431, 2021.
- [107] M. Moradi, P. Mousavi, and P. Abolmaesumi, “Computer-aided diagnosis of prostate cancer with emphasis on ultrasound-based approaches: a review,” *Ultrasound in medicine & biology*, vol. 33, no. 7, pp. 1010–1028, 2007.
- [108] A. A. Taha and A. Hanbury, “Metrics for evaluating 3d medical image segmentation: analysis, selection, and tool,” *BMC medical imaging*, vol. 15, pp. 1–28, 2015.
- [109] K. Radlak and B. Smolka, “Adaptive non-local means filtering for speckle noise reduction,” in *International Conference on Computer Vision and Graphics*. Springer, 2014, pp. 518–525.
- [110] S. M. Pizer, E. P. Amburn, J. D. Austin, R. Cromartie, A. Geselowitz, T. Greer, B. ter Haar Romeny, J. B. Zimmerman, and K. Zuiderveld, “Adaptive histogram equalization and its variations,” *Computer vision, graphics, and image processing*, vol. 39, no. 3, pp. 355–368, 1987.
- [111] O. M. Mehr, M. Mohammadi, and M. Soryani, “Deep learning-based ultrasound image despeckling by noise model estimation.” *Iranian Journal of Electrical & Electronic Engineering*, vol. 19, no. 3, 2023.
- [112] M. Abdel-Nasser and O. A. Omer, “Ultrasound image enhancement using a deep learning architecture,” in *Proceedings of the International Conference on Advanced Intelligent Systems and Informatics 2016 2*. Springer, 2017, pp. 639–649.
- [113] E. Bertelli, L. Mercatelli, C. Marzi, E. Pachetti, M. Baccini, A. Barucci, S. Colantonio, L. Gherardini, L. Lattavo, M. A. Pascali *et al.*, “Machine and deep learning prediction of prostate cancer aggressiveness using multiparametric mri,” *Frontiers in oncology*, vol. 11, p. 802964, 2022.
- [114] R. T. Larue, J. E. van Timmeren, E. E. de Jong, G. Feliciani, R. T. Leijenaar, W. M. Schreurs, M. N. Sosef, F. H. Raat, F. H. van der Zande, M. Das *et al.*, “Influence of gray level discretization on radiomic feature stability for different ct scanners, tube currents and slice thicknesses: a comprehensive phantom study,” *Acta oncologica*, vol. 56, no. 11, pp. 1544–1553, 2017.
- [115] A. João, A. Gambaruto, R. Pereira, and A. Sequeira, “Robust and effective automatic parameter choice for medical image filtering.” *Computer Methods in Biomechanics and Biomedical Engineering: Imaging & Visualization*, vol. 8, no. 2, pp. 152–168, 2020.
- [116] P. Puech, O. Rouvière, R. Renard-Penna, A. Villers, P. Devos, M. Colombel, M.-O. Bitker, X. Leroy, F. Mège-Lechevallier, E. Comperat *et al.*, “Prostate cancer diagnosis: multiparametric mr-targeted biopsy with cognitive and transrectal us–mr fusion guidance versus systematic biopsy—prospective multicenter study,” *Radiology*, vol. 268, no. 2, pp. 461–469, 2013.
- [117] D. Sarkar, “The role of multi-parametric mri and fusion biopsy for the diagnosis of prostate cancer—a systematic review of current literature,” *Cell & Molecular Biology of Prostate Cancer: Updates, Insights and New Frontiers*, pp. 111–123, 2018.
- [118] Y. Ming, X. Dong, J. Zhao, Z. Chen, H. Wang, and N. Wu, “Deep learning-based multimodal image analysis for cervical cancer detection,” *Methods*, vol. 205, pp. 46–52, 2022.

- [119] A. Benelli, C. Vaccaro, S. Guzzo, C. Nedbal, V. Varca, and A. Gregori, “The role of mri/trus fusion biopsy in the diagnosis of clinically significant prostate cancer,” *Therapeutic Advances in Urology*, vol. 12, p. 1756287220916613, 2020.

## **APPENDICES**

# APPENDIX I

## List of Selected Stable Texture Features

Table I.1: Selected stable texture features

Source	Type	Feature
original	firstorder	Energy
original	firstorder	Kurtosis
original	firstorder	Mean
original	firstorder	Median
original	firstorder	RootMeanSquared
original	firstorder	Skewness
original	firstorder	TotalEnergy
original	glcm	ClusterShade
original	glcm	Correlation
original	glcm	Idmn
original	gldm	DependenceNonUniformity
original	gldm	LargeDependenceHighGrayLevelEmphasis
original	glrlm	GrayLevelNonUniformity
original	glszm	GrayLevelNonUniformity
original	ngtdm	Coarseness
wavelet-LLH	firstorder	90Percentile
wavelet-LLH	firstorder	Energy
wavelet-LLH	firstorder	Kurtosis
wavelet-LLH	firstorder	Maximum
wavelet-LLH	firstorder	Mean
wavelet-LLH	firstorder	Median
wavelet-LLH	firstorder	RootMeanSquared
wavelet-LLH	firstorder	Skewness
wavelet-LLH	firstorder	TotalEnergy
wavelet-LLH	glcm	ClusterShade
wavelet-LLH	glcm	Imc1
wavelet-LLH	gldm	DependenceNonUniformity
wavelet-LLH	gldm	GrayLevelNonUniformity
wavelet-LLH	gldm	SmallDependenceEmphasis
wavelet-LLH	gldm	SmallDependenceHighGrayLevelEmphasis
wavelet-LLH	gldm	SmallDependenceLowGrayLevelEmphasis
wavelet-LLH	glrlm	GrayLevelNonUniformity

*Continued on next page*

*Continued from previous page*

Source	Type	Feature
wavelet-LLH	glrlm	LongRunLowGrayLevelEmphasis
wavelet-LLH	glrlm	RunEntropy
wavelet-LLH	glrlm	RunLengthNonUniformity
wavelet-LLH	glrlm	RunLengthNonUniformityNormalized
wavelet-LLH	glrlm	RunVariance
wavelet-LLH	glrlm	ShortRunLowGrayLevelEmphasis
wavelet-LLH	glszm	GrayLevelNonUniformity
wavelet-LLH	glszm	GrayLevelNonUniformityNormalized
wavelet-LLH	glszm	GrayLevelVariance
wavelet-LLH	glszm	HighGrayLevelZoneEmphasis
wavelet-LLH	glszm	LargeAreaEmphasis
wavelet-LLH	glszm	LargeAreaHighGrayLevelEmphasis
wavelet-LLH	glszm	LargeAreaLowGrayLevelEmphasis
wavelet-LLH	glszm	LowGrayLevelZoneEmphasis
wavelet-LLH	glszm	SizeZoneNonUniformity
wavelet-LLH	glszm	SmallAreaHighGrayLevelEmphasis
wavelet-LLH	glszm	ZonePercentage
wavelet-LLH	glszm	ZoneVariance
wavelet-LHL	ngtdm	Coarseness
wavelet-LHL	ngtdm	Strength
wavelet-LHL	firstorder	Mean
wavelet-LHL	firstorder	Skewness
wavelet-LHL	glcm	Idmn
wavelet-LHL	glcm	MCC
wavelet-LHL	gldm	DependenceNonUniformity
wavelet-LHL	gldm	GrayLevelNonUniformity
wavelet-LHL	gldm	SmallDependenceLowGrayLevelEmphasis
wavelet-LHL	glrlm	GrayLevelNonUniformity
wavelet-LHL	glrlm	RunLengthNonUniformity
wavelet-LHL	glrlm	ShortRunLowGrayLevelEmphasis
wavelet-LHL	glszm	GrayLevelNonUniformity
wavelet-LHL	ngtdm	Coarseness
wavelet-LHH	firstorder	Mean
wavelet-LHH	firstorder	Skewness
wavelet-LHH	glcm	DifferenceEntropy
wavelet-LHH	glcm	DifferenceVariance
wavelet-LHH	glcm	Imc1
wavelet-LHH	gldm	DependenceNonUniformity

*Continued on next page*

*Continued from previous page*

Source	Type	Feature
wavelet-LHH	gldm	GrayLevelNonUniformity
wavelet-LHH	glrlm	GrayLevelNonUniformity
wavelet-LHH	glrlm	GrayLevelNonUniformityNormalized
wavelet-LHH	glrlm	GrayLevelVariance
wavelet-LHH	glrlm	RunLengthNonUniformity
wavelet-LHH	glszm	GrayLevelNonUniformity
wavelet-LHH	glszm	GrayLevelNonUniformityNormalized
wavelet-LHH	glszm	GrayLevelVariance
wavelet-LHH	glszm	HighGrayLevelZoneEmphasis
wavelet-LHH	glszm	LargeAreaEmphasis
wavelet-LHH	glszm	LargeAreaHighGrayLevelEmphasis
wavelet-LHH	glszm	LargeAreaLowGrayLevelEmphasis
wavelet-LHH	glszm	LowGrayLevelZoneEmphasis
wavelet-LHH	glszm	SizeZoneNonUniformity
wavelet-LHH	glszm	SizeZoneNonUniformityNormalized
wavelet-LHH	glszm	SmallAreaEmphasis
wavelet-LHH	glszm	SmallAreaHighGrayLevelEmphasis
wavelet-LHH	glszm	SmallAreaLowGrayLevelEmphasis
wavelet-LHH	glszm	ZoneEntropy
wavelet-LHH	glszm	ZonePercentage
wavelet-LHH	glszm	ZoneVariance
wavelet-LHH	ngtdm	Busyness
wavelet-LHH	ngtdm	Coarseness
wavelet-LHH	ngtdm	Strength
wavelet-HLL	firstorder	Mean
wavelet-HLL	glcm	MCC
wavelet-HLL	gldm	DependenceNonUniformity
wavelet-HLL	gldm	SmallDependenceLowGrayLevelEmphasis
wavelet-HLL	glrlm	GrayLevelNonUniformity
wavelet-HLL	ngtdm	Coarseness
wavelet-HLH	firstorder	Mean
wavelet-HLH	firstorder	Skewness
wavelet-HLH	glcm	DifferenceEntropy
wavelet-HLH	glcm	DifferenceVariance
wavelet-HLH	glcm	Imc1
wavelet-HLH	gldm	DependenceNonUniformity
wavelet-HLH	gldm	GrayLevelNonUniformity
wavelet-HLH	glrlm	GrayLevelNonUniformity

*Continued on next page*

*Continued from previous page*

Source	Type	Feature
wavelet-HLH	glrlm	RunLengthNonUniformity
wavelet-HLH	glszm	GrayLevelNonUniformity
wavelet-HLH	glszm	GrayLevelNonUniformityNormalized
wavelet-HLH	glszm	GrayLevelVariance
wavelet-HLH	glszm	HighGrayLevelZoneEmphasis
wavelet-HLH	glszm	LargeAreaEmphasis
wavelet-HLH	glszm	LargeAreaHighGrayLevelEmphasis
wavelet-HLH	glszm	LargeAreaLowGrayLevelEmphasis
wavelet-HLH	glszm	LowGrayLevelZoneEmphasis
wavelet-HLH	glszm	SizeZoneNonUniformity
wavelet-HLH	glszm	SizeZoneNonUniformityNormalized
wavelet-HLH	glszm	SmallAreaEmphasis
wavelet-HLH	glszm	SmallAreaHighGrayLevelEmphasis
wavelet-HLH	glszm	SmallAreaLowGrayLevelEmphasis
wavelet-HLH	glszm	ZoneEntropy
wavelet-HLH	glszm	ZonePercentage
wavelet-HLH	glszm	ZoneVariance
wavelet-HLH	ngtdm	Busyness
wavelet-HLH	ngtdm	Coarseness
wavelet-HLH	ngtdm	Strength
wavelet-HHL	firstorder	Mean
wavelet-HHL	firstorder	Median
wavelet-HHL	firstorder	Skewness
wavelet-HHL	glcm	ClusterShade
wavelet-HHL	glcm	Imc1
wavelet-HHL	glcm	MCC
wavelet-HHL	gldm	DependenceNonUniformity
wavelet-HHL	gldm	GrayLevelNonUniformity
wavelet-HHL	gldm	SmallDependenceLowGrayLevelEmphasis
wavelet-HHL	glrlm	GrayLevelNonUniformity
wavelet-HHL	glrlm	RunLengthNonUniformity
wavelet-HHL	ngtdm	Coarseness
wavelet-HHH	firstorder	Entropy
wavelet-HHH	firstorder	Median
wavelet-HHH	firstorder	Skewness
wavelet-HHH	firstorder	Uniformity
wavelet-HHH	glcm	Autocorrelation
wavelet-HHH	glcm	ClusterShade

*Continued on next page*

*Continued from previous page*

Source	Type	Feature
wavelet-HHH	glcm	JointAverage
wavelet-HHH	glcm	SumAverage
wavelet-HHH	glcm	SumSquares
wavelet-HHH	gldm	DependenceNonUniformity
wavelet-HHH	gldm	DependenceNonUniformityNormalized
wavelet-HHH	gldm	GrayLevelNonUniformity
wavelet-HHH	gldm	GrayLevelVariance
wavelet-HHH	gldm	HighGrayLevelEmphasis
wavelet-HHH	gldm	LargeDependenceHighGrayLevelEmphasis
wavelet-HHH	gldm	LargeDependenceLowGrayLevelEmphasis
wavelet-HHH	gldm	LowGrayLevelEmphasis
wavelet-HHH	gldm	SmallDependenceEmphasis
wavelet-HHH	gldm	SmallDependenceHighGrayLevelEmphasis
wavelet-HHH	gldm	SmallDependenceLowGrayLevelEmphasis
wavelet-HHH	glrlm	GrayLevelNonUniformity
wavelet-HHH	glrlm	GrayLevelNonUniformityNormalized
wavelet-HHH	glrlm	GrayLevelVariance
wavelet-HHH	glrlm	HighGrayLevelRunEmphasis
wavelet-HHH	glrlm	LongRunEmphasis
wavelet-HHH	glrlm	LongRunHighGrayLevelEmphasis
wavelet-HHH	glrlm	LongRunLowGrayLevelEmphasis
wavelet-HHH	glrlm	LowGrayLevelRunEmphasis
wavelet-HHH	glrlm	RunEntropy
wavelet-HHH	glrlm	RunLengthNonUniformity
wavelet-HHH	glrlm	RunLengthNonUniformityNormalized
wavelet-HHH	glrlm	RunPercentage
wavelet-HHH	glrlm	RunVariance
wavelet-HHH	glrlm	ShortRunEmphasis
wavelet-HHH	glrlm	ShortRunHighGrayLevelEmphasis
wavelet-HHH	glrlm	ShortRunLowGrayLevelEmphasis
wavelet-HHH	glszm	GrayLevelNonUniformity
wavelet-HHH	glszm	GrayLevelNonUniformityNormalized
wavelet-HHH	glszm	GrayLevelVariance
wavelet-HHH	glszm	HighGrayLevelZoneEmphasis
wavelet-HHH	glszm	LargeAreaEmphasis
wavelet-HHH	glszm	LargeAreaHighGrayLevelEmphasis
wavelet-HHH	glszm	LargeAreaLowGrayLevelEmphasis
wavelet-HHH	glszm	LowGrayLevelZoneEmphasis

*Continued on next page*

*Continued from previous page*

Source	Type	Feature
wavelet-HHH	glszm	SizeZoneNonUniformity
wavelet-HHH	glszm	SizeZoneNonUniformityNormalized
wavelet-HHH	glszm	SmallAreaEmphasis
wavelet-HHH	glszm	SmallAreaLowGrayLevelEmphasis
wavelet-HHH	glszm	ZoneEntropy
wavelet-HHH	glszm	ZonePercentage
wavelet-HHH	glszm	ZoneVariance
wavelet-HHH	ngtdm	Busyness
wavelet-HHH	ngtdm	Coarseness
wavelet-HHH	ngtdm	Strength
wavelet-LLL	firstorder	90Percentile
wavelet-LLL	firstorder	Energy
wavelet-LLL	firstorder	Kurtosis
wavelet-LLL	firstorder	Mean
wavelet-LLL	firstorder	Median
wavelet-LLL	firstorder	RootMeanSquared
wavelet-LLL	firstorder	Skewness
wavelet-LLL	firstorder	TotalEnergy
wavelet-LLL	glcm	ClusterShade
wavelet-LLL	glcm	Correlation
wavelet-LLL	glcm	Idmn
wavelet-LLL	glcm	Idn
wavelet-LLL	glcm	Imc1
wavelet-LLL	glcm	MCC
wavelet-LLL	gldm	DependenceNonUniformity
wavelet-LLL	gldm	LargeDependenceHighGrayLevelEmphasis
wavelet-LLL	gldm	SmallDependenceLowGrayLevelEmphasis
wavelet-LLL	glrlm	GrayLevelNonUniformity
wavelet-LLL	glrlm	RunLengthNonUniformity
wavelet-LLL	glszm	GrayLevelNonUniformity
wavelet-LLL	glszm	LargeAreaHighGrayLevelEmphasis
wavelet-LLL	glszm	ZoneEntropy
wavelet-LLL	ngtdm	Coarseness
square	firstorder	10Percentile
square	firstorder	Kurtosis
square	firstorder	Median
square	firstorder	Minimum
square	firstorder	Skewness

*Continued on next page*

*Continued from previous page*

Source	Type	Feature
square	firstorder	Uniformity
square	glcm	Correlation
square	glcm	Idmn
square	glcm	Idn
square	glcm	Imc1
square	glcm	InverseVariance
square	glcm	JointEnergy
square	glcm	MCC
square	glcm	MaximumProbability
square	gldm	DependenceEntropy
square	gldm	DependenceNonUniformity
square	gldm	DependenceNonUniformityNormalized
square	gldm	GrayLevelNonUniformity
square	gldm	LargeDependenceEmphasis
square	gldm	LargeDependenceLowGrayLevelEmphasis
square	gldm	LowGrayLevelEmphasis
square	gldm	SmallDependenceLowGrayLevelEmphasis
square	glrlm	GrayLevelNonUniformity
square	glrlm	LongRunEmphasis
square	glrlm	LongRunHighGrayLevelEmphasis
square	glrlm	LongRunLowGrayLevelEmphasis
square	glrlm	RunEntropy
square	glrlm	RunVariance
square	glszm	GrayLevelNonUniformity
square	glszm	SizeZoneNonUniformityNormalized
square	glszm	SmallAreaEmphasis
square	ngtdm	Coarseness
squareroot	firstorder	90Percentile
squareroot	firstorder	Energy
squareroot	firstorder	Maximum
squareroot	firstorder	RootMeanSquared
squareroot	firstorder	Skewness
squareroot	firstorder	TotalEnergy
squareroot	glcm	ClusterShade
squareroot	gldm	DependenceNonUniformity
squareroot	gldm	GrayLevelNonUniformity
squareroot	gldm	LargeDependenceHighGrayLevelEmphasis
squareroot	glrlm	GrayLevelNonUniformity

*Continued on next page*

*Continued from previous page*

Source	Type	Feature
squareroot	glrlm	LongRunHighGrayLevelEmphasis
squareroot	glrlm	LowGrayLevelRunEmphasis
squareroot	glrlm	RunLengthNonUniformity
squareroot	glrlm	ShortRunLowGrayLevelEmphasis
squareroot	glszm	GrayLevelNonUniformity
squareroot	glszm	ZoneEntropy
squareroot	ngtdm	Busyness
squareroot	ngtdm	Coarseness
squareroot	ngtdm	Strength
logarithm	firstorder	Energy
logarithm	firstorder	Entropy
logarithm	firstorder	InterquartileRange
logarithm	firstorder	Range
logarithm	firstorder	TotalEnergy
logarithm	firstorder	Uniformity
logarithm	glcm	ClusterProminence
logarithm	glcm	ClusterShade
logarithm	glcm	JointEnergy
logarithm	glcm	JointEntropy
logarithm	glcm	MaximumProbability
logarithm	glcm	SumEntropy
logarithm	gldm	DependenceNonUniformity
logarithm	gldm	GrayLevelNonUniformity
logarithm	glrlm	GrayLevelNonUniformity
logarithm	glrlm	GrayLevelNonUniformityNormalized
logarithm	glrlm	RunLengthNonUniformity
logarithm	glrlm	ShortRunLowGrayLevelEmphasis
logarithm	glszm	GrayLevelNonUniformity
logarithm	glszm	GrayLevelNonUniformityNormalized
logarithm	glszm	HighGrayLevelZoneEmphasis
logarithm	glszm	LargeAreaEmphasis
logarithm	glszm	LargeAreaHighGrayLevelEmphasis
logarithm	glszm	LowGrayLevelZoneEmphasis
logarithm	glszm	SmallAreaHighGrayLevelEmphasis
logarithm	glszm	ZoneEntropy
logarithm	glszm	ZoneVariance
logarithm	ngtdm	Strength
exponential	firstorder	Kurtosis

*Continued on next page*

*Continued from previous page*

Source	Type	Feature
exponential	firstorder	Median
exponential	glcm	Imc1
exponential	gldm	DependenceNonUniformity
exponential	gldm	GrayLevelNonUniformity
exponential	glrlm	GrayLevelNonUniformity
exponential	glrlm	RunVariance
exponential	glszm	SizeZoneNonUniformityNormalized
exponential	glszm	SmallAreaLowGrayLevelEmphasis
gradient	firstorder	Kurtosis
gradient	firstorder	Minimum
gradient	firstorder	Skewness
gradient	glcm	Idmn
gradient	gldm	DependenceNonUniformity
gradient	gldm	DependenceNonUniformityNormalized
gradient	glrlm	GrayLevelNonUniformity
gradient	glszm	GrayLevelNonUniformity
gradient	glszm	LowGrayLevelZoneEmphasis
gradient	glszm	SizeZoneNonUniformityNormalized
gradient	glszm	SmallAreaLowGrayLevelEmphasis
gradient	ngtdm	Coarseness